

USING EXTREME ULTRA-VIOLET AND SOFT X-RAY OBSERVATIONS AS
PROBES OF MAGNETIC RECONNECTION DURING SOLAR FLARES

by

Sabrina Leah Savage

A dissertation submitted in partial fulfillment
of the requirements for the degree

of

Doctor of Philosophy

in

Physics

MONTANA STATE UNIVERSITY
Bozeman, Montana

November 2010

©COPYRIGHT

by

Sabrina Leah Savage

2010

All Rights Reserved

APPROVAL

of a dissertation submitted by

Sabrina Leah Savage

This dissertation has been read by each member of the dissertation committee and has been found to be satisfactory regarding content, English usage, format, citations, bibliographic style, and consistency, and is ready for submission to the Division of Graduate Education.

Dr. David E. McKenzie

Approved for the Department of Physics

Dr. Richard J. Smith

Approved for the Division of Graduate Education

Dr. Carl A. Fox

STATEMENT OF PERMISSION TO USE

In presenting this dissertation in partial fulfillment of the requirements for a doctoral degree at Montana State University, I agree that the Library shall make it available to borrowers under rules of the Library. I further agree that copying of this dissertation is allowable only for scholarly purposes, consistent with “fair use” as prescribed in the U. S. Copyright Law. Requests for extensive copying or reproduction of this dissertation should be referred to Bell & Howell Information and Learning, 300 North Zeeb Road, Ann Arbor, Michigan 48106, to whom I have granted “the non-exclusive right to reproduce and distribute my dissertation in and from microform along with the non-exclusive right to reproduce and distribute my abstract in any format in whole or in part.”

Sabrina Leah Savage

November, 2010

DEDICATION

To my beautiful belles, Sierra and Alydah. You are brighter than any Sun in my sky. *You* are my reason.

To my little princess and monster, Quinn and Milo. You are the warm Sun on my face on a too cold day.

To my Ty. You are the continuum to my spectrum.

To Mom and Dad. For giving me a telescope 20 years ago.

ACKNOWLEDGEMENTS

This work would not have been possible without the vast support and patience of my advisor, Dr. David E. McKenzie. It was his previous work that inspired my own and his encouragement of independent research that ultimately allowed this dissertation to become more diverse than originally intended. The breadth of this research has greatly benefitted from the opportunities he provided to travel in order to meet colleagues around the world. I would especially like to thank Dr. McKenzie and the Harvard-Smithsonian Center for Astrophysics, notably Dr. Kathy Reeves, for the opportunity to be a part of the XRT community. The skills that I have acquired performing satellite operations and the experiences that I have been afforded in professional and international relations have proved invaluable to the complexity of this dissertation. In particular, XRT satellite operations have made me acutely aware of the tediousness and unexpected difficulties inherent in the scientific process, and although I may not have always expressed it properly, I am grateful for these lessons. By extension, I would like to acknowledge all of the satellite Chief Observers. For without their hard work and long days/nights, I would not have had access to the vast amounts of data required for the success of my research. I would also like to acknowledge the particularly supportive and enriching environment fostered by the Montana State University Physics Department. To everyone who has guided my long graduate career, please accept my sincerest gratitude.

TABLE OF CONTENTS

1. INTRODUCTION	1
1.1. Outline & Summary of Results	8
1.1.1. Chapter 2	8
1.1.2. Chapter 3	9
1.1.3. Chapter 4	11
1.1.4. Application to Models.....	12
1.1.5. Future Applications	14
2. QUANTITATIVE EXAMINATION OF SUPRA-ARCADE DOWN- FLOWS IN ERUPTIVE SOLAR FLARES	15
2.1. Introduction	15
2.2. Automated Detection Algorithm	19
2.3. Analysis of Solar Flare Data	23
2.3.1. 2002 April 21, TRACE data	27
2.3.2. 1999 January 20, SXT data	28
2.3.3. 2000 July 12, SXT data	29
2.4. Discussion: Relation to Reconnection	32
2.4.1. Measured Speeds	32
2.4.2. Observed Sizes	34
2.4.3. Estimation of Reconnecting Flux.....	34
2.4.4. Inferred Reconnection Rate	39
2.4.5. Shrinkage Energy	41
2.5. Conclusion	43
2.6. Acknowledgments	46
3. RECONNECTION OUTFLOWS AND CURRENT SHEET OB- SERVED WITH HINODE/XRT IN THE 2008 APRIL 9 “CARTWHEEL CME” FLARE	47
3.1. Introduction	47
3.2. Observations	49
3.3. Analysis	51
3.3.1. Candidate Current Sheet.....	52
3.3.2. Shrinking Loops & Flows	61
3.3.3. XRT & LASCO Upflows	72
3.4. Discussion.....	75
3.5. Summary & Conclusions.....	81
3.6. Acknowledgements	87

TABLE OF CONTENTS – CONTINUED

4. QUANTITATIVE EXAMINATION OF A LARGE SAMPLE OF SUPRA-ARCADE DOWNFLOWS IN ERUPTIVE SOLAR FLARES .	88
4.1. Introduction	88
4.1.1. Observations	91
4.1.2. Sources of Uncertainty	98
4.2. Analysis	101
4.2.1. Synthesis of Frequency Diagrams.....	103
Velocity & Acceleration	104
Area	104
Height	104
Magnetic Measurements.....	105
4.2.2. Trends	110
4.2.3. Magnetic Derivations	115
4.2.4. Drag Analysis	119
4.2.5. Loop Cooling.....	123
4.2.6. Discussion & Conclusions	124
REFERENCES CITED	130
APPENDICES	135
APPENDIX A: Flow Tables & Histograms	136
APPENDIX B: Ode to Dr. Seuss.....	171

LIST OF TABLES

Table	Page
1. Summary information of flares analyzed in this chapter.	24
2. List of flares exhibiting downflow signatures.	95
3. List of analyzed flares	97
4. Average de-projected velocities statistics.	137
5. Initial de-projected velocity statistics.	141
6. De-projected acceleration statistics. Positive accelerations indicate deceleration of the downflows.	145
7. Initial area statistics. “Manual area only” measurements are not plotted as histograms since there is no spread in the data. *No range in data.	149
8. Initial de-projected height statistics.	153
9. De-projected change in height statistics.	157
10. Initial magnetic flux statistics. “Manual area only” measurements are not plotted as histograms since there is no spread in the data. .	161
11. Shrinkage energy statistics. “Manual area only” measurements are not plotted as histograms since there is no spread in the data.	166

LIST OF FIGURES

Figure	Page
1. <i>Top</i> : Schematic depiction of the standard flux rope flare model. <i>Bottom</i> : Cartoon sequence depiction of the reconnection process at the diffusion site resulting in downflows and upflows.	3
2. SADs were first noticed during SXT observations of this limb flare which occurred on 1999 January 20. These images were taken from the discovery paper by McKenzie & Hudson (1999 [30]). The white arrows indicate the initial positions of two dark flows. The black arrows indicate the positions of the flows at later times. .	4
3. (a) Example image from the 2002 April 21 TRACE flare showing supra-arcade downflows (SADs) enclosed within the white box. (b) Example image from the 2003 November 4 flare with supra-arcade downflowing loops (SADLs) indicated by the arrows. The left panel of each set is the original image. The right panel has been enhanced for motion via run-differencing and scaled for contrast. .	5
4. (a) Cartoon depiction of SADs resulting from 3-D patchy reconnection. Discrete flux tubes are created, which then individually shrink, dipolarizing to form the post-eruption arcade. (b) Cartoon depiction of SADLs also resulting from 3-D patchy reconnection. Note that the viewing angle, indicated by the eye position, is perpendicular to that of SADs observations.	6
5. Testing the semi-automated software with an SXT-mimic synthetic data set. (a) Five artificial voids are seen in this frame. A total of sixteen voids were created in this 50-frame movie. The actual trajectories of all 16 are shown in panel (b), and the trajectories as determined by the software are in panel (c).	22

LIST OF FIGURES – CONTINUED

Figure	Page
6. Example trajectories from two SADs detected in the 21-Apr flare, demonstrating the range of uncertainty in the trajectory determinations. Panel (a) is a SAD with one of the noisier trajectories while (b) has very little scatter in the automatically determined trajectory. Velocities and accelerations can be derived from polynomial fits to the trajectories (as shown in the legends); however, for this chapter, only path-averaged speeds are reported. The error bars are derived by assigning an uncertainty to the positions as the square root of the diameter of the trough (or square root of the largest extent in the case of a non-circular trough).	26
7. (a) The famous flare of 2002 April 21 revealed downflows in TRACE and SUMER for the first time, and represents one of the sharpest observations of downflows. (b) Downflows detected in the 21-Apr flare, tracked by the automated routine and supplemented with manually-tracked flows.	27
8. (a) Image taken from the 20-Jan flare. (b) Enhanced image overlaid with downflow detections, tracked by the automated routine. The solar limb is at right; the arcade itself is obscured by pixel saturation. The center of the FOV moves by several arcseconds throughout the course of the observations. This shifting accounts for the northern track beyond the FOV for the selected overlay image.	28
9. (a) Image taken from 12-Jul flare. (b) Enhanced image overlaid with downflow detections, tracked by the automated routine. The solar limb is at left.	29
10. Distribution of average de-projected speeds found in the detected downflows- (a) 21-Apr flare, (b) 20-Jan flare, (c) 12-Jul flare. (The “Good” labels in the legends of (a) and (b) indicate that some detected flows were manually rejected from the final output set.)	30
11. Distribution of average areas found for the detected downflows: (a) 21-Apr flare, (b) 20-Jan flare, (c) 12-Jul flare. Only those flows detected with the automatic threshold routine were included in (a).	31

LIST OF FIGURES – CONTINUED

Figure	Page
12. Distribution of magnetic fluxes found for the detected downflows: (a) 21-Apr flare, (b) 20-Jan flare, and (c) 12-Jul flare.	36
13. Energies calculated for loop shrinkage: (a) 21-Apr flare, (b) 20-Jan flare, and (c) 12-Jul flare.	43
14. Cartoon depiction of supra-arcade downflows resulting from patchy reconnection. Discrete flux tubes are created, which then individually shrink, dipolarizing to form the post-eruption arcade. The measured quantities shown are averages from the current data set..	45
15. A CME is observed by XRT between 09:16 and 10:11 UT.	49
16. <i>Left:</i> Path of the erupted filament as seen by <i>STEREO A/SECCHI</i> . The dashed line indicates the radial direction extending from the active region as seen on the limb. The curved path follows the trajectory of the erupted structure from 08:53 UT (time of the reverse-scaled background image). <i>Right:</i> LASCO C2 frames (11:06 UT, 11:26 UT, 11:50 UT, 12:26 UT) showing the CME path beyond $\sim 2.5 R_{\odot}$. The dashed line indicates the radial direction extending from the active region projected onto the plane of the sky. The XRT FOV is shown in the upper left-hand corner of each image.	51
17. <i>Left:</i> (11:08:24 UT) <i>Right:</i> (17:31:55 UT) These reverse-scale images highlight the bright, thin linear feature (i.e. the candidate current sheet) extending from the apex of the arcade region from the 2008 April 9 event. Note the southward drift of approximately 4 deg/hr. All flows track along this feature even as it progresses southward.	53

LIST OF FIGURES – CONTINUED

Figure	Page
18. Reverse-scale composite images with an XRT inset overlaid onto corresponding LASCO C2 images. The candidate current sheet direction is represented by the solid line extending from the XRT arcade. The length of the line is extended to near the base of the CME in the LASCO images. The dotted line represents the initial direction of the CME as measured from the initial detection in the LASCO images (top left panel). The CME path direction as manually identified in each subsequent LASCO image is indicated by the dashed line. Notice that the CME does not follow a straight plane-of-sky path. The times indicated are those of the LASCO images.	55
19. (a) (13:09 UT) Reverse-scale XRT image highlighting the fan-like appearance of the candidate current sheet near the midpoint of the XRT image sequence. This suggests that the CCS is not being viewed completely edge-on. (b) Reverse-scale TRACE image from July 23, 2002 at 00:40 UT. The orientation of this flare is nearly mirrored to that of the “Cartwheel CME” flare but with a less-severe projection. A fan above the post-eruption arcade loops similar to that seen in (a) is easily discernible.....	57
20. <i>Left:</i> Example slice (white line) across the CCS for determining its thickness. <i>Right:</i> The intensity profile across the slit. The vertical dashed lines correspond to the positions chosen as the edges of the CCS. Note that the scales of the image and the profile have been reversed.	58
21. Reverse-scaled images selected for determining the CCS thickness. The slices across the CCS indicate the thickness determined for that position.	58
22. Reverse-scale composite images with an enlarged XRT inset overlaid onto corresponding LASCO C2 images. The length of the candidate current sheet is represented by the full solid line within the LASCO FOV. The “p” and “q” values correspond to the center of the white error boxes in the XRT and LASCO images, respectively. The times indicated are those of the LASCO images. The corresponding times for the inset XRT images differ by less than one minute.	62

LIST OF FIGURES – CONTINUED

Figure	Page
23. De-projected “q” and “p” heights in solar radii versus the time elapsed since the loss of equilibrium as seen in the <i>STEREO A</i> /SECCHI data (approximately 08:53 UT). (Refer to Figure 32 for a qualitative reference of the “q” and “p” positions.) This plot qualitatively agrees with predictions from the Lin & Forbes (2000 [22]) reconnection model wherein the distance between “q” and “p” increases steadily. (See Figure 9 from Webb et al. (2003 [60]) for a comparative graph.) The dashed horizontal line indicates the height of the null point ($0.25 R_{\odot} \sim 170$ Mm above the surface) which is discussed in Section 4.	63
24. Position versus time stackplot created with three-pixel wide slits taken along the current sheet candidate as it progressed southward within the XRT FOV. Representative slits are displayed as insets in the top-left hand corner. Each three-pixel segment represents approximately one minute. Dark and bright lanes indicate motion along the extractions. The black vertical strips are due to small data gaps, and the dashed vertical strip represents the large data gap beginning at 16:25 UT. The separate panels indicate that a different slit was used for that time frame to allow for the southward progression. The disassociation position of the reconnection outflow pair is indicated in the figure. The upflow portion of the disconnection event is much more diffuse than its downflow counterpart, making it appear broader and dimmer.....	64
25. (a) Plane-of-sky trajectories of the manually-tracked flows overlaid onto a reverse-scaled XRT image taken at 16:30:54 UT. (b) & (c) De-projected trajectories based on a convergent footpoint at a latitude of -18° and a longitude of 23° beyond the west limb. The reverse-scaled background images (MDI magnetogram plus magnetic loops) are derived from a PFSS model package (Schrijver & DeRosa 2003 [42]) with a center longitude set to (b) 115° and (c) 150° . The flows are assumed to have no velocity component in the longitudinal direction. The arrows represent upflow trajectories.....	66

LIST OF FIGURES – CONTINUED

Figure	Page
26. De-projected height-time profiles represented by (a) a typical downflow and (b) a typical upflow observed in this study. The vertical dotted lines mark the mid-exposure time of each image in the sequence. (Note that Flow 16 does not have a contiguously-detected track due to the low signal-to-noise ratio at the heights through which it travels.) The solid line is the 2-D polynomial fit applied to the profile to obtain the initial velocity and acceleration. The calculated fit parameters are given in the legend for each flow. The thick dashed line represents the gravitational profile for a body in free-fall given the initial height and velocity of the flow. The thin dashed profile line in (a) represents the gravitational profile for a body in free-fall experiencing a constant drag coefficient of $3.5 \times 10^{-3} \text{ s}^{-1}$	68
27. All de-projected height-time profiles. Profiles with a positive slope represent upflows. The eruption front and disconnection event profiles are labeled in the figure. Note that the initial heights of the upflow and downflow portions of the disconnection event are separated slightly because the region appears to brighten and move sunward prior to separating.	69
28. (a) Histogram of the initial de-projected velocities. Upflow velocities are positive. (b) Histogram of the de-projected accelerations. All flows are slowing down or have accelerations consistent with zero.	71
29. (a) Histogram of the initial de-projected heights. (b) Histogram of the de-projected change in heights.	71

LIST OF FIGURES – CONTINUED

Figure	Page
30. XRT & LASCO flow associations: All panels consist of composite XRT (reverse-scaled)/LASCO C2 images. <i>Top Panel</i> : The white crosses correspond to the extrapolated position of the XRT eruption front which tracks precisely with the white-light CME seen in the LASCO images. The acceleration of the LASCO CME is factored into the extrapolations; however, deflection is not included (see Figure 16). <i>Bottom Panel</i> : The LASCO images are running-mean-differenced and enhanced to emphasize flows. The colored crosses correspond to the extrapolated positions of the XRT upflows. Ellipses indicate strong XRT/LASCO flow associations after using the LASCO flow accelerations to extrapolate the XRT upflow positions. Note that the colors in this figure correspond to the colors of the tracks in Figure 25.	74
31. (a) PFSS model of the active region as it crossed the limb ($\sim 08:00$ UT on 2008 April 7) using a source surface at 2.5 solar radii (black dashed circle). <i>Blue</i> : Heliospheric current sheet and its separatrix (dashed). <i>Red</i> : Spine lines extending from the null point ($r = 1.25 R_{\odot}$) (where the spine line and dome (green) intersect). <i>Green</i> : Dome fan surface originating from the null point which encloses all of the closed field originating from the active region’s negative polarity. (b) Magnetogram taken a week before the flare. CE+ is the region of positive field that closes across the equator to negative flux in the northern hemisphere. CD+/- are the regions of positive/negative field enclosed by the dome described above. The “Open Field” region extends to the southeast of the active region.	75
32. Schematic diagram depicting a 3-D interpretation of the “Cartwheel CME” flare as seen by (a) XRT (rotated view) and (b) LASCO. A current sheet would form along the polarity inversion line (PIL) and between the leading edge of the erupted flux rope and arcade. The boundaries of this current sheet could extend along the length of the arcade.	78
33. Anchored legs of the flux rope slowly rotate southward (plane-of-sky) through the XRT FOV.	79

LIST OF FIGURES – CONTINUED

Figure	Page
34. Evolution of the current sheet near the arcade closely matching a rotated XRT FOV. The shrinking loops begin in the west and move southeastward along the polarity inversion line. The active current sheet indicates where reconnection is occurring and would likely appear as a bright, thin linear feature in XRT images.....	79
35. (a) Typical field in the neighborhood of the boundaries indicated by the colored lines in the right panel. (b) 2-D slices of the dome and spline lines (green and red, respectively) from the PFSS model shown in Figure 31 (a). The null point is indicated by a white triangle.....	80
36. Track composite images from Figure 25 with the null point overlaid....	81
37. (a) Schematic diagram of supra-arcade downflows (SADs) resulting from 3-D patchy reconnection. Discrete flux tubes are created, which then individually shrink, dipolarizing to form the post-eruption arcade. The measured quantities shown are averages from the following events: 1999 January 20 (M5.2); 2000 July 12 (M1.5); 2002 April 21 (X1.5) (McKenzie & Savage 2009 [31]). (b) Schematic diagram of supra-arcade downflowing loops (SADLs) also resulting from 3-D patchy reconnection. The measured quantities are averages from the flare occurring behind the western limb on 2008 April 9. Note that the viewing angle is perpendicular to that of the SADs observations.	83
38. (a) Example image from the 2002 April 21 TRACE flare showing supra-arcade downflows (SADs) enclosed within the white box. (b) Example image from the 2003 November 4 flare with supra-arcade downflowing loops (SADLs) indicated by the arrows. The left panel of each set is the original image. The right panel has been enhanced for motion via run-differencing and scaled for contrast.	88

LIST OF FIGURES – CONTINUED

Figure	Page
39. (a) Cartoon depiction of supra-arcade downflows (SADs) resulting from 3-D patchy reconnection. Discrete flux tubes are created, which then individually shrink, dipolarizing to form the post-eruption arcade. (b) Cartoon depiction of supra-arcade down-flowing loops (SADLs) also resulting from 3-D patchy reconnection. Note that the viewing angle, indicated by the eye position, is perpendicular to that of SADs observations.	89
40. Diagram depiction illustrating the possible reason for the lack of bright SADs despite observations of bright SADLs with a snapshot of a loop shrinking through a bright current sheet with a viewing angle <i>Top</i> : along the arcade axis and <i>Bottom</i> : perpendicular to the axis. (Different scales) The loop is bright on the left of both panels and dark on the right. Because the current sheet is thin and in a region of low signal, the bright loops are easier to observe along the arcade axis which is opposite for the dark loops.....	90
41. Radial magnetic fields derived from PFSS magnetic field modeling for the active regions producing flares observed by TRACE on a) 2002 July 23, b) 2002 April 21, and c) 2003 November 4. The initial height of the first flow per flare was used to create the figures. The footpoint region is circled. The west limb event in (a) predicts much weaker fields than the other two east limb events.	100
42. Synthesis of the de-projected trajectory information from Table 4. a) De-projected average velocity. b) De-projected initial velocity. c) De-projected acceleration. (Refer to the text for a detailed description of these figures.)	107
43. Synthesis of the area and height information from Table 4. a) Initial area. b) De-projected initial height. c) De-projected change in height. (Refer to the text for a detailed description of these figures.)	108
44. Synthesis of the magnetic information from Table 4. a) Initial magnetic field. b) Initial magnetic flux. c) Shrinkage energy. (Refer to the text for a detailed description of these figures.)	109

LIST OF FIGURES – CONTINUED

Figure	Page
45. Selected trend plots. (a) Initial area (only for those measured via the threshold technique) versus initial magnetic field strength. (b) Initial de-projected velocity versus initial magnetic field strength. (c) Initial de-projected velocity versus initial de-projected height. (d) Initial de-projected velocity versus elapsed time. (e) Initial de-projected height versus elapsed time. The elapsed time is the time from the initial flow observation per flare. Contained with the legends are the number of flows used to create the plot (#), the Spearman rank order correlation coefficient (S), the Spearman chance probability (%), and the Pearson linear correlation coefficient (P).....	111
46. Trends with respect to elapsed time related to the calculation of shrinkage energy. Specifically, $\Delta W \propto ((a)^2 \times (b) \times (c)) / (d)$ and $(e) = (a) \times (b)$. (a) Initial magnetic field strength. (b) Initial area for troughs measured using the threshold technique and those measured manually. (c) Change in de-projected height. (d) Flow travel time. (e) Initial magnetic flux. (f) Shrinkage energy. The elapsed time is the time from the initial flow observation per flare. Contained with the legends are the number of flows used to create the plot (#), the Spearman rank order correlation coefficient (S), the Spearman chance probability (%), and the Pearson linear correlation coefficient (P).....	118
47. Example flow profiles from the 2008 April 9 “Cartwheel CME” event observed by XRT. The thick line represents the 2-D polynomial fit to the trajectory. The thick dashed line represents the gravitational profile calculated using the initial height and initial speed of the flow. The thin dashed line represents the gravitational profile with some constant damping coefficient applied. The thin dashed vertical lines indicate the times of the available images.....	122
48. A plot of the applied drag constants, chosen to most closely match the flow profiles, versus initial height. The dashed line represents a linear fit to the data. Contained with the legend is the number of flows used to create the plot (#), the Spearman rank order correlation coefficient (S), the Spearman chance probability (%), and the Pearson linear correlation coefficient (P).....	122

LIST OF FIGURES – CONTINUED

Figure	Page
49. Images taken from the 2002 April 21 TRACE flare showing some of the post-eruption arcade loops cooling between the 195 Å temperature passbands.	124
50. (a) Schematic diagram of supra-arcade downflows (SADs) resulting from 3-D patchy reconnection. Discrete flux tubes are created, which then individually shrink, dipolarizing to form the post-eruption arcade. The measured quantities shown are averages from the limb events listed in Table 3 containing SADs. (b) Schematic diagram of supra-arcade downflowing loops (SADLs) also resulting from 3-D patchy reconnection. The measured quantities shown are averages from the limb events listed in Table 3 containing SADLs.	127
51. Histograms displaying average velocity frequency for the limb flares from this study as observed by a) SXT, b) XRT, c) TRACE, d) LASCO, e) SXT & XRT, f) SXT, XRT, & TRACE, and g) SXT, XRT, TRACE, & LASCO.	138
52. Histograms displaying average velocity frequency for the limb flares from this study which contained SADs as observed by a) SXT, b) XRT, c) TRACE, d) SXT & XRT, and e) SXT, XRT, & TRACE.	139
53. Histograms displaying average velocity frequency for the limb flares from this study which contained SADLs as observed by a) SXT, b) XRT, c) TRACE, d) LASCO, e) SXT & XRT, f) SXT, XRT, & TRACE, and g) SXT, XRT, TRACE, & LASCO.	140
54. Histograms displaying initial velocity frequency for the limb flares from this study as observed by a) SXT, b) XRT, c) TRACE, d) LASCO, e) SXT & XRT, f) SXT, XRT, & TRACE, and g) SXT, XRT, TRACE, & LASCO.	142
55. Histograms displaying initial velocity frequency for the limb flares from this study which contained SADs as observed by a) SXT, b) XRT, c) TRACE, d) SXT & XRT, and e) SXT, XRT, & TRACE.	143

LIST OF FIGURES – CONTINUED

Figure	Page
56. Histograms displaying initial velocity frequency for the limb flares from this study which contained SADLs as observed by a) SXT, b) XRT, c) TRACE, d) LASCO, e) SXT & XRT, f) SXT, XRT, & TRACE, and g) SXT, XRT, TRACE, & LASCO.....	144
57. Histograms displaying acceleration frequency for the limb flares from this study as observed by a) SXT, b) XRT, c) TRACE, d) LASCO, e) SXT & XRT, f) SXT, XRT, & TRACE, and g) SXT, XRT, TRACE, & LASCO.	146
58. Histograms displaying acceleration frequency for the limb flares from this study which contained SADs as observed by a) SXT, b) XRT, c) TRACE, d) SXT & XRT, and e) SXT, XRT, & TRACE.....	147
59. Histograms displaying acceleration frequency for the limb flares from this study which contained SADLs as observed by a) SXT, b) XRT, c) TRACE, d) LASCO, e) SXT & XRT, f) SXT, XRT, & TRACE, and g) SXT, XRT, TRACE, & LASCO.	148
60. Histograms displaying initial area frequency for the limb flares from this study as observed by a) SXT and b) TRACE. <i>Left:</i> Troughs chosen using thresholds. <i>Right:</i> Threshold plus manual trough areas.	150
61. Histograms displaying initial area frequency for the limb flares from this study as observed by c) SXT & XRT, d) SXT, XRT, & TRACE, and e) SXT, XRT, TRACE, & LASCO. <i>Left:</i> Troughs chosen using thresholds. <i>Right:</i> Threshold plus manual trough areas.	151
62. Histograms displaying initial area frequency for the limb flares from this study which contained SADs as observed by a) SXT, b) TRACE, c) SXT & XRT, and d) SXT, XRT, & TRACE. <i>Left:</i> Troughs chosen using thresholds. <i>Right:</i> Threshold plus manual trough areas.	152
63. Histograms displaying initial height frequency for the limb flares from this study as observed by a) SXT, b) XRT, c) TRACE, d) LASCO, e) SXT & XRT, f) SXT, XRT, & TRACE, and g) SXT, XRT, TRACE, & LASCO.	154

LIST OF FIGURES – CONTINUED

Figure	Page
64. Histograms displaying initial height frequency for the limb flares from this study which contained SADs as observed by a) SXT, b) XRT, c) TRACE, d) SXT & XRT, and e) SXT, XRT, & TRACE.	155
65. Histograms displaying initial height frequency for the limb flares from this study which contained SADLs as observed by a) SXT, b) XRT, c) TRACE, d) LASCO, e) SXT & XRT, f) SXT, XRT, & TRACE, and g) SXT, XRT, TRACE, & LASCO.	156
66. Histograms displaying change in height frequency for the limb flares from this study as observed by a) SXT, b) XRT, c) TRACE, d) LASCO, e) SXT & XRT, f) SXT, XRT, & TRACE, and g) SXT, XRT, TRACE, & LASCO.	158
67. Histograms displaying change in height frequency for the limb flares from this study which contained SADs as observed by a) SXT, b) XRT, c) TRACE, d) SXT & XRT, and e) SXT, XRT, & TRACE.	159
68. Histograms displaying change in height frequency for the limb flares from this study which contained SADLs as observed by a) SXT, b) XRT, c) TRACE, d) LASCO, e) SXT & XRT, f) SXT, XRT, & TRACE, and g) SXT, XRT, TRACE, & LASCO.	160
69. Histograms displaying magnetic flux frequency for the limb flares from this study as observed by a) SXT and b) TRACE. <i>Left:</i> Troughs chosen using thresholds. <i>Right:</i> Threshold plus manual trough areas.	162
70. Histograms displaying magnetic flux frequency for the limb flares from this study as observed by c) SXT & XRT, d) SXT, XRT, & TRACE, and e) SXT, XRT, TRACE, & LASCO. <i>Left:</i> Troughs chosen using thresholds. <i>Right:</i> Threshold plus manual trough areas.	163
71. Histograms displaying magnetic flux frequency for east limb flares from this study as observed by a) SXT, b) SXT & TRACE, and c) SXT, TRACE, & LASCO.	164
72. Histograms displaying magnetic flux frequency for the west limb flares from this study as observed by a) SXT, b) TRACE, c) SXT & XRT, and d) SXT, XRT, & TRACE.	165

LIST OF FIGURES – CONTINUED

Figure	Page
73. Histograms displaying magnetic work frequency for the limb flares from this study as observed by a) SXT and b) TRACE. <i>Left:</i> Troughs chosen using thresholds. <i>Right:</i> Threshold plus manual trough areas.	167
74. Histograms displaying magnetic work frequency for the limb flares from this study as observed by c) SXT & XRT, d) SXT, XRT, & TRACE, and e) SXT, XRT, TRACE, & LASCO. <i>Left:</i> Troughs chosen using thresholds. <i>Right:</i> Threshold plus manual trough areas.	168
75. Histograms displaying magnetic work frequency for the east limb flares from this study as observed by a) SXT, b) SXT & TRACE, and c) SXT, TRACE, & LASCO.	169
76. Histograms displaying magnetic work frequency for the limb flares from this study which contained SADs as observed by a) SXT, b) TRACE, c) SXT & XRT, and d) SXT, XRT, & TRACE.	170

ABSTRACT

Sunward-flowing voids above post-coronal mass ejection (CME) flare arcades were first discovered using the soft X-ray telescope (SXT) aboard *Yohkoh* and have since been observed with *TRACE* (extreme ultra-violet (EUV)), *SOHO/LASCO* (white light), *SOHO/SUMER* (EUV spectra), and *Hinode/XRT* (soft X-rays (SXR)). These supra-arcade downflows (SADs) have been shown to be plasma deficient with respect to their surroundings and follow trajectories which slow as they reach the top of the arcade. Characteristics such as these are consistent with post-reconnection magnetic flux tube cross-sections. The tubes retract from a reconnection site high in the corona until they reach a more potential magnetic configuration – a process in line with the standard model of reconnection. Viewed from a perpendicular angle, SADs should appear as shrinking loops rather than downflowing voids. In fact, observations of supra-arcade downflowing loops (SADLs) yield speeds and decelerations consistent with those determined for SADs. For this dissertation I have compiled a substantial SADs flare catalog and have developed semi-automatic detection software to detect and track individual downflows in order to provide statistically significant samples of parameters such as velocity, acceleration, area, magnetic flux, shrinkage energy, and reconnection rate. In addition, I provide measurements connecting supra-arcade upflows with flows observed by *LASCO* in the outer corona following a CME which further substantiates the standard reconnection model. I discuss these measurements, how they were obtained, and what impact they have on reconnection models.

INTRODUCTION

Solar flares are the most energetic events occurring in our solar system and directly affect the Earth through the interaction of magnetic fields and highly energetic particles; therefore, understanding flare origins and evolution has become a key scientific concern. Magnetic reconnection is widely accepted as a trigger for flare energy release and is theorized to occur quickly (on order of seconds to minutes) in the low-emission corona above a brightening active region. Under these constraints, directly observing flare reconnection is hindered by instrumental capacity (e.g. spatial resolution, field of view (FOV), dynamic range, temporal cadence). Therefore, empirical reconnection studies generally involve observing the environment preceding the change in field line topology and/or the consequences of rearranging the energetics of the field.

In standard reconnection models, magnetic loops flowing into the diffusion site and then away from it in opposite directions after undergoing reconnection are an inevitable theoretical consequence (Figure 1) (Carmichael 1964 [2]; Sturrock 1968 [50]; Hirayama 1974 [11]; Kopp & Pneuman 1976 [19]; Forbes & Acton 1996 [7]; Lin & Forbes 2000 [22]). Understanding the behavior and construct of these loops can provide us with the closest insight into the reconnection process without being able to observe the actual change in field line topology itself. Reconnection rates have been derived from observations of pre-reconnection, inflowing loops as well as from post-reconnection separation of brightened footpoints in the chromosphere (Yokoyama et al. 2001 [61]; Narukage & Shibata 2006 [32]; Saba et al. 2001 [39]; Fletcher & Hudson

2001 [5]). Prior to this current study however, observations of post-reconnection loops above the flaring site have only been speculated with limited exploration into their innate characteristics (McKenzie & Hudson 1999 [30]; McKenzie 2000 [29]; Innes et al. 2003a [14]; Asai et al. 2004 [1]; Sheeley, Warren, & Wang 2004 [46]; Khan et al. 2007 [17]; Reeves, Seaton, & Forbes 2008 [37]). Yet these loops contain more information about the reconnection process (e.g. diffusion time from cross-section sizes, magnetic flux involved per episode, energy released through relaxation, reconnection rates, etc.). Realistically, though, these newly-reconnected loops require very special circumstances in order to image since they can be relatively devoid of emitting plasma with respect to their surroundings (Innes et al. 2003a [14]) and travel through the corona where they are viewed against a dark background.

Figure 1 provides a schematic depiction of the standard flux rope flare model to which we will ascribe for this study (Shibata 1995 [48]). The flux rope is initially prohibited from erupting by an overlying magnetic field. This field de-stabilizes via some process – possibly through reconnection in the vicinity of the flux rope due to flux emergence, shearing of footpoints, MHD instabilities, etc. – which then allows the flux rope to escape. As the flux rope travels into the outer corona, field lines are swept together in its wake, a current sheet forms where there is a discontinuity in the field line polarities, and the field lines reconnect through this current sheet. Each reconnection episode results in a new set of loops with one moving away from the solar surface and the other moving toward it (shown in the lower panel). Those newly

reconnected loops moving *towards* the solar surface are referred to as **downflows** in this text. Those moving *away* are introduced as **upflows** in Chapter 3. Both downflows and upflows can also be referred to as reconnection **outflows**.

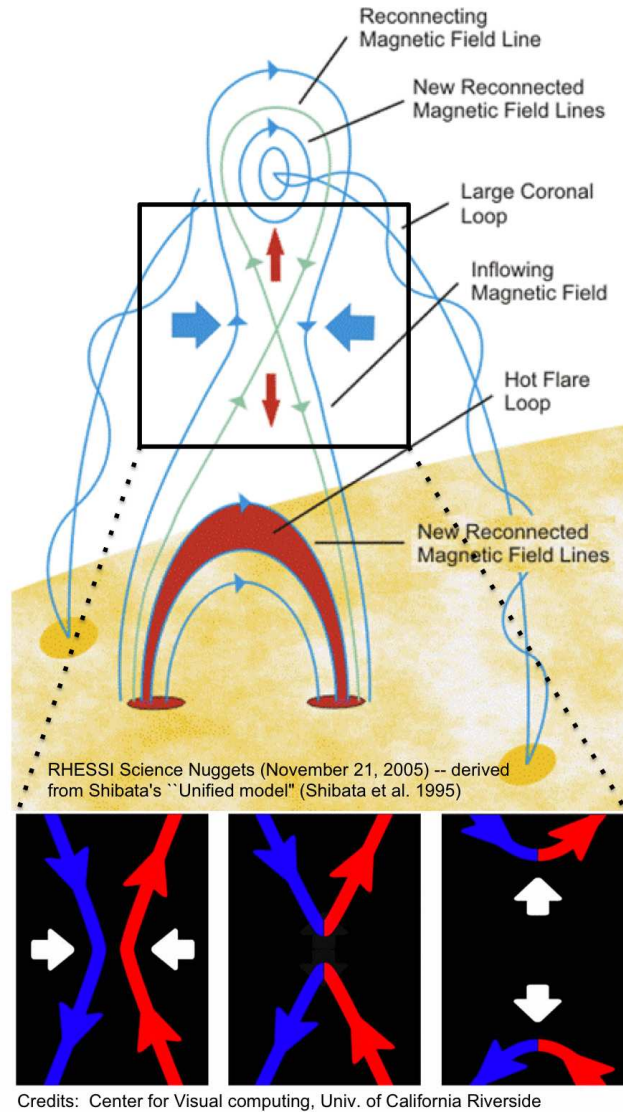


Figure 1: *Top:* Schematic depiction of the standard flux rope flare model. *Bottom:* Cartoon sequence depiction of the reconnection process at the diffusion site resulting in downflows and upflows.

After the initial energy release of a long duration flare, a series of flux tubes rooted in the photosphere along footpoint ribbons becomes apparent above the active region. An interesting discovery found to occur above these arcades are sunward-flowing dark, teardrop-shaped features. These supra-arcade downflows (SADs) were first observed above an east limb, M4.5 GOES class flare occurring on 1999 January 20 and observed by *Yohkoh*/SXT (Figure 2) (McKenzie & Hudson 1999 [30]; McKenzie 2000 [29]).

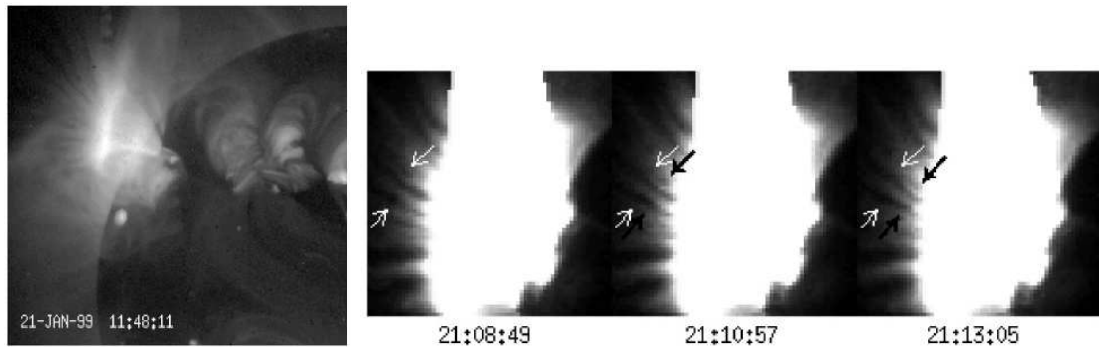


Figure 2: SADs were first noticed during SXT observations of this limb flare which occurred on 1999 January 20. These images were taken from the discovery paper by McKenzie & Hudson (1999 [30]). The white arrows indicate the initial positions of two dark flows. The black arrows indicate the positions of the flows at later times.

SADs have since been observed in several flares with various instruments (namely, *TRACE*, *SOHO*/LASCO, *SOHO*/SUMER, *Hinode*/XRT, and *STEREO*/SECCHI). Supra-arcade downflowing loops (SADLs) are also observed to shrink in the same region as SADs and with similar trajectories. Figure 3 provides an example of each type of observation. The downflowing voids (SADs) differ in appearance from downflowing loops (SADLs) possibly due to observational perspective. If the loops are

viewed nearly edge-on as they retract through a bright current sheet, then SADs may represent the cross-sections of the SADLs (see Figure 4). These newly-reconnected loops form high above the arcade in the hot, low-density plasma regime – a hypothesis supported by the lack of emission in both extreme ultra-violet (EUV) and soft X-rays (SXR). The loops subsequently retract from the reconnection site in a manner described by a three-dimensional generalization of the aforementioned standard reconnection model (McKenzie & Savage 2009 [31] – Chapter 2; Savage et al. 2010 [40] – Chapter 3). Confirming the connection between SADs, shrinking loops, magnetic reconnection, and flare energy release is a challenging issue considering the lack of coincidental observations using multiple wavelengths.

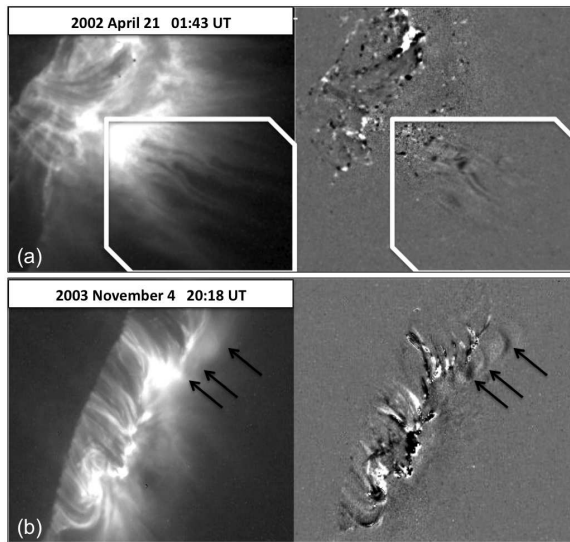


Figure 3: (a) Example image from the 2002 April 21 TRACE flare showing supra-arcade downflows (SADs) enclosed within the white box. (b) Example image from the 2003 November 4 flare with supra-arcade downflowing loops (SADLs) indicated by the arrows. The left panel of each set is the original image. The right panel has been enhanced for motion via run-differencing and scaled for contrast.

The loops are expected to travel from the reconnection site at speeds near the Alfvén speed and then decelerate as they approach the potential magnetic configuration of the arcade (Linton & Longcope 2006 [25]). While the flows have been measured to travel much slower than the Alfvén speed (possibly due to drag forces, see Section 4.2.4), they are, in fact, seen to decelerate towards the end of their track as they settle near the top of the arcade (McKenzie & Savage 2009 [31] – Chapter 2, Section 2.3; Savage et al. 2010 [40] – Chapter 3, Section 3.3.2). Retracting loop signatures in cusped flares have also been observed (Reeves, Seaton, & Forbes 2008 [37]) as well as individual SADs above a post-CME arcade (Savage et al. 2010 [40] – Chapter 3, Section 3.3.2). Figure 4 provides a cartoon diagram illustrating the viewing-angle difference between SADs and SADLs.

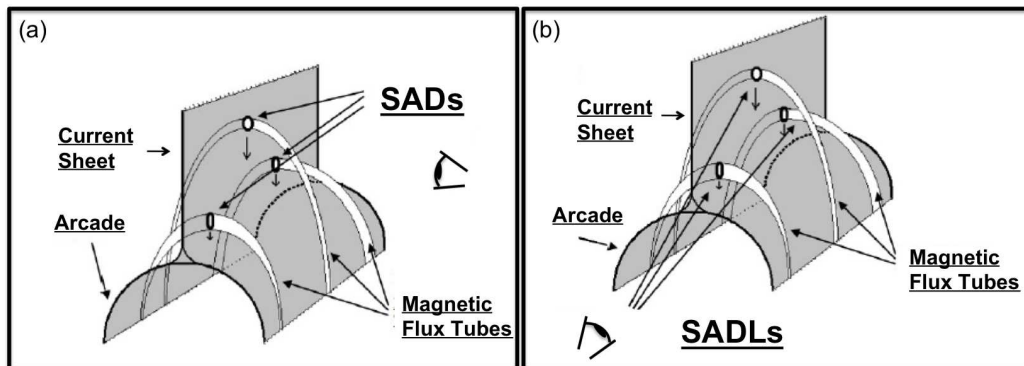


Figure 4: (a) Cartoon depiction of SADs resulting from 3-D patchy reconnection. Discrete flux tubes are created, which then individually shrink, dipolarizing to form the post-eruption arcade. (b) Cartoon depiction of SADLs also resulting from 3-D patchy reconnection. Note that the viewing angle, indicated by the eye position, is perpendicular to that of SADs observations.

The one instance of spectral analysis during downflow observations, which was obtained by *SOHO*/SUMER in the C II, Fe XII, and Fe XXI lines, indicates that the dark flows are plasma deficient as there was found to be no line emission associated with them nor was there continuum absorption (Innes et al. 2003a [14]). Bright flows are also observed which may be due to varying chromospheric evaporation timescales (i.e. the time it takes for them to fill with plasma from the chromosphere) or changing conditions within the current sheet (as speculated in Section 3.4 for the dark-to-bright transition of the flows observed in the “Cartwheel CME” flare). Most of the flows observed in this study are dark because they are typically easier to distinguish from the background. (Refer to Section 4.1 for more discussion of bright flows.)

The goal of this dissertation is to build up a catalog of SADs and SADLs observations in order to advance our understanding of their origin and to place quantitative constraints upon characteristics such as speed, acceleration, and size. This goal has been achieved through the development and use of semi-automatic detection and tracking software supplemented by a manual version for loops and noisier image sets. Section 2.2 discusses the semi-automated techniques. The manual version is implemented in Chapters 3 & 4. A detailed flare analysis of an event from 2008 April 9 is also used to observationally enhance our picture of reconnection occurring along a current sheet high above a flaring active region. The analyses presented in this study lend substantial support to the hypothesis that they are, in fact, loops shrinking from a reconnection site high in the corona above the flare instead of, for instance,

cool sunward-flowing plasmoids associated with a coronal mass ejection (CME). Then basing our assumptions upon this loop model, we derive estimates of the magnetic characteristics associated with a large sample of flows which can then be evaluated in the context of often-cited reconnection models – namely, Sweet-Parker and Petschek (Sweet 1958 [54]; Parker 1963 [33]; Petschek 1964 [34]).

1.1. Outline & Summary of Results

The following sections provide a brief overview of the enclosed chapters along with a summary of results. Chapters 2 & 3 are based on published papers – McKenzie & Savage (2009 [31]) and Savage et al. (2010 [40]), respectively.

1.1.1. Chapter 2

“Quantitative Examination of Supra-Arcade Downflows in Eruptive Solar Flares”

Chapter 2 discusses the methodology implemented to extract downflow observables relevant to reconnection (e.g. velocity, acceleration, height, size). Results from the application of the methods to three large flares (1999 January 20, 2000 July 12, & 2002 April 21) are provided. Magnetic flux and shrinkage energy estimates are derived by combining the measured sizes and heights with magnetic fields obtained via PFSS modeling. Typical flux estimates per loop are on order of a few $\times 10^{18}$ Mx which is consistent with empirical findings of “parcels of $\sim 4 \times 10^{18}$ Mx at a time” (Longcope et al. 2005 [28]). These magnetic flux and energy approximations are

subject to large observational and model-dependent uncertainties; however, we believe that these are the first empirical estimates derived from SADs observations of the characteristic flux participating in individual reconnection events. The shrinkage energy per event is found to be $\sim 10^{27}$ ergs. Summing over the number of flows yields approximately $10^{28} - 10^{29}$ ergs released through the relaxation of the *detected* loops. This amount does not approach the total flare energy budget but does reveal continual energy deposition following the impulsive phase of the flare. To our knowledge, this is also the first report of empirical estimates of the energy release from the relaxation of the newly-reconnected field. Then from the total energy estimates, we infer reconnection rates on order of 10^{16} Mx s⁻¹ which is comparable to previously reported values by Yokoyama et al. (2001 [61]) and Longcope et al. (2005 [28]) using other methods. Within large uncertainty, our reconnection rate may represent a lower bound considering that we can only include the flux and energy from detectable and trackable flows. Additional flows within the same time frame would increase the energy budget and, in turn, the reconnection rate.

1.1.2. Chapter 3

“Reconnection Outflows and Current Sheet Observed with Hinode/XRT in the 2008 April 9 ‘Cartwheel CME’ Flare”

In Chapter 3 we present a detailed discussion of an XRT flare occurring behind the limb on 2008 April 9 – including current sheet, SADs, and SADLs observations

along with magnetic field analysis of the active region. Observations of flows retracting through an observable current sheet high above the footpoints ($\sim 80\text{--}200$ Mm) make this flare particularly unique and intriguing. Thickness values for the current sheet are reported as at least 10 times narrower than several previous measurements from other flares (Ciaravella & Raymond 2008 [3]), Lin et al. (2007 [24]), Webb et al. (2003 [60]), Ciaravella et al. (2002 [4]), and Ko et al. (2003 [18]). This discrepancy may be explained by instrumental- and height-dependence of the thickness measurement (see Section 3.3.1). Our thickness estimate of $(4\text{--}5)\times 10^3$ km may indicate a turbulent current sheet (Ciaravella & Raymond 2008 [3]). We provide ample discussion concerning the apparent rotation of the current sheet through the FOV and attribute it to a projection effect combined with a highly-inclined polarity inversion line (Section 3.4).

Shrinking loops and upflows are clearly imaged for this flare from which trajectory information is obtained. Even more interesting, however, is the observation of a possible reconnection outflow pair episode occurring at nearly 190 Mm above the solar surface. To our knowledge, an outflow pair episode such as this (i.e. appearing in a region where retracting loops and upflows have been observed and along a directly observable SXR current sheet) has not been observed this close to the solar surface. The upflow positions are then extrapolated from the XRT FOV into the LASCO C2 FOV where a possible correspondence is found between the upflows and coronal density enhancements tracking with the erupted flux rope. Additionally, the upflow

portion of the reconnection outflow pair episode appears to correspond with the CME pinch-off point. Basically, this flare is a nice representative of the standard model presented in Figure 1 complete with an erupted flux rope, current sheet, post-eruption arcade, and reconnection outflows.

1.1.3. Chapter 4

“Quantitative Examination of a Large Sample of Supra-Arcade Downflows in Eruptive Solar Flares”

Finally, the results from 35 flares with 369 downflows are reported and discussed in Chapter 4. The average velocities of the flows (typically up to only a few $\times 100$ km s⁻¹) are found to be unexpectedly slower than expected Alfvén speeds (on order of 10^3 km s⁻¹). Some interpretations of these results are that either the Alfvén speed is lower than expected in the reconnection region, the drag may be overwhelming the magnetic tension force pulling down the loops causing them to retract slower, entanglement of field lines or plasma compressibility during the reconnection process reduces the initial speed, or even continual field entanglement during the retraction phase through the current sheet slows the flows. Plasma compressibility is shown in Section 2.4.1 to be negligible. There is also the possibility that the flows are not retracting reconnected loops; however, several of the flare observations clearly show shrinking loop features, and the slowing of the flows as they approach the arcade would become difficult to explain otherwise. The possibility of drag affecting the flows is further explored in Section 4.2.4.

The parameter estimations explored in Chapter 2 are confirmed using the large sample population (velocity $\sim 10^2$ km s $^{-1}$; acceleration ~ 0 km s $^{-2}$; height $\sim 10^5$ km; Δ height $\sim 10^4$ km; area $\sim 10^7$ km 2 ; magnetic flux $\sim 10^{18}$ Mx; shrinkage energy $\sim 10^{27}$ ergs; reconnection rate $\sim 10^{16}$ Mx s $^{-1}$). See Figure 50 for a graphical summary of results. Comparing the parameter estimations between SADs and SADLs lends substantial evidence supporting the link between them (Section 4.2.1). Trends in the data are explored in Section 4.2.2. The most notable trend is the positive correlation between height versus flare progression time (Figure 45 (e)). This link may provide a check on the standard model which predicts a continual rise in the reconnection site or may simply be explained through observational bias. For measurements that are not area-dependent, there is also good agreement between the EUV and SXR instruments which suggests that the flow observations are not temperature dependent. Flow sizes are shown to be highly sensitive to instrument resolution in Figure 43 (a). The exceptional temperature-dependent observation concerns the earliest flows seen in the 2002 April 21 TRACE flare, which appear to cool on order of 15–40 minutes (see Section 4.2.5). This observation is possible due to the use of the 195 Å TRACE filter which has two distinguishable temperature bandpasses.

Continual addition of flare data expected to be available with the rise of solar activity will serve to enhance the interpretations of these possible trends. Newly available high resolution imagers will also further aid in trend reliability.

1.1.4. Application to Models

It is hoped that 3D models of patchy reconnection will provide predicted distributions to which the observations in Chapter 4 can be compared – in particular, distributions of flux tube sizes and outflow speeds that mimic the empirically determined distributions. We propose that reproduction of the observed characteristics (e.g., fluxes of 10^{18} Mx per reconnection episode) is a reasonable objective. Currently, the lack of positive acceleration throughout the flow lifetimes and the fast reconnection rates support the Petschek model over Sweet-Parker (Sweet 1958 [54]; Parker 1963 [33]; Petschek 1964 [34]; Somov 1992 [49]). Note that the result from Yokoyama et al. (2001 [61]) also indicates reconnection of the faster Petschek kind, rather than Sweet-Parker. With our reconnection rates similar to Yokoyama’s, the implication is that patchy reconnection, while not steady-state (by definition of “patchy”), may resemble Petschek’s geometry more than Sweet-Parker.

Our thickness estimates of the current sheet observed during the “Cartwheel CME” event (Chapter 3) suggest that turbulence may be a physical source of the anomalous resistivity that seems to be required for reconnection to proceed on relevant time scales – although this is highly speculative. Full 3D (or at least 2.5D) simulations are more appropriate applications of the models in order to reproduce the discrete nature of the flows (both in space and time) and the variation in their sizes, speeds, and field strengths (Linton & Longcope 2006 [25]; Longcope, Guidoni, & Linton 2009 [27]).

1.1.5. Future Applications

Assuming that SADs are shrinking reconnected loops, then their presence should be associated with hard X-ray (HXR) signatures through various possible processes resulting in accelerated particles via reconnection (i.e. electric field generation, plasma waves, turbulence, shocks, Alfvén wave dissipation, etc.) Analyzing the flow timings with respect to hard X-ray (HXR) signatures using RHESSI is planned as future work. Such a project may provide coveted insight into the flare particle acceleration and energy input mechanisms.

QUANTITATIVE EXAMINATION OF SUPRA-ARCADE DOWNFLOWS IN ERUPTIVE SOLAR FLARES

2.1. Introduction

Supra-arcade downflows (SADs) are downward-moving features observed in the hot, low-density region above post-eruption flare arcades. Initially detected with the *Yohkoh* Soft X-ray Telescope (SXT) as X-ray-dark, blob-shaped features, downflows have since been observed with TRACE (e.g., Innes et al. 2003a [14]; Asai et al. 2004 [1]) *SOHO*/SUMER (Innes et al. 2003a [14]), *SOHO*/LASCO (Sheeley & Wang 2002 [44]), and Hinode/XRT.

The darkness of these features in X-ray and EUV images and spectra, together with the lack of absorption signatures in EUV, indicate that the downflows are best explained as pockets of very low plasma density, or *plasma voids* (see especially Innes et al. 2003a [14]). Because these plasma voids are able to resist being filled in immediately by the surrounding ambient plasma, it seems reasonable to presume that magnetic flux within the voids provides supporting pressure. A configuration consistent with the observations is a magnetic flux tube, filled with flux but with very little plasma, shrinking into the post-eruption arcade (McKenzie & Hudson 1999 [30]; McKenzie 2000 [29]).

It is thus believed that the downflows represent the outflow of magnetic flux from a reconnection site, in keeping with the standard reconnection model of eruptive flares. The emptiness and motion of the plasma voids is consistent with flux tubes

shrinking at rates exceeding the speed with which chromospheric evaporation can fill them with plasma (McKenzie & Hudson 1999 [30]).

This interpretation does not conflict with the results of Verwichte et al. (2005 [58]). Verwichte et al. (2005 [58]) analyzed the oscillations of the supra-arcade rays in the 2002 April 21 flare observed by TRACE, and found that the oscillations can be described as sunward-traveling wave packets. That paper focused only on the oscillations in the rays, or ‘tails of the tadpoles’, and did not speculate on the nature of the plasma voids, or ‘heads of the tadpoles’. We have confirmed this interpretation of the paper through private communication with Verwichte. The suggestion, occasionally raised in conversations with various colleagues, that Verwichte et al. (2005 [58]) offers an alternate interpretation of plasma voids arises from the imprecise nomenclature used in the paper, wherein ‘tadpole’ sometimes refers to the head alone, and more often to the dark tail. We avoid the term ‘tadpole’ because of this confusion, and also because the term conjures an image of a blob denser than its surroundings, contrary to the findings of Innes et al. (2003a [14]).

The speeds of SADs reported previously (e.g., McKenzie & Hudson 1999 [30]; McKenzie 2000 [29]; Innes et al. 2003a [14]; Asai et al. 2004 [1]) are on the order of a few $\times 10^1 - 10^2$ km s⁻¹, slower than canonically expected for reconnection outflows (i.e., slower than the 1000 km s⁻¹ which is often assumed to be the Alfvén speed). Linton & Longcope (2006 [25]) suggest the possibility of drag forces working against the reconnection outflow to explain why the speeds are sub-Alfvénic. In their model,

reconnection was allowed to occur for a finite period of time, in a localized region of slightly enhanced resistivity, and reconnected field was observed retracting away from the reconnection site: “This accelerated field forms a pair of three-dimensional, arched flux tubes whose cross sections have a distinct teardrop shape. We found that the velocities of these flux tubes are smaller than the reconnection Alfvén speed predicted by the theory, indicating that some drag force is slowing them down.” Alternatively, plasma compressibility can reduce the speed of reconnection outflow (Priest & Forbes 2000 [35]). We show below that the observations do not appear to support an interpretation based on compressibility.

The sizes of the teardrop-shaped outflows of Linton & Longcope (2006 [25]) are determined by the duration of a given reconnection episode and by the size of the patch of enhanced resistivity. From the SAD observations, the sizes of the plasma voids can be directly measured and utilized as constraints in the model: ideally, the model would produce a distribution of outflowing flux tubes that mimics the distribution found in the observations. Additionally, their speed profiles (including acceleration/deceleration) may eventually be useful for understanding the nature of any drag forces.

Nearly all that is known about the supra-arcade region is of a qualitative nature. There is not in the literature any collection of the statistics of SADs. To be useful as constraints for the models, the observations must yield quantitative measurements

with estimable uncertainties. Whereas most of the preceding literature about supra-arcade downflows has focused on their mere presence (e.g., McKenzie 2000 [29]), the fact that they are voids (Innes et al. 2003a [14]), or their timing in relation to nonthermal energy release (Asai et al. 2004 [1]; Khan et al. 2007 [17]). In this chapter we report observational quantities from a sample of plasma voids in three flares, quantities which are potentially useful as model inputs or constraints. [For the 2002 April 21 flare, downflowing loops are considered as SADs in this chapter; however, they will be considered separately in Chapter 4.] The distributions of observed void sizes and speeds are displayed. We combine the measured sizes with a model of the magnetic field in the supra-arcade region to yield estimates of the magnetic flux in individual flux tubes. We believe that these flux estimates—while admittedly subject to observational and model-dependent uncertainties—represent the first empirical estimates of the characteristic flux participating in individual reconnection events.

Linton & Longcope (2006 [25]) demonstrated that the energy released by the shrinkage of a flux tube accounts for a significant portion of the total energy released by an individual reconnection. Linton & Longcope (2006 [25]) indicate that for small reconnection regions, the energy released by the loop shrinkage may in fact be considerably larger than the energy directly released by magnetic reconnection. Hudson (2000 [13]) conjectured that magnetic structures must contract (or “implode”) as a consequence of energy loss, and provided an upper limit on the energy accessible via implosion. In this chapter, we utilize the paths of the downward motions of plasma

voids and an estimate of the fluxes in each of the shrinking flux tubes to make an empirical estimate of this energy. Except for the approximation of change in volume, our expression for the shrinkage energy is mathematically equivalent to Hudson's. To our knowledge, this is the first time that flare observations have been used to derive empirical estimates of this particular mode of energy release.

2.2. Automated Detection Algorithm

For this project, semi-automated software for detection and measurement of SADs has been developed. The effort was motivated by a desire to measure reliably and objectively the characteristics of SADs in a large number of flares, with repeatable results. In Innes et al. (2003a [14]) and in Sheeley, Warren, & Wang 2004 [46]), SADs are displayed via sloped traces in stackplots constructed from slices of the images. The difficulties in automating this technique are significant. (1) The method requires pixels to be extracted from a virtual slit placed along the trajectory of the downflow, requiring prior knowledge of the existence and location of the downflow; so it is most appropriate for demonstrating the existence of a downflow, not for automatically detecting the downflow. (2) With the stackplot, automated measurements of the void's area are not provided; the area must be measured manually. (3) To detect downflows automatically with stackplots, the virtual slit must be placed across the paths of the suspected downflows, like a "finish line" parallel to the limb. This was done in Innes et al. (2003a [14]). The insurmountable problem is that in low-cadence

image sequences, fast-moving voids can skip over the virtual slit and thus fail to be detected crossing the “finish line”. For these reasons, an improved and automated method is warranted.

Our detection routine finds plasma voids in a flare movie by searching for locally depressed signals (“troughs”) in each image, and then attempting to match trajectories extending over some user-defined minimum number of images. To detect a trough in a given image, the program identifies any contiguous group of pixels that is darker than a user-specified threshold amount. When a trough exceeding a predefined minimum size is identified, the positions of all its constituent pixels are recorded, as is the position of the trough’s centroid. This process is repeated for each image in the movie.

The next step is to determine whether the positions in consecutive images trace out trajectories of *moving* troughs. Two key assumptions are applied: (i) Only trajectories that indicate motion towards the flare arcade are accepted. (ii) Trajectories comprising fewer than N position points are rejected, with N typically set to 4. The former assumption reflects our present focus on supra-arcade downflows, but could be removed for searches of flows directed away from the Sun. The latter assumption is intended to ensure reliability of the results. We find that troughs observed in fewer than 4 successive images are more likely to be false detections. (For reference, in the three flares considered in this chapter, the number of position points for each visually verified trough ranges from 3 to 41.) One result of this conservatism is that

the fastest SADs may be overlooked, as they can pass through the field of view in just two or three frames. For the 2002 April 21 flare (see below), assuming $N = 4$ and a cadence of 1 image per thirty seconds, SADs traveling faster than $\sim 1600 \text{ km s}^{-1}$ could have passed undetected. For the 2000 July 12 flare (also below), similar considerations imply a maximum detectable speed of $\sim 1800 \text{ km s}^{-1}$. To compensate for gaps in the data sampling, as well as for momentary disappearances of voids due to, e.g., temporary increases in data noise, trajectories shorter than N points may be combined if the velocities (speed and direction of the trough) before and after the dropout are consistent.

All the trajectories meeting the above criteria are displayed for the user, with movie clips from the relevant image frames, to allow visual inspection and rejection of any false trajectories. Although the routine has been designed to find as many full-length tracks as possible, the noise in the region of interest makes this very difficult; therefore, manual tracking is enabled in order to allow the user to add to the automatically-detected troughs. Upon acceptance by the user, the trajectories of detected troughs can be fitted with polynomials to obtain velocity and acceleration estimates. An additional product of the analysis is automated determination of the size of each plasma void, by counting the number of pixels associated with each trough and scaling by the telescope's angular resolution.

The routine has been refined through repeated application to synthetic flare data which mimic the appearance of downflows within a background of white noise. The

noise level and parameters of the artificial voids (e.g., size, speed, and darkness) have been varied for the refinement of the analysis software. An example frame from one synthetic data sequence, designed to mimic the very low signal-to-noise ratio of the SXT downflow movies (significantly noisier than the TRACE data), is shown in Figure 5(a).

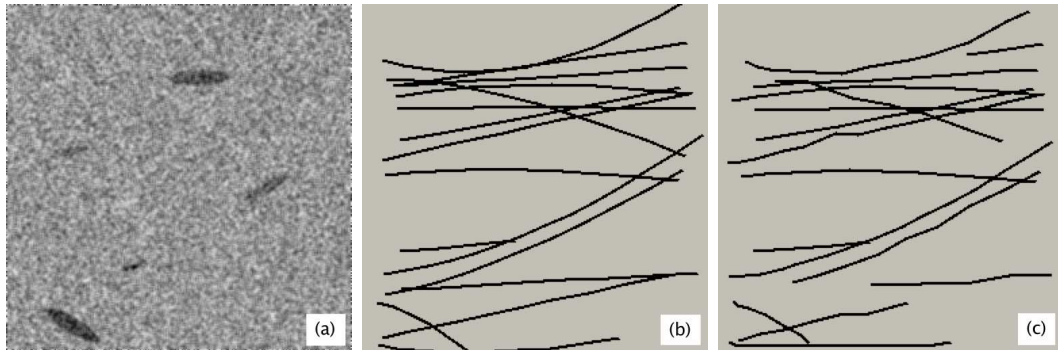


Figure 5: Testing the semi-automated software with an SXT-mimic synthetic data set. (a) Five artificial voids are seen in this frame. A total of sixteen voids were created in this 50-frame movie. The actual trajectories of all 16 are shown in panel (b), and the trajectories as determined by the software are in panel (c).

In all tests of synthetic data, the routine was able to detect all the troughs; refinements to the software allowed elimination of false positives. Figure 5(b) and (c) demonstrate the trajectories of voids in the SXT-mimic synthetic data.

We note that in addition to the dark plasma voids, shrinking loops are often observed. These X-ray or EUV-emitting loops are observed in the same supra-arcade region with the plasma voids, often during the same time intervals, and moving at similar speeds. These loops appear to get brighter as they approach the top of the

arcades. In such cases, it would appear that the ‘bright shrinkages’ are observed because chromospheric evaporation fills the loops before/as they shrink, whereas voids appear dark because they are shrinking before evaporation has filled them. For this dissertation we focus on the plasma voids, rather than the ‘bright shrinkages’, primarily because they are observationally easier to distinguish from the bright loops in flares.

2.3. Analysis of Solar Flare Data

The automatic detection routine has been applied to image sequences from three SAD flares, summarized in Table 1. All three were accompanied by CMEs. The X1.5 flare of 2002 April 21 was observed by TRACE, RHESSI, SOHO, and numerous other observatories (e.g., Wang et al. 2002 [59]; Innes et al. 2003a [14]). The 1999 January 20 M5.2 flare was observed by *Yohkoh*/SXT, and was the discovery event for downflows; this flare was described extensively in McKenzie & Hudson (1999 [30]) and in McKenzie (2000 [29]). The M5.7 flare of 2000 July 12 was observed by SXT. The TRACE images from 21-Apr have angular resolution of 0.5 arcseconds per pixel, whereas the 12-Jul and 20-Jan images were made in SXT’s half-resolution mode, corresponding to 4.91 arcseconds per pixel. As a result, the smallest of the voids seen by TRACE would have been completely undetectable by SXT; this is borne out in the histograms of detected voids (see below). In all three flares, supra-arcade downflows were faintly visible in the raw images; the images were processed

for contrast enhancement (flattened, run-mean-differenced, and byte-scaled) prior to application of the SAD-tracking routine.

Table 1: Summary information of flares analyzed in this chapter.

Date	GOES start, peak [UT]	GOES Classification	Source	Time Span of Analysis (UT)	Approximate Position
2002 April 21	00:43, 01:51	X1.5	TRACE (195Å)	01:32–02:26	82W 16S
1999 January 20	19:06, 20:04	M5.2	SXT	20:36–21:28	85E 29N
2000 July 12	18:41, 18:49	M5.7	SXT	21:14–21:53	72W 16N

Note that all positional information is provided based upon the centroid of a trough location. Theoretically, tracking the head of the trough would constitute a more accurate assessment of its position because the centroid position may include portions of the growing wake behind the actual shrinking loop which could cause the velocities to appear slightly smaller. However, the automated routine relies on thresholds to determine the areas, and since each image is at least slightly different – especially when the exposure durations vary – the heads become much less reliable positions than the centroids. Because the areas are all the same for the manual routine, the centroid and head positions are merely shifted from one another.

By fitting a parabolic polynomial to the trajectory of each void, the speeds and accelerations of each void can be measured. The accelerations are generally small, however, and subject to uncertainties in the position points. This is particularly true for cases where the automatically determined trajectories are noisy and span only a

few position points. The plots in Figure 6 show the time profiles of the locations of two SADs from the 21-Apr flare, to demonstrate the range of scatter in the SAD trajectory determinations. Here, we have averaged the speed of each plasma void over its full measured trajectory, rather than presenting the velocities and accelerations derived from polynomial fits. The de-projected path-averaged speeds reported herein range from 30 to 470 km s⁻¹. In Chapter 4 we explore the distribution of velocities more deeply, including accelerations and the spatial/temporal variations in SAD speeds from a larger number of flares. The purpose of reporting speeds in this chapter is primarily to demonstrate the capability of the detection scheme.

Similarly, the void sizes reported in histograms below (Figure 11) are averaged over the lifetime of each detected downflow.

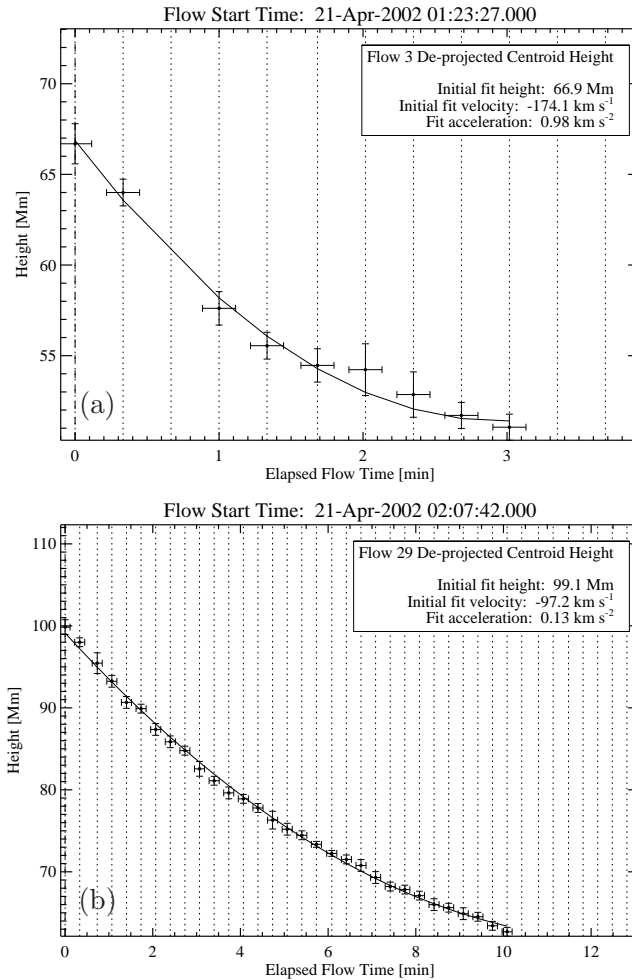


Figure 6: Example trajectories from two SADs detected in the 21-Apr flare, demonstrating the range of uncertainty in the trajectory determinations. Panel (a) is a SAD with one of the noisier trajectories while (b) has very little scatter in the automatically determined trajectory. Velocities and accelerations can be derived from polynomial fits to the trajectories (as shown in the legends); however, for this chapter, only path-averaged speeds are reported. The error bars are derived by assigning an uncertainty to the positions as the square root of the diameter of the trough (or square root of the largest extent in the case of a non-circular trough).

2.3.1. 2002 April 21, TRACE data

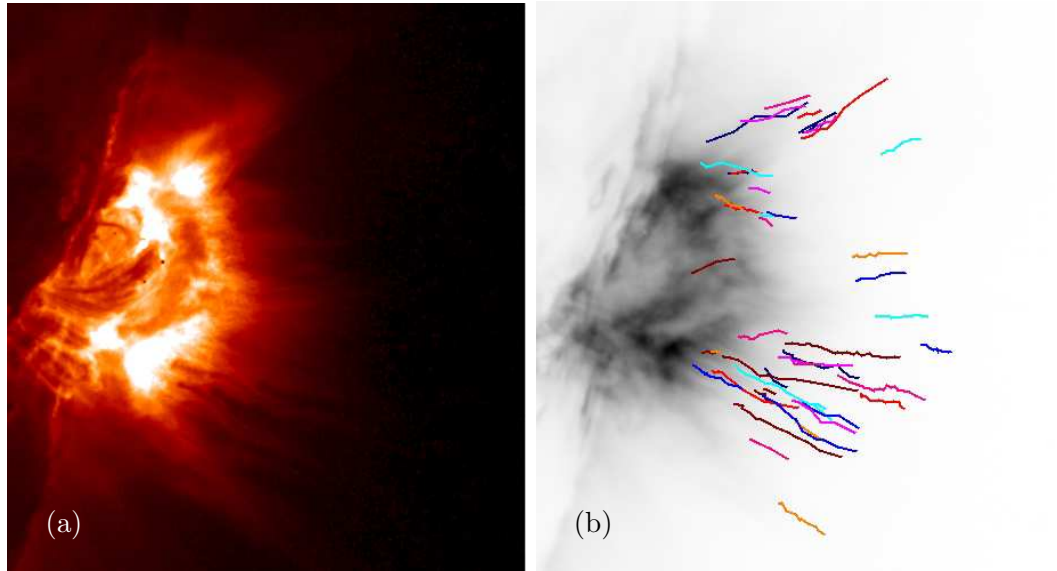


Figure 7: (a) The famous flare of 2002 April 21 revealed downflows in TRACE and SUMER for the first time, and represents one of the sharpest observations of downflows. (b) Downflows detected in the 21-Apr flare, tracked by the automated routine and supplemented with manually-tracked flows.

In the TRACE data from 2002 April 21 (Figure 7(a)), the automated detection routine tracked 23 SADs which have been manually verified by visual inspection. An additional 25 SADs were tracked completely manually. The trajectories of all of the detected downflows are plotted in Figure 7(b). Although SADs descending into the southern part of the arcade were most obvious, and have been described elsewhere, the automated routine detected downflows above other parts of the arcade during the later part of the rising phase of the flare. De-projected average speeds of the downward motions range from 45 to 436 km s⁻¹ (Figure 10(a)). The median speed is 101 km s⁻¹. Figure 11 shows the sizes of the detected X-ray voids. The median of

the average areas of those flows detected using the automatic threshold technique is $3.6 \times 10^6 \text{ km}^2$.

2.3.2. 1999 January 20, SXT data

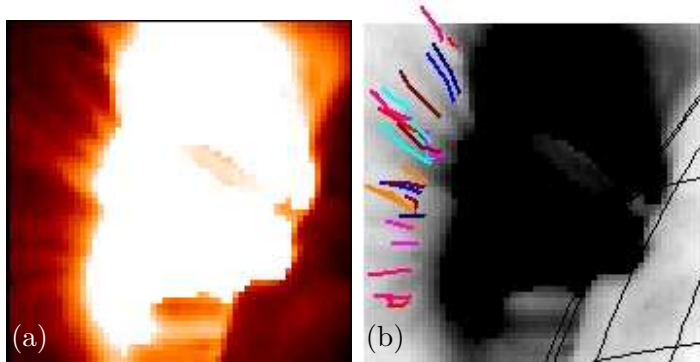


Figure 8: (a) Image taken from the 20-Jan flare. (b) Enhanced image overlaid with downflow detections, tracked by the automated routine. The solar limb is at right; the arcade itself is obscured by pixel saturation. The center of the FOV moves by several arcseconds throughout the course of the observations. This shifting accounts for the northern track beyond the FOV for the selected overlay image.

In the SXT data from 1999 January 20, 25 downflows were found above the arcade. The trajectories of the detected downflows are plotted in Figure 8. The downward speeds in this flare are very similar to those in the 21-Apr flare (Figure 10(b)); de-projected path-average speeds range from 30 to 264 km s^{-1} , the median speed being 106 km s^{-1} . Due to the much coarser angular resolution of SXT compared to TRACE, and the very noisy signal in the flare images, none of the smaller SADs are detected: the median area among these SADs is $42 \times 10^6 \text{ km}^2$ (Figure 11(b)).

2.3.3. 2000 July 12, SXT data

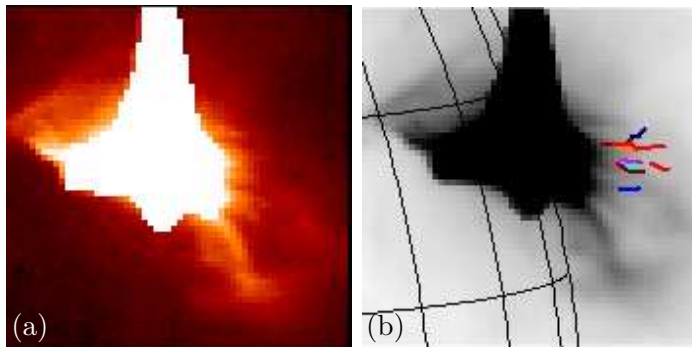


Figure 9: (a) Image taken from 12-Jul flare. (b) Enhanced image overlaid with downflow detections, tracked by the automated routine. The solar limb is at left.

In the SXT data from 2000 July 12, 10 downflowing voids were tracked and manually verified; the trajectories are displayed in Figure 9. As in the 20-Jan flare, the detected plasma voids are larger than those in the 21-Apr flare; the median area is $30 \times 10^6 \text{ km}^2$ (Figure 11(c)). This follows as a result of the vast difference in angular resolutions used for the respective images. The downflow speeds are shown in Figure 10(c). De-projected path-average speeds range from 53 to 470 km s^{-1} ; the median speed is 146 km s^{-1} .

Figure 11 demonstrates that in each flare a range of void sizes are detected. There is disparity between the three distributions in Figure 11—the TRACE images apparently reveal no voids larger than $10 \times 10^6 \text{ km}^2$, which are seen in the SXT flares. In an attempt to evaluate whether this disparity is related to the difference in angular resolution, we have rebinned the TRACE data to 2.5 arcsec/pixel to approximate the

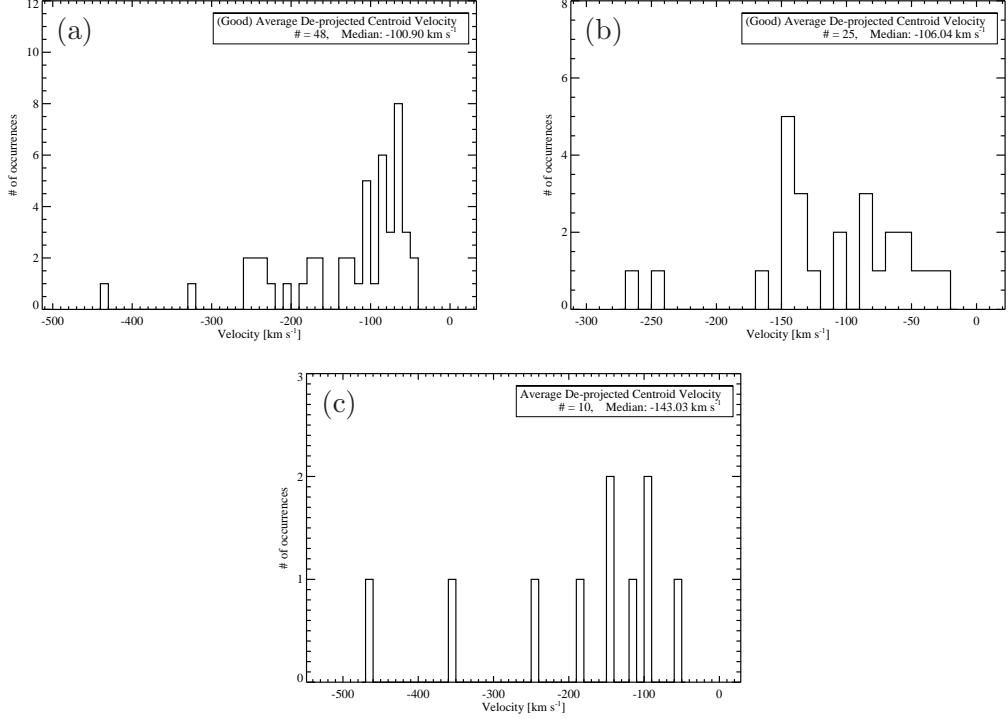


Figure 10: Distribution of average de-projected speeds found in the detected downflows- (a) 21-Apr flare, (b) 20-Jan flare, (c) 12-Jul flare. (The “Good” labels in the legends of (a) and (b) indicate that some detected flows were manually rejected from the final output set.)

SXT full-resolution pixel size, and to 5 arcsec/pixel to approximate the SXT half-resolution pixel size. We observe in the unbinned TRACE images that it is possible to distinguish between the ‘tail’ of a SAD and the slightly darker plasma void. When the images are rebinned to coarser angular resolutions this void/tail distinction is quickly destroyed. The result is that SADs in the rebinned data are given areas that include part of the ‘tail’. The largest of the 2.5-arcsec-binned SADs is $\sim 40 \times 10^6$ km², similar to the median area found in the 12-Jul flare; the mode of the binned SADs is $\sim 10 - 20 \times 10^6$ km². As the angular resolution of the images is further

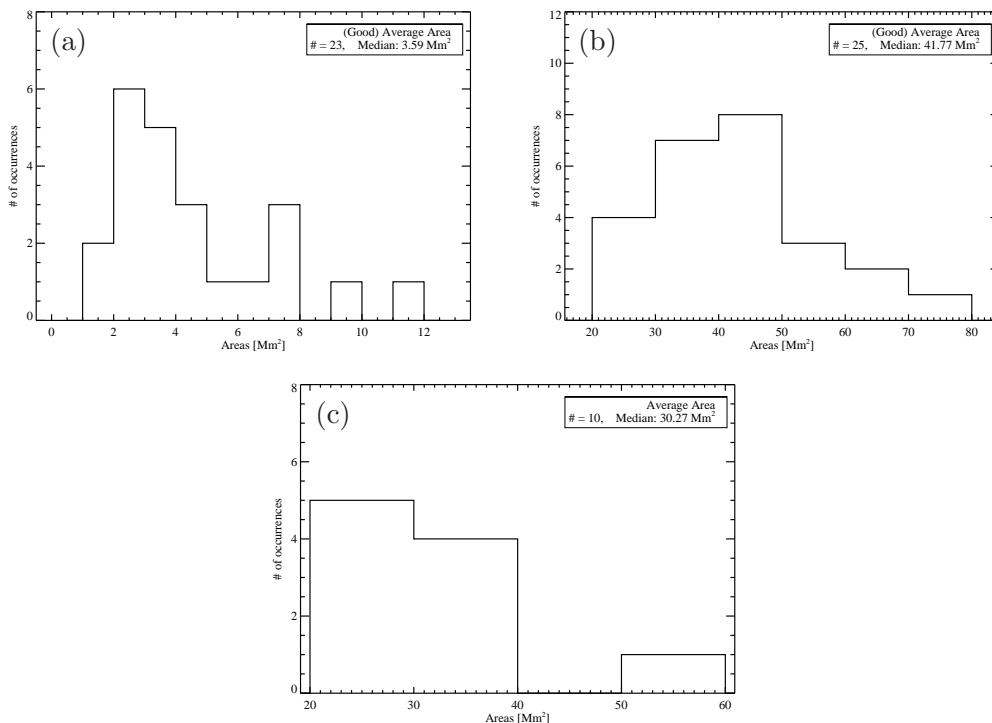


Figure 11: Distribution of average areas found for the detected downflows: (a) 21-Apr flare, (b) 20-Jan flare, (c) 12-Jul flare. Only those flows detected with the automatic threshold routine were included in (a).

degraded, the voids become entirely undetectable. The brightness contrast between the voids (including the ‘tails’) and the surrounding supra-arcade plasma is too low to allow the SADs to stand out in images where the angular width of a pixel is greater than the width of the SADs. In the 5-arcsec-binned TRACE data, the voids are virtually undetectable, to the degree that no measurements of size or speed are possible. Exactly the same effect is seen in the quarter-resolution flare images from SXT (9.8 arcsec/pixel), for nearly all flares observed by SXT.

From this exercise we conclude that some of the areas measured in SXT images may include contributions from the SAD ‘tails’ due to greater difficulty in separating ‘tail’ from void. We see no reason why TRACE would not have detected voids as large as $30 \times 10^6 \text{ km}^2$ or larger, if they had been present in the 21-Apr flare. At the same time, we remark that each flare is different, and each may have a different range of SAD sizes.

2.4. Discussion: Relation to Reconnection

It is generally accepted that magnetic reconnection is responsible for either the initiation or dynamical progression of CMEs and eruptive flares. Reconnection is the central component in the two-dimensional model due to Carmichael (1964 [2]), Sturrock (1968 [50]), Hirayama (1974 [11]), and Kopp & Pneuman (1976 [19]), sometimes called the CSHKP model, which continues to form the organizing element of much CME and flare research (see, for a summary, Shibata 1999 [47]). It is a testament to this model that decades of observations and numerical simulations have not overturned it or even changed its basic form. In this section we consider the measured characteristics of SADs in relation to quantities pertinent to reconnection.

2.4.1. Measured Speeds

The observed SAD speeds are slow in comparison to the 1000 km s^{-1} that is often assumed for the Alfvén speed. For an estimate of the Alfvén speed in the present flares, we utilize a PFSS magnetic field extrapolation (see below). At the locations

of the detected SADs the field strengths range between 5 G and 87 G (median, 17 G). Assuming a plasma density of 10^9 cm^{-3} (see Fletcher & Hudson 2008 [6], and references therein), we infer Alfvén speeds of 350–6000 km s^{-1} (median, 1200 km s^{-1}). Most of the downward motions thus appear to be sub-Alfvénic. The magnetic field strength estimates and slow flow speeds are further explored in Chapter 4 (particularly Sections 4.2.4 and 4.2.3).

Linton & Longcope (2006 [25]) suggest that sub-Alfvénic outflows may result from drag forces. Although no attempt has been made in this chapter to estimate quantitatively the drag forces necessary to produce these speeds, the snowplowing suggested by Linton & Longcope (2006 [25]) could lead to enhanced density in front of the shrinking loop. (See Sections 3.3.2 & 4.2.4 below for flow drag analysis.) Enhanced *emission* ahead of SADs has been noted by previous authors (e.g., Sheeley & Wang 2002 [44]; Innes et al. 2003b [15]), though identification of this emission enhancement with snowplowing is highly speculative.

Alternatively, plasma compressibility can reduce the speed of reconnection outflow (Priest & Forbes 2000 [35]), by a factor of $(\rho_i/\rho_o)^{1/2}$, where ρ_i (ρ_o) is the density upstream (downstream) of the reconnection. Comparison of the detected speeds ($\sim 30\text{--}470 \text{ km s}^{-1}$) to the median estimated Alfvén speed ($\sim 1200 \text{ km s}^{-1}$) suggests reduction factors of 3–40 (i.e., detected speeds are $0.03 - 0.4v_A$). Such reductions would require density increases of 9–1600. Most flows have speeds near $\sim 100 \text{ km s}^{-1}$ which corresponds to a density increase on order of 150. The observed low density

in plasma voids (Innes et al. 2003a [14]), and lack of emission, are incompatible with density increases of such large magnitudes, suggesting that compressibility plays a negligible role.

2.4.2. Observed Sizes

In Linton & Longcope (2006 [25]) the size of the teardrop-shaped outflow is determined by the duration of a given reconnection episode and by the size of the patch of enhanced resistivity. The observed size distribution of downflow features may be useful for adjusting the parameters of such models.

We have already seen that SXT does not detect the smaller voids which are observable with TRACE, and we consider it likely that some plasma voids exist that are smaller than even TRACE can resolve. While the full range of possible diameters cannot be explored at present, we can explore the large-diameter end of the distribution. The histograms in Figure 11 demonstrate that for each flare a range of sizes exists, indicating that patches of reconnection may be found in a range of sizes. It is worth noting that the areas observed in these three flares are similar to the cross-sections of reconnecting loops observed in TRACE by Longcope et al. (2005 [28]), wherein the median loop diameter was 3.7 Mm.

2.4.3. Estimation of Reconnecting Flux

The magnetic fields in the vicinity of the flares were retrieved from the PFSS extrapolations calculated by Dr. M. DeRosa (Schrijver & DeRosa 2003 [42]), provided within the SolarSoft (Freeland & Handy 1998 [8]) environment. The latitude, longitude, and height of the first detection of each plasma void were calculated by associating each void with a footpoint location, and by correcting the height for the effect of projection onto the plane of the sky. Because of the lack of obvious ‘legs’ traceable from the voids down to the photosphere, the assignment of footpoint location introduces some uncertainty. The first attempt to assign void footpoints is based upon an extrapolation of the void’s trajectory down to visually determined flare ‘ribbon’ locations. If this method results in non-reliable footpoint locations (typically due to incomplete tracks), then one footpoint location derived manually, by comparing the set of void images with magnetograms, is applied universally to the flare. The heliographic latitude and longitude of the footpoint was then assigned to the void. The PFSS field strength at the position of the first detection of each plasma void was multiplied by the apparent size of the void to yield an estimate of the magnetic flux within the shrinking flux tube. Flux estimates are summarized in the histograms of Figure 12. Of the fluxes assigned to each downflow in the 21-Apr flare, the mean is 9.0×10^{17} Mx, the standard deviation of the sample is 8.4×10^{17} Mx, and the median is 6.8×10^{17} Mx. (SADs and SADLs are included in the calculations for the 21-Apr

flare. It should be noted, however, that the SADL areas are assigned manually instead of using thresholds. This results in areas that are typically at the low end of the SADs range.) For the 20-Jan flare, the mean flux is 2.8×10^{18} Mx, the standard deviation of the sample is 1.1×10^{18} Mx, and the median is 2.3×10^{18} Mx. In the SADs of the 12-Jul flare, the mean flux is 6.0×10^{18} Mx, the standard deviation of the sample is 0.4×10^{18} Mx, and the median is 4.4×10^{18} Mx. (The east limb calculations for the 20-Jan flare are weaker and less reliable due to less current magnetographic data. This issue is discussed in detail in Section 4.1.2.)

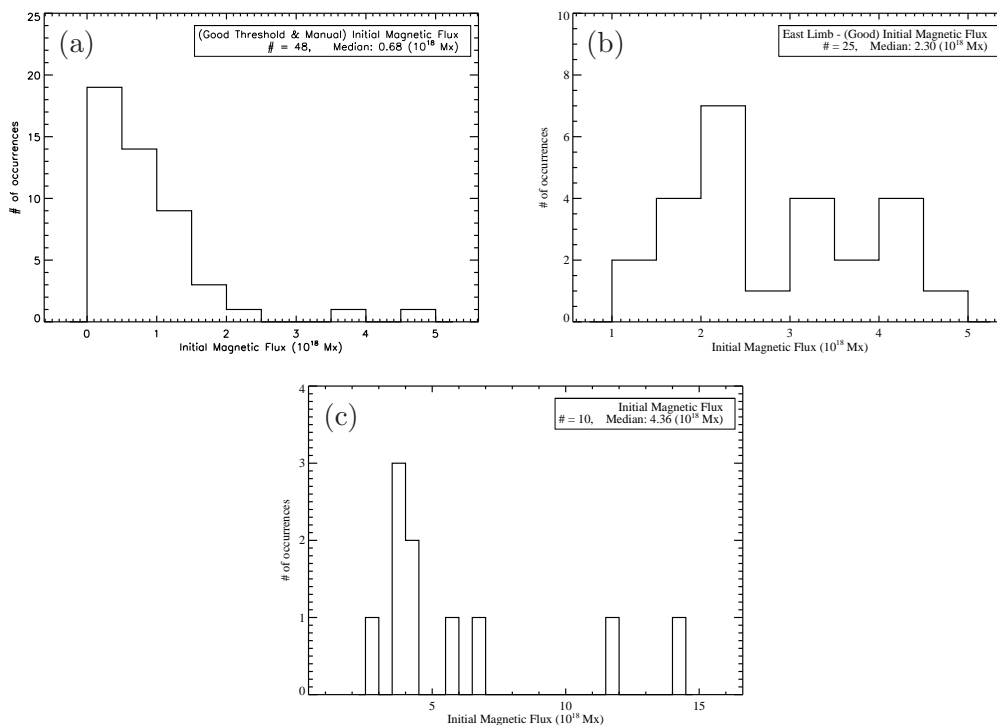


Figure 12: Distribution of magnetic fluxes found for the detected downflows: (a) 21-Apr flare, (b) 20-Jan flare, and (c) 12-Jul flare.

Potential sources of error in calculation of the magnetic fluxes include the initial height of each SAD above the photosphere, the cross-sectional area of its associated flux tube, and the strength of the magnetic field.

The height of the reconnection event forming each shrinking flux tube is uncertain, due to noise in the images, threshold of the detection scheme, and projection effects (which we have tried to counter). Additionally, it is necessary to interpolate within the PFSS model to estimate the field strength at a given void's location. At the initial height of the flows ($\sim 40 - 120$ Mm), the magnetic field strength varies smoothly, so that errors in the height of the void, or in the location of the footpoint, cause uncertainties on the order of 5–20 percent of the field strength. An additional potential source of error is the fact that we assign a value corresponding to the height of *initial detection*, which is not necessarily the height of formation of the flux tube. As this height is a lower limit on the actual height of the reconnection site, it affects the flux determination because magnetic field strength falls with height. By underestimating height we may be overestimating flux. If the flux tubes are in pressure equilibrium, then the flux should remain the same at any height with the cross-sectional areas compressing to account for the increase in magnetic field; however, our area measurements are not precise enough to properly measure the change in area. We use the area of a trough as a proxy for the cross-sectional area of the flux tube. The trough's area can be affected by noise in the images, as well as the sensitivity threshold of the detection. It is difficult to say whether this is systematically over- or underestimating

the area, but we consider the area estimate to be accurate to within about 25 percent. We arrived at this estimation by repeatedly analyzing each of the flares, varying the threshold each time. The relative variation in the number of pixels identified with a given trough never exceeded 25 percent. We do not consider the effects of photon scattering in the telescopes, or the instrument point spread function. Both scattering and a finite point spread function reduce the contrast in the images, and could result in underestimating the area of a trough. Such effects are small in the SXT and TRACE images, and the associated uncertainty in the trough area is within the amount found by varying the detection thresholds.

The magnetic field estimate is derived from a PFSS extrapolation. The potential field extrapolation will tend to underestimate the strength of the magnetic field at heights above the active region, but a bigger source of uncertainty is the fact that these flares are at the limb. Since magnetograms are unreliable near the limb, the PFSS extrapolation employed uses only magnetograms within 55 degrees of disk center, and then uses differential rotation and a surface transport code to model how the magnetic field evolves over the three days required to arrive at the limb. We consider that the PFSS field strength estimate is probably accurate to better than 30 percent, based on the following argument: In a recent analysis of nonlinear force-free field extrapolations for four flaring active regions, Regnier & Priest (2007 [38]) calculated the free energy in the nonlinear force-free fields, figured as the energy above that in the corresponding potential field, i.e., $\Delta E = E^{nlf} - E^{pot}$. According to Priest (private communication),

these free energies ranged from $\Delta E/E = 0.023$ to $\Delta E/E = 0.65$, indicating differences in magnetic field strength of roughly $\Delta B/B = 0.01 - 0.3$. Thus the 30 percent uncertainty assigned to the PFSS field strength is reasonably conservative.

We note the similarity of the fluxes found here to that estimated by Longcope et al. (2005 [28]). In that work, reconnection appeared to proceed in “parcels of $\sim 4 \times 10^{18}$ Mx at a time.” It is difficult to say how much credence should be given to this similarity, because we know of no prediction in the literature of the amount of flux expected to participate in individual reconnection episodes. The results of performing this measurement on a larger number of flares are presented in Chapter 4, namely Section 4.2.1.

2.4.4. Inferred Reconnection Rate

Key to understanding the magnetic reconnection mechanism in flares is knowledge of the amount of magnetic flux that is processed over time—the reconnection rate. The reconnection rate has been measured indirectly by mapping the motions of chromospheric ribbons across magnetograms to determine the amount of flux that is input to reconnection (Saba et al. 2001 [39]; Fletcher & Hudson 2001 [5]). In observations, the ribbons appear to move across photospheric flux at rates that vary along their lengths (Saba et al. 2001 [39]) and between polarities (Fletcher & Hudson 2001 [5]).

Another scheme for estimating the reconnection rate focuses on apparent reconnection inflows; see particularly Yokoyama et al. (2001 [61]) and Narukage & Shibata (2006 [32]). These authors report reconnection rates on the order of $M_A \simeq 0.001 - 0.07$. In this notation, the reconnection rate is expressed as an Alfvénic Mach number, but we can employ these authors' estimated field strengths, etc., to derive the amount of magnetic flux processed over time. Yokoyama et al. (2001 [61]) suggest magnetic field strengths of 12–40 G, and inflow speeds of $v_{in} \simeq 1 - 5 \text{ km s}^{-1}$, with a characteristic length scale of $L = 1.5 \times 10^5 \text{ km}$ (corresponding to the assumed extent of the reconnection zone along the axis of the flare arcade, and roughly equal to the length of observed flaring loops). With these parameters, an alternative expression of the reconnection rate is given by $Bv_{in}L \simeq (2 - 30) \times 10^{16} \text{ Mx s}^{-1}$. Given the uncertainties in the quoted measurements and characteristic length scale, we present this estimate of the reconnection rate only as a demonstration of the relevant order of magnitude—the point to take away is that the reconnection rate can be on the order of a few-to-tens of $10^{16} \text{ Mx s}^{-1}$. In comparison, the reconnection rate observed by Longcope et al. (2005 [28]) in a flurry of reconnection between two active regions was estimated as $(0.15 - 5) \times 10^{20} \text{ maxwells}$ over 3.5 hours, or $(0.1 - 4) \times 10^{16} \text{ Mx s}^{-1}$.

The flux estimates derived above and the times of detection of each SAD seem to indicate that, in the 21-Apr flare, approximately $4.8 \times 10^{19} \text{ maxwells}$ of flux was processed over a period of roughly 64 minutes. This implies a reconnection rate of $1.2 \times 10^{16} \text{ Mx s}^{-1}$. For the 20-Jan flare, $\sim 7.0 \times 10^{19} \text{ Mx}$ was processed in

144 minutes, for a reconnection rate of $0.8 \times 10^{16} \text{ Mx s}^{-1}$. In the 12-Jul flare, approximately $6.1 \times 10^{19} \text{ Mx}$ was processed in 35 minutes, for a reconnection rate of $2.3 \times 10^{16} \text{ Mx s}^{-1}$. These reconnection rates are comparable to Yokoyama et al. (2001 [61]) and to Longcope et al. (2005 [28]).

At any rate, these large eruptive flares certainly process more than a few $\times 10^{19}$ maxwells of flux. However, such an accounting is not the objective of this study, and we make no attempt to describe the total energy budget of a flare. What the present observations can do, though, is provide empirical estimates of the physical scales of 3D patchy reconnection in solar flares, the speeds of outflow, and the fluxes involved. The “flare ribbons” technique used by Fletcher & Hudson (2001 [5]) has the potential strength, in principle, of capturing the total amount of flux reconnected during the flare, whereas the method described here only captures the flux tubes observable as downflows. On the other hand, the “downflows method” will necessarily count only flux reconnected in the supra-arcade region (i.e., it does not count flux reconnected to other structures outside the flaring region). Furthermore, the technique allows one to infer the sizes of flux tubes, possibly the sizes of diffusion patches, the discrete amounts of flux participating in each “parcel”, and put limits on the heights of the diffusion patches above the photosphere. We consider the two techniques to be complementary, the “flare ribbons” method more appropriate near disk center where magnetograms are better, and the “downflows” method more appropriate near the limb.

2.4.5. Shrinkage Energy

Lastly, the relaxation of tension in the reconnected flux tube appears to be a significant source of energy release, perhaps more so than the flux annihilation itself. This energy release was observed in the simulation of Linton & Longcope (2006 [25]), and may be required by Hudson’s 2000 [13] implosion conjecture. The SAD observations can be utilized for an estimate of the scale of this energy. We assume an energy density of $B^2/8\pi$, and a change in flux tube volume of $A\Delta L$. Conserving flux in the shrinking tube, the energy transfer associated with shrinkage is given by

$$\Delta W = B^2 A \Delta L / 8\pi. \quad (2.1)$$

This is equivalent to Hudson’s (2000) [13] expression for the upper limit on available energy, except for a difference in the estimated change in volume—Hudson used $4\pi(\Delta t v_A)^3/3$, where Δt represents the relevant timescale for energy release. As an upper limit on the volume change, Hudson (2000 [13]) let the volume retract symmetrically at the Alfvén speed.

Empirical estimates of ΔW are given in Figure 13, where we have assigned A to the area of each SAD at the time of its initial detection, and ΔL to the change in its height over the course of shrinkage. A more complete understanding of the geometry of each flux tube might allow a more accurate estimate of the change in length; the present association of ΔL with change in height will suffice for an order-of-magnitude estimate. The median ΔW for the 21-Apr, 20-Jan, and 12-Jul SADs are 1.2×10^{27} ergs, 1.6×10^{27} ergs, and 4.8×10^{27} ergs, respectively. Summing these

over the total sample of SADs in each of the flares yields $10. \times 10^{28}$ ergs, 4.7×10^{28} ergs, and 6.7×10^{28} ergs, respectively. These energies are clearly not indicative of the total energy associated with the impulsive phases of the flares, but should be taken as evidence of significant energization throughout the lifetime of the flares.

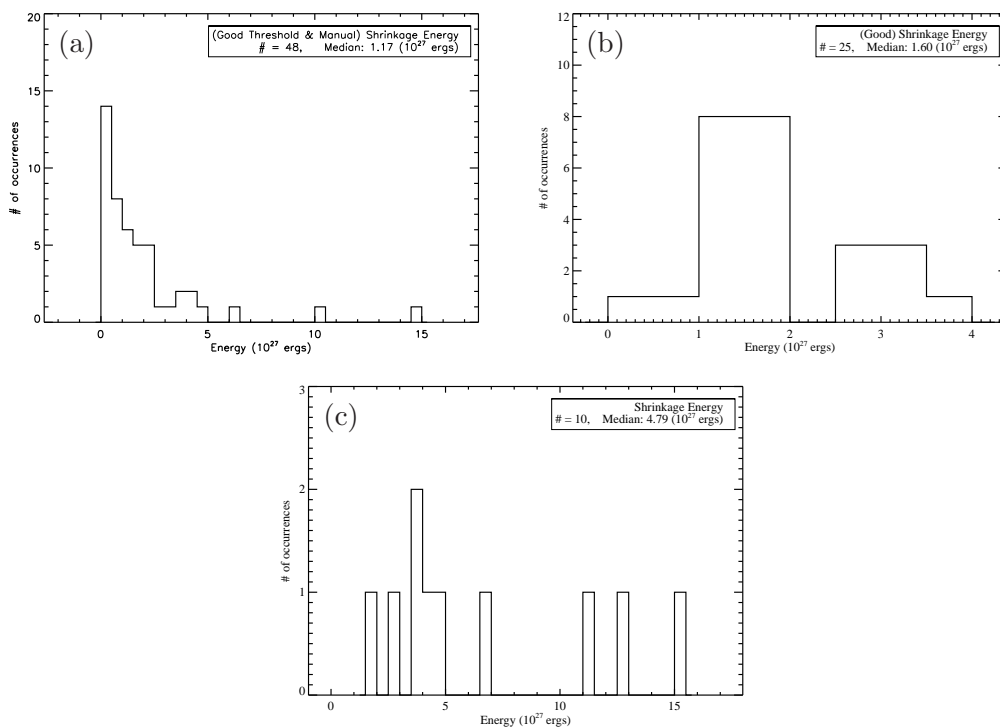


Figure 13: Energies calculated for loop shrinkage: (a) 21-Apr flare, (b) 20-Jan flare, and (c) 12-Jul flare.

2.5. Conclusion

In a coarse description, ‘reconnection’ means that a new magnetic connection is formed and an old connection abandoned. But the high conductivity of coronal plasma implies magnetic diffusion times much longer than the typical timescales of

flares, so how can these new connections be allowed on timescales that are relevant? An answer that has been offered, paraphrasing Sweet (1958 [54]), Parker (1963 [33]), Petschek (1964 [34]), Jaggi (1964 [16]), and many others since, is that in a localized region, resistivity may increase for a short time, so that reconnection can happen. But what exactly are the meanings of “localized” and “short time”? One must answer these questions to build a model of reconnection that can be compared to observations, or a model that actually predicts something. The observations discussed herein provide some tentative answers to these questions. Localization is addressed by the automated detection of SADs, providing the latitude, longitude, and a lower limit on the height. The duration of the reconnection episode may be related to the cross-sectional area of the outflowing flux tube (Linton & Longcope 2006 [25]).

For SADs of the ‘plasma void’ type in three flares observed by TRACE and SXT, we have derived empirical estimates of speeds, sizes, and included magnetic flux (see Figure 14). We believe these estimates, though model-dependent, are potentially useful as inputs/constraints for models of 3D reconnection. Measured cross-sectional areas are typically 10^7 km^2 , with significant range for variation. De-projected path-averaged speeds range from approximately 30 to 470 km s^{-1} , and are sub-Alfvénic. Combination of the SAD observations with magnetic modeling—in this case a PFSS model—yields an estimation of the flux in each shrinking flux tube. For three flares, the median flux in a shrinking tube is on the order of 10^{18} Mx . The energy associated with loop shrinkage appears to be of a significant magnitude; the present observations

suggest $\Delta W \sim 10^{27}$ erg per loop shrinkage, and reconnection rates on the order of 10^{16} Mx s^{-1} . To our knowledge, these are the first empirical estimations of the flux participating in individual reconnection episodes, and of energy released by shrinkage, via measurements of post-reconnection flux tubes. It is hoped that 3D models of patchy reconnection will provide predicted distributions to which the observations can be compared.

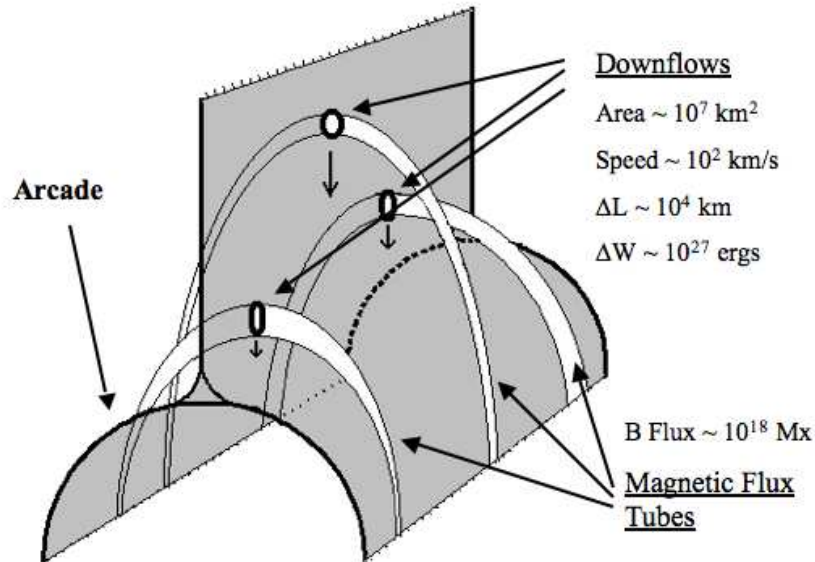


Figure 14: Cartoon depiction of supra-arcade downflows resulting from patchy reconnection. Discrete flux tubes are created, which then individually shrink, dipolarizing to form the post-eruption arcade. The measured quantities shown are averages from the current data set.

2.6. Acknowledgments

This work was supported by NASA Grant NNG04GB76G. The authors wish to thank Drs. D. Longcope, M. Linton, and E. Priest for valuable discussions, and also to acknowledge the assistance of Mr. James Tolan and Ms. Letisha McLaughlin, participants in MSU's NSF-sponsored Research Experiences for Undergraduates (REU) program, NSF Award 0243923, during the summers of 2005 (JT), 2006 (LM), and 2007 (LM). The authors also acknowledge the comments of the anonymous reviewers.

RECONNECTION OUTFLOWS AND CURRENT SHEET OBSERVED WITH Hinode/XRT IN THE 2008 APRIL 9 “CARTWHEEL CME” FLARE

3.1. Introduction

While the details of flare dynamics are debatable, the general energy release mechanism is widely accepted to arise from magnetic reconnection. Direct evidence of reconnection, however, has been scarce and often questionable. In all models of reconnection, loops flowing both towards and away from the reconnection site are an inevitable theoretical consequence (Carmichael 1964 [2]; Sturrock 1968 [50]; Hirayama 1974 [11]; Kopp & Pneuman 1976 [19]). Observationally, though, these loops require very special circumstances in order to image since they are likely to be relatively devoid of emitting plasma and form high in the corona where they are viewed against a dark background. Supra-arcade downflows (SADs) have been observed in several flares and interpreted as the cross-sections of these shrinking loops as they retract through a bright fan (McKenzie & Hudson 1999 [30]; McKenzie 2000 [29]; McKenzie & Savage 2009 [31]). Cusped flares, like those predicted by the standard models, have been shown to have signatures of retracting loops (Forbes & Acton 1996 [7]; Reeves, Seaton, & Forbes 2008 [37]). Imaging individual loops retracting above the flaring site with high enough temporal and spatial resolution has proven to be a challenge due to observational limitations. In order to observe the downflows which occur above the post-eruption arcade, the flare must occur near the limb; and long image exposures, which inevitably saturate the flaring site and are therefore not desirable for most

flare observations, must be taken to provide proper contrast in the low signal to noise region above the arcade.

Coronal mass ejections (CMEs) are frequently observed to be associated with eruptive flares. Current sheets are expected to extend between the arcade region and the CME (Forbes & Acton 1996 [7]). While the current sheets themselves are probably too narrow to be fully resolved with current instrumentation, calculations have shown that conduction fronts lead to the formation of a sheath of hot plasma surrounding the current sheet that widens the observable structure (Reeves et al. 2010 [36]; Seaton & Forbes 2009 [43]; Yokoyama & Shibata 1998 [62]). Recent modeling has shown that this hot plasma sheath can be observed by a sensitive X-ray imager such as Hinode’s X-ray Telescope (XRT) (Reeves et al. 2010 [36]). Current sheet observations have been claimed and analyzed for several flares using EUV and white light coronagraphs (Ciaravella & Raymond 2008 [3]; Lin et al. 2007 [24]; Webb et al. 2003 [60]; Ciaravella et al. 2002 [4]; Ko et al. 2003 [18]). Because white-light coronagraphs measure polarization brightness, which is directly related to density, these measurements indicate that the density in the structures surrounding the current sheet is elevated compared with the background corona.

In the following sections, we describe the “Cartwheel CME” flare as seen by XRT and LASCO. We describe the XRT observations in detail, which include a candidate current sheet, shrinking loops, and flows, and then show correspondences between

XRT and LASCO flows. We also discuss a possible scenario for interpreting the observations based on magnetic modeling.

3.2. Observations

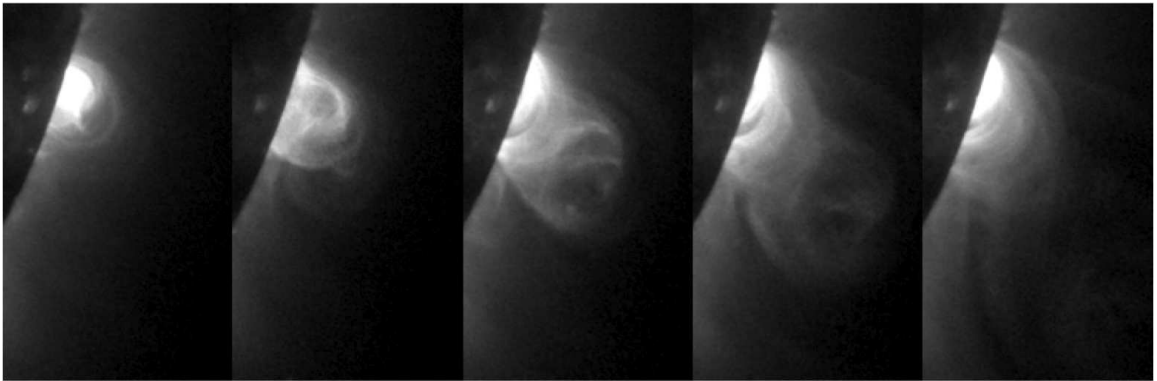


Figure 15: A CME is observed by XRT between 09:16 and 10:11 UT.

The stringent conditions required to observe faint structures associated with reconnection above a flaring region are all met during a flare observed by Hinode’s XRT on 2008 April 9 between 09:16 UT and 17:32 UT in association with active region 10989 (see Golub et al. 2007 [9] for a description of the XRT instrument). This flare has colloquially been nicknamed the “Cartwheel CME” flare because the observed structure, which we interpret as a flux rope in Section 4, appears to rotate as it is ejected from the Sun. The region is approximately 23° behind the west limb at the time of the eruption. Several instruments observed this event including XRT, *STEREO A*/SECCHI, TRACE, and LASCO. The flare is observed on the limb within SECCHI’s field of view (FOV) with *STEREO A* being 24.34° beyond the Earth-Sun

line. From the SECCHI observations, we place the actual flare start time at approximately 08:53 UT. This chapter will focus on observations from XRT and LASCO with support from SECCHI. XRT's images are taken using the Al/poly filter with 1 - 16 second exposures. There is no GOES signature for this flare due to its occurrence behind the limb; however, this fortunate observational situation offers a unique, relatively deep-exposure look at the supra-arcade region as the limb occulted the bright footpoints.

A large body of EUV- and X-ray-emitting mass is observed by XRT from 09:16 UT to 10:11 UT (Figure 15). The flare is obscured by the limb up to about 70 Mm in the XRT FOV. The speed of the structure as observed by XRT increases from ~ 80 to ~ 180 km s⁻¹. A white-light CME enters the *SOHO*/LASCO FOV at 11:06 UT and proceeds through the LASCO C2 FOV with an average speed of ~ 450 km s⁻¹ (Landi et al. 2010 [20]). The onset of the filament eruption is observed by SECCHI beginning at about 08:53 UT. Figure 16 (left) depicts the curved path of the eruption within the SECCHI FOV. Figure 16 (right) shows the CME as it passes through the LASCO C2 FOV. The dashed white line indicates the radial direction extending from the active region projected onto the plane of the sky. These observations indicate that the erupted structure initially moves in a non-radial direction toward the observer with its path becoming more radial as it approaches a height of $\sim 2.5 R_{\odot}$. The deflection may be the result of interaction with an open field region to the southeast of the active region, though such interaction remains speculative (Section 4). (See Landi et

al. (2010 [20]) for a detailed analysis of this CME.) The observations described in the following sections all occurred after the CME, and in the region from which it departed.

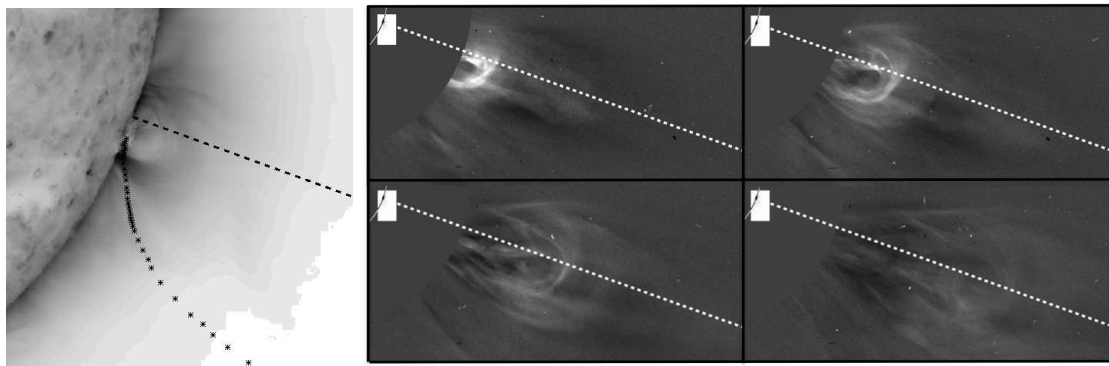


Figure 16: *Left*: Path of the erupted filament as seen by *STEREO A/SECCHI*. The dashed line indicates the radial direction extending from the active region as seen on the limb. The curved path follows the trajectory of the erupted structure from 08:53 UT (time of the reverse-scaled background image). *Right*: *LASCO C2* frames (11:06 UT, 11:26 UT, 11:50 UT, 12:26 UT) showing the CME path beyond $\sim 2.5 R_{\odot}$. The dashed line indicates the radial direction extending from the active region projected onto the plane of the sky. The XRT FOV is shown in the upper left-hand corner of each image.

3.3. Analysis

The original XRT images clearly show loops shrinking towards a bright arcade region. Sharpening the images improves the visibility of the individual loops at greater heights and makes it possible to detect faint, moving features previously unnoticed in the unsharpened movies.

The 358 original images examined between 08:01 and 17:32 UT are taken using an automatic exposure control setting. This resulted in some dynamic exposure times with a typical cadence of one minute. The median exposure setting is nearly 6 seconds which is about 60 times longer than exposure durations taken with the Al/poly filter of similar unocculted active regions on the verge of saturation (e.g. AR 10978; 2007 December 18). There is a large data gap of 155 minutes occurring between 13:47 and 16:22 UT. Despite normalizing, the widely varying exposure times make comparing successive images difficult due to the varying low signal-to-noise background level; therefore, the first step in sharpening is to eliminate the occurrence of non-repeating exposure durations within a time span of 30 minutes. The exposure-filtered set is flattened by dividing by the mean of an array of temporally-adjacent images with similar exposure durations. Then to enhance movement, each image is running-mean-differenced by subtracting the mean of the same set of similar surrounding images. Finally, the image set is byte-scaled in order to reduce any residual flickering (i.e. all of the pixels per image are binned based on a 0 to 255 intensity scale which reduces the dynamic scaling between images of different exposure lengths). The resulting image set has 274 images with typical cadences ranging from 1 to 5 minutes between data gaps (median: 1 minute).

3.3.1. Candidate Current Sheet

The sharpened image set reveals flows moving both towards and away from the solar surface (henceforth referred to in the text as downflows and upflows, respectively)

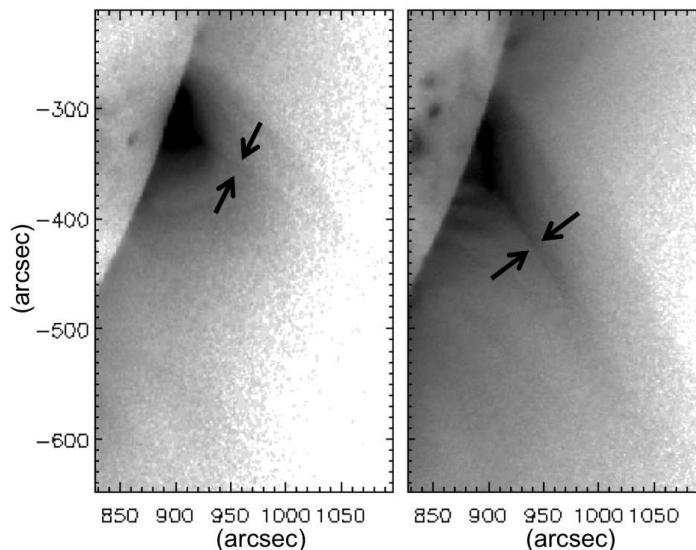


Figure 17: *Left:* (11:08:24 UT) *Right:* (17:31:55 UT) These reverse-scale images highlight the bright, thin linear feature (i.e. the candidate current sheet) extending from the apex of the arcade region from the 2008 April 9 event. Note the southward drift of approximately 4 deg/hr. All flows track along this feature even as it progresses southward.

and shrinking loops that can be tracked after the CME has left the XRT FOV. All of these flows both toward and away from the Sun, including the apexes of the shrinking loops, follow the direction of a bright, thin linear feature which extends from the apex of the arcade region. This feature becomes apparent at 11:00 UT following a nearly 40 minute data gap in the image sequence and slowly progresses southward about 25° over 6.5 hours for an average rate of approximately 4 deg/hr (see Figure 17). The solar rotation rate at a latitude of -18° , the approximate location of the flare, is about 0.6 deg/hr; therefore, the solar differential rotation cannot account for a projected drift of the linear feature.

The appearance of this feature is similar to those interpreted as current sheets by Ciaravella & Raymond (2008 [3]), Webb et al. (2003 [60]), and Ko et al. (2003 [18]). In particular, this feature is thin and bright compared to its surroundings and is located above the flare arcade. In all cases, coronal magnetic fields cannot be measured, so the inference of a current sheet is circumstantial; however, the position of this feature at the top of the arcade and its orientation between the arcade and CME are consistent with the interpretation of a current sheet. While the feature appears thin, the actual current sheet may be even thinner based on modeling which shows that current sheet structures can have surrounding areas of hot temperature due to conduction fronts, making the observable structure wider than the actual current sheet (Reeves et al. 2010 [36]; Seaton & Forbes 2009 [43]; Yokoyama & Shibata 1998 [62]). Recent modeling has shown that because of its sensitivity to high temperature plasma, XRT is able to observe this hot structure (Reeves et al. 2010 [36]). An additional piece of circumstantial evidence in favor of the current sheet interpretation is the motion of the observed shrinking loops. The shrinking loops observed in the XRT data display cusped looptops, and the apex of each loop tracks along this feature, consistent with the Kopp & Pneuman model (Kopp & Pneuman 1976 [19]).

This feature (henceforth referred to as the candidate current sheet or CCS) is initially detected at a position angle ~ 7 degrees southward of the CME when it first appears in the LASCO FOV at $\sim 2.5 R_{\odot}$ around 11 UT. It then immediately begins slowly drifting away from the LASCO CME path during its aforementioned apparent

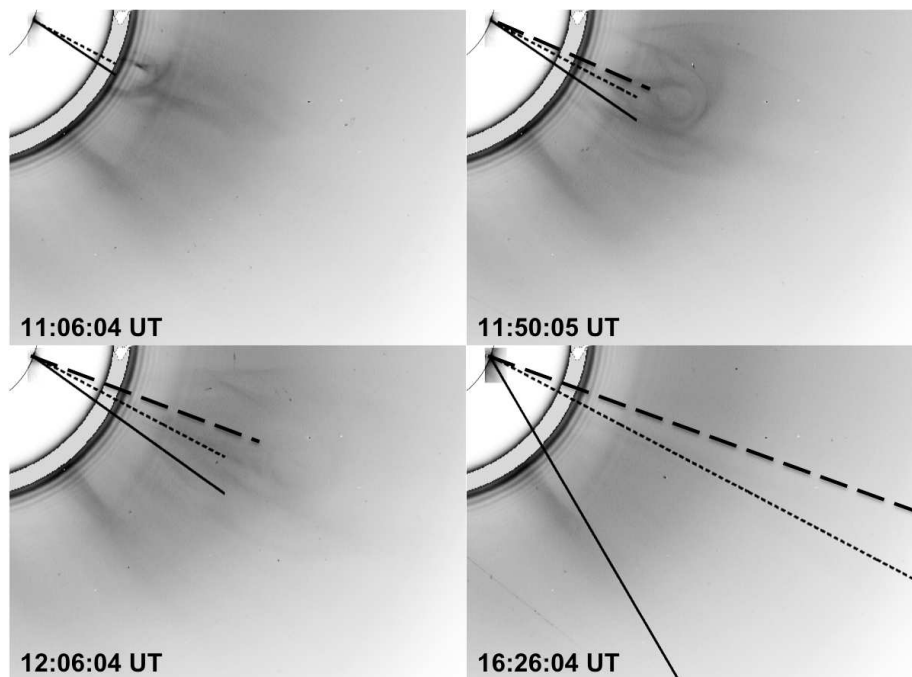


Figure 18: Reverse-scale composite images with an XRT inset overlaid onto corresponding LASCO C2 images. The candidate current sheet direction is represented by the solid line extending from the XRT arcade. The length of the line is extended to near the base of the CME in the LASCO images. The dotted line represents the initial direction of the CME as measured from the initial detection in the LASCO images (top left panel). The CME path direction as manually identified in each subsequent LASCO image is indicated by the dashed line. Notice that the CME does not follow a straight plane-of-sky path. The times indicated are those of the LASCO images.

southward progression. The alignment of the CCS with respect to the CME, and also the southward progression of the CCS, are consistent with the measurements from Webb et al. (2003 [60]) for 59 apparent current sheets showing an angular separation with the CME. Figure 18 displays reverse-scale composite images with an XRT inset overlaid onto corresponding LASCO C2 images. The direction of the CCS is first determined in the full-scale XRT images and then expanded into the LASCO C2 FOV to show the relationship between the CME path and the CCS direction. The

length of the displayed CCS roughly corresponds to the distance between the top of the arcade in the XRT images and the central base of the CME in the LASCO set. The initial CME direction (dotted lines) is displayed in all panels while the current CME location (dashed lines) is updated. The growing angle between the two directions shows that the CME does not follow a straight plane-of-sky path. This conclusion is also supported by the CME path as seen within the XRT FOV as well as by SECCHI images near the base of the flare (see Figure 16). The deflection occurs prior to $3 R_{\odot}$.

Examination of the source active region for this CME and flare indicates that the axis of the arcade is likely not oriented directly along the XRT line of sight due to the inclination of the polarity inversion line (see Section 4 for more details). Thus the proposed current sheet is not observed directly edge-on, but with some projection (as in Ko et al. 2003 [18] and Ciaravella & Raymond 2008 [3]). Such a projection would be consistent with the observation that near the midpoint of the XRT sequence, the CCS does not appear to be a single ray, but exhibits more of a fanlike structure (Figure 19 (a)). This structure is similar to those observed in the current sheet analyzed by Ko et al. 2003 [18] (see Figures 5 & 6 therein). Numerous other authors have noted such fanlike or “spikey” structures above arcades (e.g., Švestka et al. 1998 [53] and McKenzie & Hudson 1999 [30]). An example of this structure as seen in a flare occurring near the East limb on July 23, 2002 is given in Figure 19 (b). The

orientation of this flare is mirror opposite to that of the “Cartwheel CME” flare but with a less-severe projection angle.

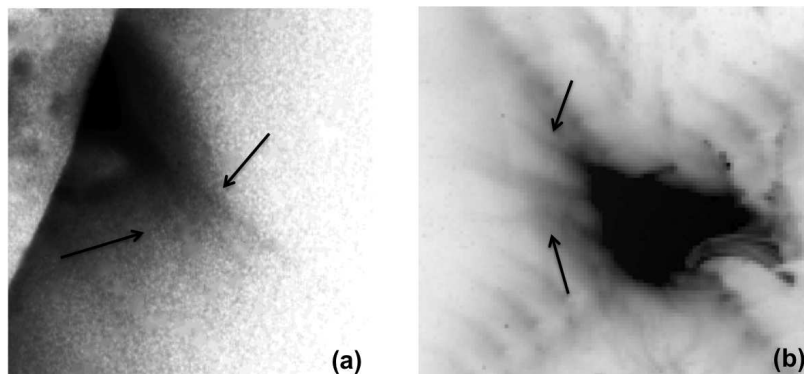


Figure 19: (a) (13:09 UT) Reverse-scale XRT image highlighting the fan-like appearance of the candidate current sheet near the midpoint of the XRT image sequence. This suggests that the CCS is not being viewed completely edge-on. (b) Reverse-scale TRACE image from July 23, 2002 at 00:40 UT. The orientation of this flare is nearly mirrored to that of the “Cartwheel CME” flare but with a less-severe projection. A fan above the post-eruption arcade loops similar to that seen in (a) is easily discernible.

The average thickness of the CCS (or rather the hot plasma surrounding the actual current sheet) is determined to be on order of $(4-5) \times 10^3$ km, depending on the image time. This thickness is measured by extracting slits across the current sheet feature and using the slit intensity profile as a guide for determining the CCS thickness (see Figure 20 for an example slice and profile). The selected images and the slits used to determine average thicknesses are displayed in Figure 21. These thickness values should be regarded as upper limit values as they represent a thickness that is not being viewed perfectly edge-on (see Figure 19).

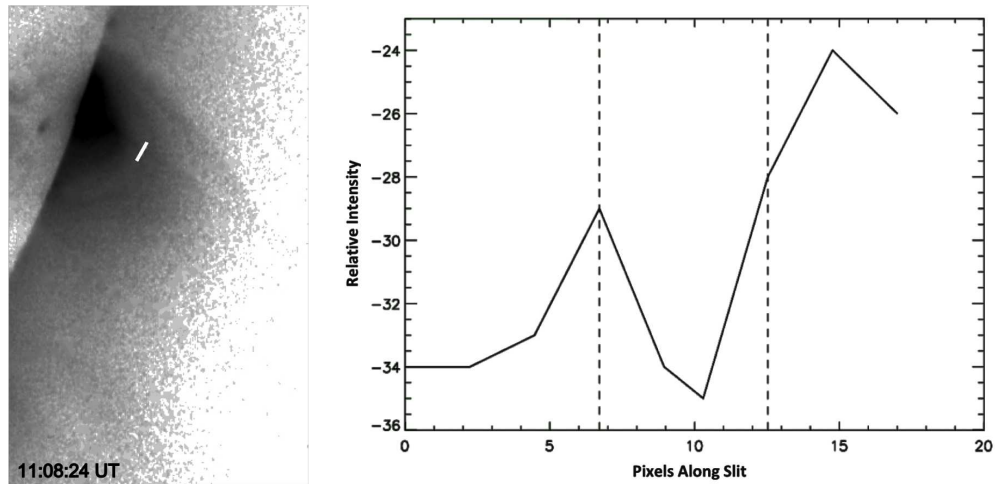


Figure 20: *Left*: Example slice (white line) across the CCS for determining its thickness. *Right*: The intensity profile across the slit. The vertical dashed lines correspond to the positions chosen as the edges of the CCS. Note that the scales of the image and the profile have been reversed.

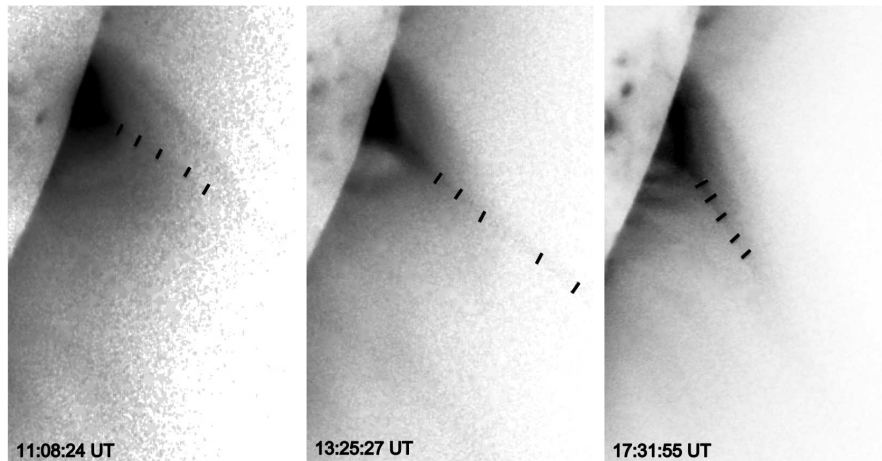


Figure 21: Reverse-scaled images selected for determining the CCS thickness. The slices across the CCS indicate the thickness determined for that position.

Ciaravella & Raymond (2008 [3]) obtained a CS thickness range of $30\text{-}60 \times 10^3$ km for the 2003 November 4 flare using UVCS and geometrical arguments. They claim that the broadened line profiles obtained from UVCS measurements “must result from either bulk flows or turbulence.” Furthermore, they predict the thickness due to turbulence to be $\leq 4 \times 10^3$ km. The similarity between this prediction and the measurements obtained with XRT for the “Cartwheel CME” flare suggest that turbulence may play a role in broadening the CS thickness.

Thickness estimates have been made by various authors for several other current sheets with similar orientations. Our thickness estimate of $(4\text{-}5) \times 10^3$ km is at least 10 times narrower than the estimate range of $(30\text{-}100) \times 10^3$ km measured by Ciaravella & Raymond (2008 [3]), Lin et al. (2007 [24]), Webb et al. (2003 [60]), Ciaravella et al. (2002 [4]), and Ko et al. (2003 [18]). The discrepancy in thickness values may arise from the fact that we observe very hot plasma with XRT’s Al/poly filter (temperatures from ~ 1 to at least 10 MK) using much finer resolution (~ 1 arcsec/pixel) than is observed with the various instruments used by these authors (i.e. LASCO (temperature-insensitive white light; C2: ~ 11.4 arcsec/pix), EIT ($\sim 0.6\text{-}3$ MK; ~ 2.6 arcsec/pix), UVCS ($\sim 2\text{-}8$ MK; $> \sim 40$ arcsec/bin for high temperatures)).

Because both XRT and LASCO observed this event, it is also possible to measure the length of the CCS assuming that the hot CCS observed in the XRT images corresponds to the white-light features in the LASCO images. Figure 22 depicts the progression of the CME height. The full length of the CCS is displayed as the

solid dark line in the LASCO FOV. An enlarged XRT FOV is inset for each LASCO image to show the position of the CCS just above the XRT arcade. The white boxes represent the error manually assigned to each position. The center of the boxes in the XRT images corresponds to the “p” value as described in Lin & Forbes (2000 [22]) and Webb et al. (2003 [60]) as the bottom position of the current sheet where it meets the top of the arcade. Conversely, the LASCO box indicates the “q” value which is the top position of the current sheet where it meets the bottom of the CME. (See Figure 32 for a visual reference.) These positions, determined “by eye”, have been de-projected based upon the footpoint used to de-project the flows (see Figure 25). It is important to note that these current sheet lengths are assumed to be the distance between these “p” and “q” values rather than direct length measurements of a confirmed current sheet; therefore, these reported lengths are upper bounds.

The results of the CCS length measurements are shown in Figure 23. There is strong qualitative agreement with the predictions from the Lin & Forbes (2000 [22]) reconnection model wherein the current sheet length (“q-p”) increases nearly linearly after reconnection begins and the top of the arcade increases comparatively little with respect to the CME height. A useful composite plot for comparing Figure 23 with the Lin & Forbes [22] height versus time predictions is given by Webb et al. (2003 [60]) (see Figure 9 therein).

The CCS length measurements correspond to an average thickness (as measured within the XRT FOV) of ~ 4.5 Mm (i.e. the CCS thickness remains fairly constant throughout the lifetime of the flare). The de-projected length measured at the time of the first and last CME detections in the LASCO C2 FOV is ~ 710 and 1950 Mm, respectively. The Alfvén Mach number can be calculated as $M_A = \text{thickness} / (q - p)$ resulting in estimates of $0.006 - 0.002$ (in order of LASCO C2 CME detection). These values are lower than previous estimates for other flares of greater than 0.1 (Ciaravella & Raymond 2008 [3]; Lin et al. 2005 [23]; Webb et al. 2003 [60]; Ciaravella et al. 2002 [4]; Ko et al. 2003 [18]) and approach the predicted value by Lin & Forbes (2000 [22]) requiring an M_A of at least 0.005 to produce an eruption. This prediction, however, applies to high-speed CMEs ($> 1000 \text{ km s}^{-1}$). The average speed of the 2008 April 9 CME within the LASCO C2 FOV is only about 450 km s^{-1} (Landi et al. 2010 [20]); therefore, the Mach number requirements for this model of reconnection may be relaxed. The Mach number predictions also vary greatly depending on the model's inclusion of 3-D geometry.

3.3.2. Shrinking Loops & Flows

Following the CME and beginning at approximately 11 UT, several individual, dark shrinking loops can be seen retracting just above the arcade. Bright regions can be seen flowing into the apex of the arcade beginning at 12:54 UT. (Dark and bright loops retracting just above the arcade are also clearly observed by SECCHI in the 171\AA and 284\AA bandpasses.) These bright regions are broader than the dark

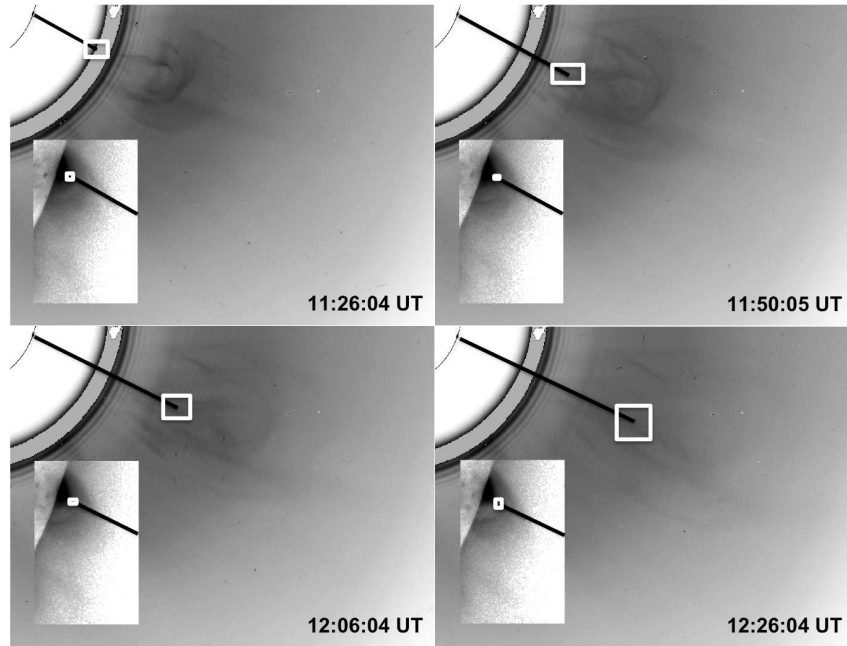


Figure 22: Reverse-scale composite images with an enlarged XRT inset overlaid onto corresponding LASCO C2 images. The length of the candidate current sheet is represented by the full solid line within the LASCO FOV. The “p” and “q” values correspond to the center of the white error boxes in the XRT and LASCO images, respectively. The times indicated are those of the LASCO images. The corresponding times for the inset XRT images differ by less than one minute.

shrinking loops seen earlier and are more difficult to distinguish as individual loops.

Loop structure associated with these regions is still maintained, however, in some of the images through which they track. Sharpening the data also reveals flows moving outwards from the flaring region. A three-pixel wide extraction is taken from each image along the CCS to create the stackplot image shown in Figure 24. The dark and bright lanes in the stackplot are due to the motion of the loops and flows along the CCS. (Hereafter, the apexes of the shrinking loops will also be referred to as downflows.)

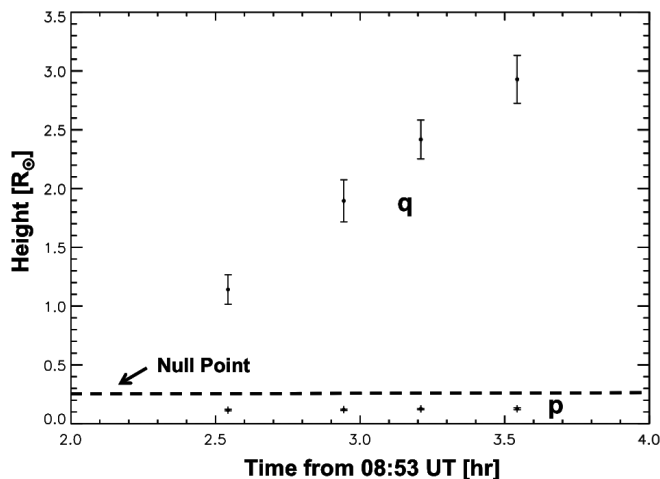


Figure 23: De-projected “q” and “p” heights in solar radii versus the time elapsed since the loss of equilibrium as seen in the *STEREO A*/SECCHI data (approximately 08:53 UT). (Refer to Figure 32 for a qualitative reference of the “q” and “p” positions.) This plot qualitatively agrees with predictions from the Lin & Forbes (2000 [22]) reconnection model wherein the distance between “q” and “p” increases steadily. (See Figure 9 from Webb et al. (2003 [60]) for a comparative graph.) The dashed horizontal line indicates the height of the null point ($0.25 R_{\odot} \sim 170$ Mm above the surface) which is discussed in Section 4.

A particularly intriguing flow set occurs between 12:18 UT and 12:35 UT and is labeled as the “Disconnection Event” in Figure 24. A bright region appears, moves slightly towards the arcade, and then disassociates. Part of the region flows towards the arcade while the other flows in the opposite direction away from the arcade along the CCS. To our knowledge, a possible reconnection outflow pair episode such as this (i.e. appearing in a region where retracting loops and upflows have been observed and along a directly observable SXR current sheet) has not been observed this close to the solar surface (at nearly 190 Mm). Outflow pairs much higher in the corona have been previously observed primarily with LASCO (see for example Sheeley & Wang

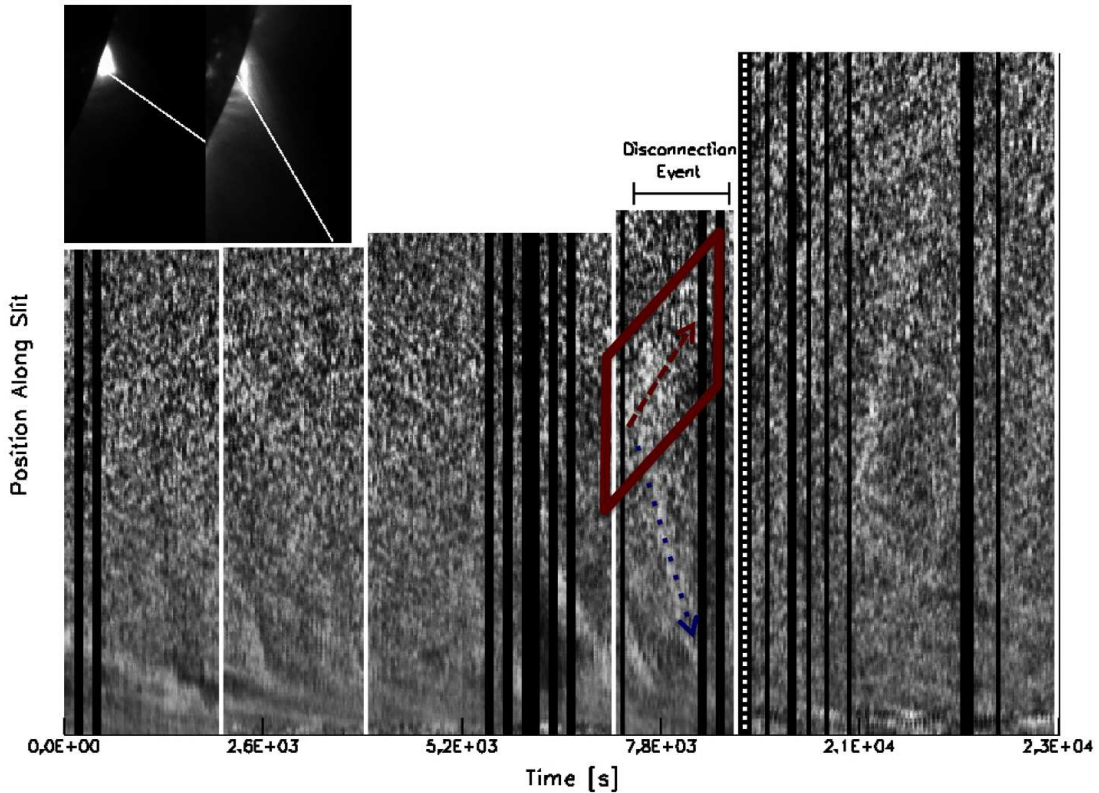


Figure 24: Position versus time stackplot created with three-pixel wide slits taken along the current sheet candidate as it progressed southward within the XRT FOV. Representative slits are displayed as insets in the top-lefthand corner. Each three-pixel segment represents approximately one minute. Dark and bright lanes indicate motion along the extractions. The black vertical strips are due to small data gaps, and the dashed vertical strip represents the large data gap beginning at 16:25 UT. The separate panels indicate that a different slit was used for that time frame to allow for the southward progression. The disassociation position of the reconnection outflow pair is indicated in the figure. The upflow portion of the disconnection event is much more diffuse than its downflow counterpart, making it appear broader and dimmer.

2007 [45], Lin et al. 2005 [23], and Sheeley, Warren, & Wang 2004 [46]). Possibly related features have been observed with RHESSI (e.g. Liu et al. 2008 [26]; Sui, Holman, & Dennis 2004 [52]; Sui & Holman 2003 [51]) and various other instruments

ranging from H-alpha to SXR detectors along with white-light coronagraphs (e.g. Tripathi et al. 2007 [56]; Tripathi, Isobe, & Mason 2006a [55]), though the interpretations may differ. The large data gap unfortunately occurs immediately following this event hindering possible observations of continued reconnection occurring in the region.

Previous work done by the authors has focused on automatically tracking and characterizing supra-arcade downflows (SADs) during long duration flaring events (McKenzie & Savage 2009 [31], see also previous Chapter). Automatically tracking shrinking loops for this event presents several challenges primarily due to the low signal to noise ratio complicated by the southward progression of the CCS. Therefore, the flows from this flare are tracked manually to ensure reliability.

A total of sixteen flows are tracked (13 downflows and 3 upflows) over a total time of 6.22 hours between 11:11 and 17:24 UT. The number of frames through which each flow is observed ranges from 3 to 22 with a median frame count of 10. Figure 25 (a) shows the plane-of-sky trajectories of the manually-tracked flows. Note that the magenta flow in the southwest region represents the track of a very faint, diffuse upflow that occurred after the large data gap. Despite its discrepant path compared to the other flows, it still tracks along the CCS which had progressed southward by the time of this flow.

We use a Potential Field Source Surface (PFSS, Schatten et al. 1969 [41]; Schrijver & DeRosa 2003 [42]) model to extrapolate the magnetic field from active region 10989.

The magnetic field morphology suggests that the footpoints of the shrinking loops lie near a latitude of -18° and a longitude of 23° beyond the west limb. This footpoint is used as a point of convergence for all of the flows in order to de-project their positions above the solar surface. The flows are assumed to have no velocity component in the longitudinal direction. The positions have also been rotated based on the latitude of the footpoint. The resulting de-projected trajectories are shown in Figure 25 (b) and (c) overlaid onto reverse-scaled MDI magnetograms with magnetic loops traced out from the PFSS modeling. We emphasize that 2-D motion is measured from the images, in plane of the sky. The uncertainty in the 3-D trajectory is entirely due to assumed longitude.

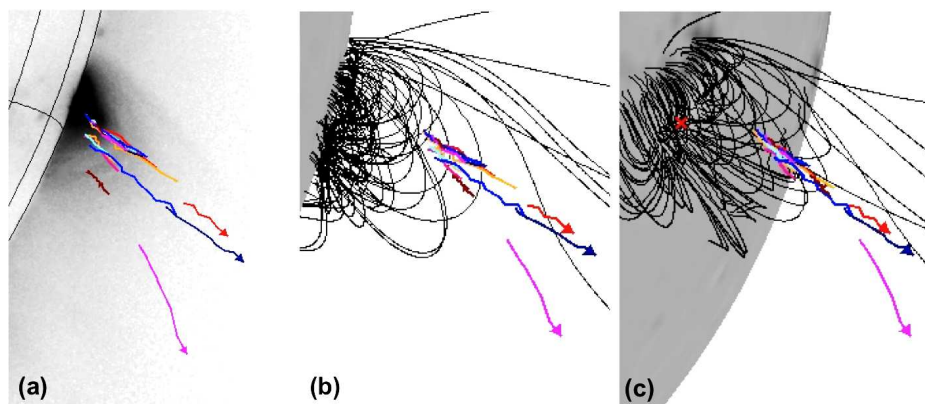


Figure 25: (a) Plane-of-sky trajectories of the manually-tracked flows overlaid onto a reverse-scaled XRT image taken at 16:30:54 UT. (b) & (c) De-projected trajectories based on a convergent footpoint at a latitude of -18° and a longitude of 23° beyond the west limb. The reverse-scaled background images (MDI magnetogram plus magnetic loops) are derived from a PFSS model package (Schrijver & DeRosa 2003 [42]) with a center longitude set to (b) 115° and (c) 150° . The flows are assumed to have no velocity component in the longitudinal direction. The arrows represent upflow trajectories.

Figure 26 shows de-projected height-time profiles for (a) a typical downflow and (b) a typical upflow observed in this study. The positions are given with respect to the chosen footpoint on the solar surface. The error bars displayed for the position represent the square root of the size of the flow at that position. These extents are determined manually and are chosen conservatively; however, errors associated with footpoint assignment and tilt in the longitudinal direction are not included in the error estimate. The initial velocity and acceleration uncertainties are determined by adding these position errors to the 2-D polynomial fit. This fit is represented by the solid profile line in Figure 26. The gravitational profile for a body in free-fall given the initial height and velocity of the flow is shown as the thick dashed line. The left panel includes a thin dashed profile line outlining the trajectory of a body falling while experiencing a constant drag force. (See Chapter 4 for more information.)

All of the downflow speeds are slower than their corresponding free-fall speeds especially as they near the limb, except for one flow that is only tracked through three frames. Faster downflow speeds would have supported the reconnection outflow hypothesis; however, it is not excluded by this opposite result either considering that other flow characteristics provide significant support. Namely, several of the flows exhibit a clearly-defined cusped or rounded loop structure and one of the regions is observed to disconnect into an upflow and a downflow which are expected results from reconnection. Also, the flow profiles diverge the most from the gravitational profiles as they near the limb and, presumably, the top of the arcade where the

loops are expected to settle to a potential configuration. If these flows are indeed reconnection outflows, then this result may indicate that a source of drag (e.g. mass build up in front of the flows due to density in the current sheet, shocks, magnetic field entanglement, etc.) has a significant effect on the flow speeds. Additionally, these profiles are qualitatively supported by reconnection models. Lin (2004 [21]) (Figure 5 therein) has shown that the retracting reconnected loops shrink primarily within the first 10-20 minutes and then decelerate considerably which is consistent with the profiles shown in Figure 27.

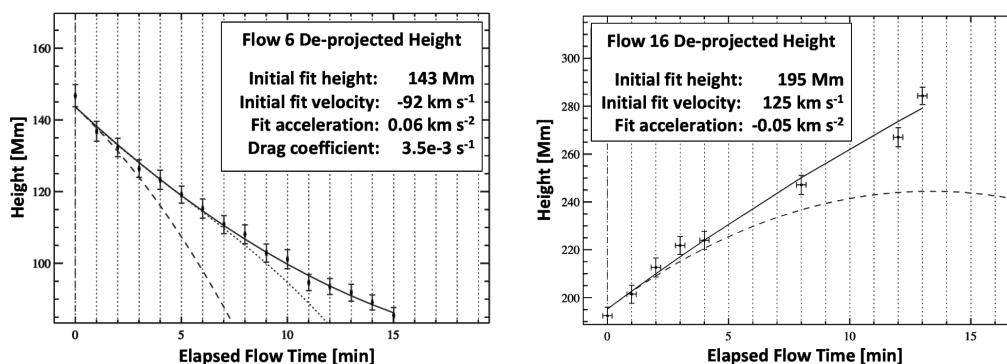


Figure 26: De-projected height-time profiles represented by (a) a typical downflow and (b) a typical upflow observed in this study. The vertical dotted lines mark the mid-exposure time of each image in the sequence. (Note that Flow 16 does not have a contiguously-detected track due to the low signal-to-noise ratio at the heights through which it travels.) The solid line is the 2-D polynomial fit applied to the profile to obtain the initial velocity and acceleration. The calculated fit parameters are given in the legend for each flow. The thick dashed line represents the gravitational profile for a body in free-fall given the initial height and velocity of the flow. The thin dashed profile line in (a) represents the gravitational profile for a body in free-fall experiencing a constant drag coefficient of $3.5 \times 10^{-3} \text{ s}^{-1}$.

The time for each position shown in Figure 26 is taken as the frame start time plus half of the exposure duration; thus, the time error bars, too small to be visible on the plots, represent half of the exposure duration which ranges from 2 to 16 seconds. The vertical dotted lines mark the time of each image (start time plus half of the exposure duration) in the sequence. Note that due to a low signal to noise ratio high above the arcade, the flows are not always detected in contiguous frames. The gaps in the profile in Figure 26 (b) (i.e. vertical dashed lines without a flow position marked) graphically represent this discontinuity. A 2-D polynomial fit (solid line) is applied to each profile to obtain initial velocities and accelerations. All of the profiles are plotted together in Figure 27.

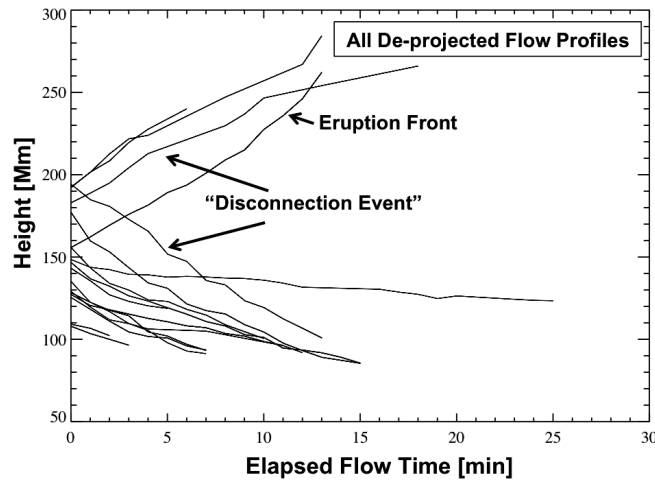


Figure 27: All de-projected height-time profiles. Profiles with a positive slope represent upflows. The eruption front and disconnection event profiles are labeled in the figure. Note that the initial heights of the upflow and downflow portions of the disconnection event are separated slightly because the region appears to brighten and move sunward prior to separating.

Because expected quantitative predictions can vary largely within reconnection models depending on conditions and constraints, a qualitative way of distinguishing between the Sweet-Parker and Petschek models is through the profiles of the flow trajectories. Sweet-Parker predicts a sustained acceleration all along the current sheet with the Alfvén speed being reached only near the tips of the sheet. The Petschek model predicts acceleration in a small diffusion region near the reconnection point with the flow’s final velocity (nominally the Alfvén speed) being reached within a relatively short distance near the reconnection point and then maintained until it exits the current layer (including slow shocks). The measured flow profiles exhibit accelerations very near to 0 km s^{-2} , except for some slowing as the downflows approach the post-eruption arcade, which matches well with the Petschek predictions (Somov 1992 [49]).

The de-projected speeds vary from the plane-of-sky speeds by up to 11% but with a mean difference of only 7%. The initial de-projected speeds range from 21 to 165 km s^{-1} (median: 120; mean: 109). The slowest speed is attributed to the last shrinking loop occurring after the large data gap. See Figure 28 (a) for a histogram of these velocities. Upflows have been assigned a positive value. The distribution from this small sample does not yield a recognizable trend; however, all speeds are much smaller than the predicted value near the Alfvén speed which is typically assumed to be a value on order of 1000 km s^{-1} for the corona. We are unable to directly measure the coronal magnetic field and thus, the Alfvén speed.

The de-projected acceleration distribution is displayed in Figure 28 (b). The acceleration magnitudes range from 0.01 to 0.6 km s^{-2} (median: 0.1; mean: 0.2). All flows are either slowing down slightly or have average accelerations consistent with zero.

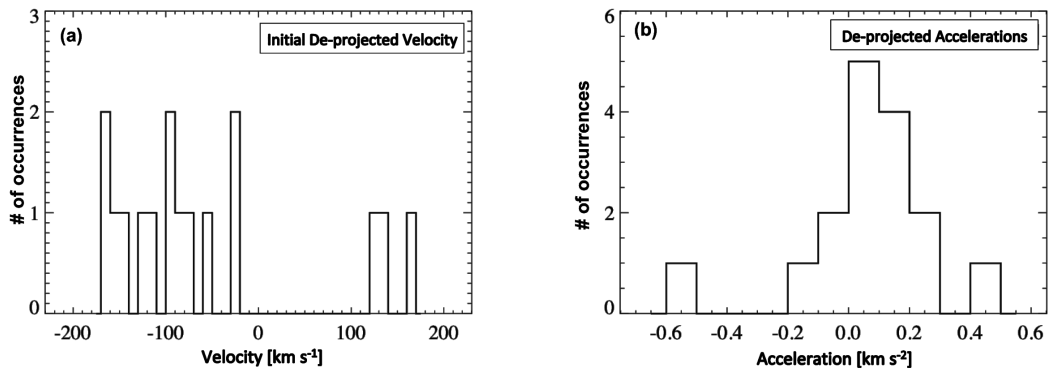


Figure 28: (a) Histogram of the initial de-projected velocities. Upflow velocities are positive. (b) Histogram of the de-projected accelerations. All flows are slowing down or have accelerations consistent with zero.

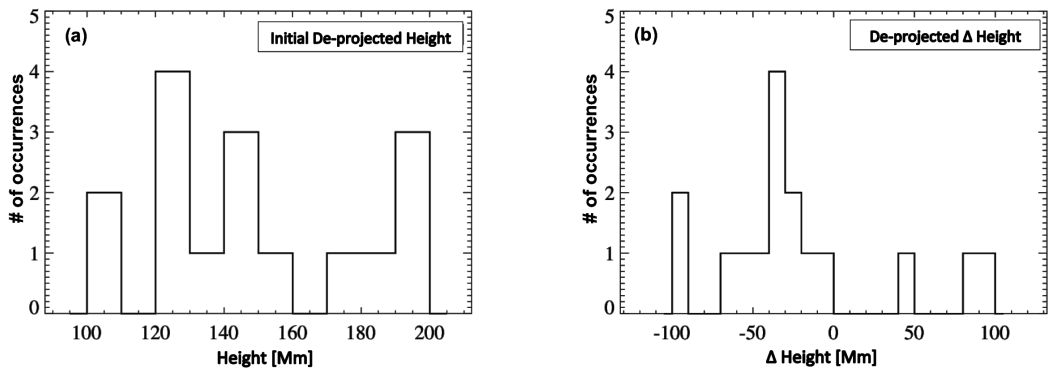


Figure 29: (a) Histogram of the initial de-projected heights. (b) Histogram of the de-projected change in heights.

The initial de-projected heights above the footpoint, which vary from the plane-of-sky heights by up to 10%, are displayed in Figure 29 (a). The heights range from 108 to 194 Mm (median: 145; mean: 150). The overall change in de-projected height (i.e. “distance travelled”) of the flows is shown in Figure 29 (b). These values range from 7 to 106 Mm (median: 40; mean: 48). Previously-measured downflow estimates for similar limb flares have upper limits of about 130 Mm on height and about 40 Mm on the shrinkage distance (McKenzie & Savage 2009 [31]). The increase in these height measurements for the “Cartwheel CME” flare can be attributed to the footpoints being occulted (as discussed in Section 3.2).

3.3.3. XRT & LASCO Upflows

Further inquiry was performed to determine how the upflows tracked beyond the XRT FOV. The upflows are detected in the noisiest regime of the images high above the flare arcade and are therefore the most difficult to accurately track. Combining these relatively high-error position estimates with fewer detected positions due to their location towards the edge of the FOV adds a large uncertainty to extrapolating their trajectories beyond the XRT FOV.

Despite these difficulties, extrapolating the upflow positions simply using their average speeds revealed some possible associations with flows observed in LASCO. In an attempt to incorporate a more accurate profile for the XRT upflows into the outer corona, the corresponding LASCO flows are tracked and an acceleration is determined from their height-time profiles. Those accelerations are determined to be 0.025, 0.02,

and 0 km s^{-2} respectively. (The path of the third LASCO flow is difficult to track and yielded inconsistent results; therefore, an acceleration of 0 km s^{-2} is applied.)

The XRT upflow positions are extrapolated to the outer corona by using their final fit velocity in the XRT FOV as an initial velocity beyond the XRT FOV. The corresponding LASCO flow accelerations are then applied to determine successive flow positions. (The XRT FOV accelerations determined from a 2-D polynomial fit are slightly negative due to the unreliability in the final position measurement of the flows. The initial extrapolations were made by using the final fit velocity with zero acceleration resulting in decent agreement between the XRT and LASCO flows. Applying the LASCO accelerations, which are listed above and do not vary significantly from 0 km s^{-2} , results in slightly better agreement.) The XRT upflow paths are assumed to be straight although the CME path itself initially veers northward (see Figure 16). This results in the upflows tracking just to the south of the LASCO flows. As a check on this procedure, the eruption front position, which is expected to be observed in LASCO as a white-light CME, is extrapolated in the same manner using a measured acceleration of 0.03 km s^{-2} . Allowing for some angular separation due to the aforementioned CME path deflection, the resulting extrapolated positions correspond precisely to the CME front in the LASCO FOV (Figure 30, top panel).

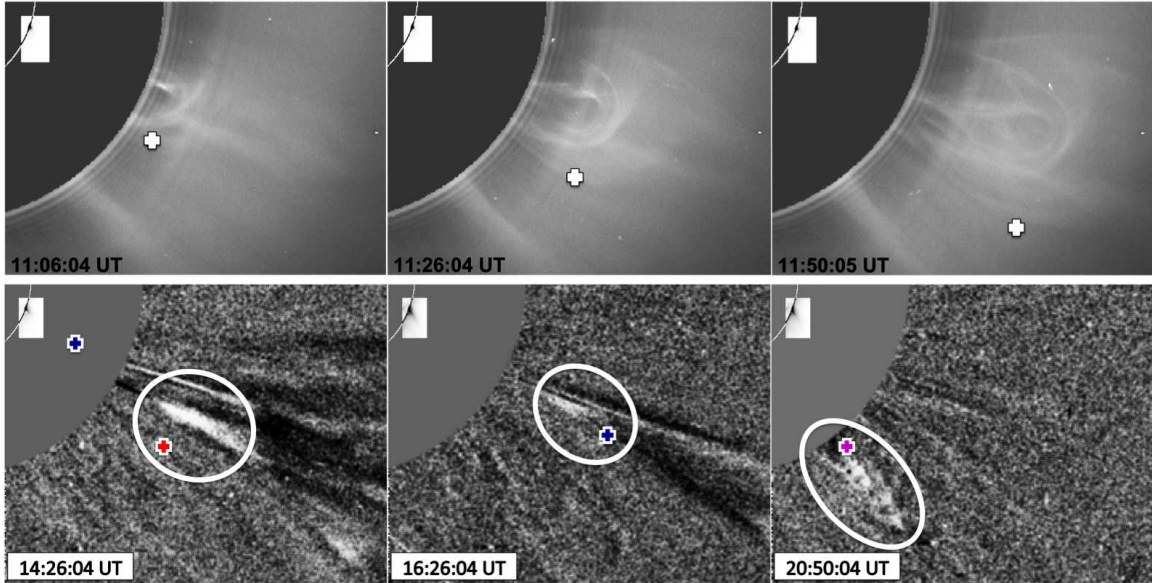


Figure 30: XRT & LASCO flow associations: All panels consist of composite XRT (reverse-scaled)/LASCO C2 images. *Top Panel:* The white crosses correspond to the extrapolated position of the XRT eruption front which tracks precisely with the white-light CME seen in the LASCO images. The acceleration of the LASCO CME is factored into the extrapolations; however, deflection is not included (see Figure 16). *Bottom Panel:* The LASCO images are running-mean-differenced and enhanced to emphasize flows. The colored crosses correspond to the extrapolated positions of the XRT upflows. Ellipses indicate strong XRT/LASCO flow associations after using the LASCO flow accelerations to extrapolate the XRT upflow positions. Note that the colors in this figure correspond to the colors of the tracks in Figure 25.

This minimally-biased method results in strikingly close associations between the XRT and LASCO upflows (Figure 30, bottom panel). In addition, the upflow resulting from the XRT disconnection event appears to closely correspond with the concave upward feature following the CME (i.e. the CME “pinch-off point”) which in turn corresponds to the CME disconnection event described by Webb et al. (2003 [60]).

3.4. Discussion

Some standard eruptive flare models consist of a flux rope which is released as a coronal mass ejection, generally due to some reconnection occurring near the active region. The flux rope eruption is followed by the formation of a current sheet between the CME and the growing underlying arcade along the polarity inversion line. The arcade is formed when magnetic loops reconnect high in the current sheet and then retract to a less energetic configuration.

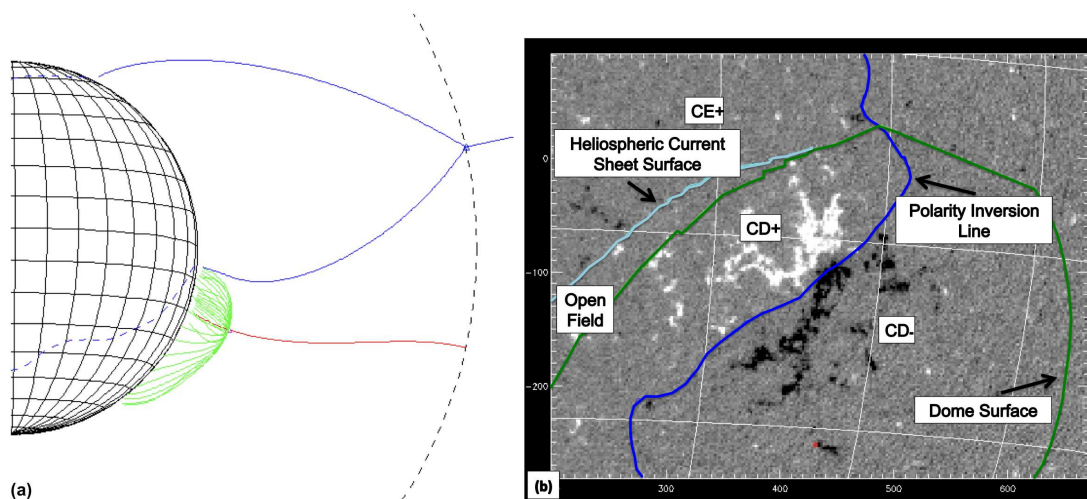


Figure 31: (a) PFSS model of the active region as it crossed the limb ($\sim 08:00$ UT on 2008 April 7) using a source surface at 2.5 solar radii (black dashed circle). *Blue*: Heliospheric current sheet and its separatrix (dashed). *Red*: Spine lines extending from the null point ($r = 1.25 R_{\odot}$) (where the spine line and dome (green) intersect). *Green*: Dome fan surface originating from the null point which encloses all of the closed field originating from the active region's negative polarity. (b) Magnetogram taken a week before the flare. CE+ is the region of positive field that closes across the equator to negative flux in the northern hemisphere. CD+/- are the regions of positive/negative field enclosed by the dome described above. The "Open Field" region extends to the southeast of the active region.

The “Cartwheel CME” flare follows this general interpretation; however, investigating the 3-D nature of this flare is important in order to understand the subtle variations from the 2-D model, namely the apparent southward progression of the CCS. First, we invoke a PFSS model to get a general understanding of the active region’s magnetic topology. The macroscopic field is approximated using a PFSS model from the harmonic coefficients distributed by the Wilcox Solar Observatory. The skeleton of this field is shown in Figure 31 (a) for the active region as it crossed the limb (2 days prior to the flare). Open field crosses the source surface, located at 2.5 solar radii (black dashed circle), in regions of outward and inward flux separated by the heliospheric current sheet (HCS) mapping down to the solar surface in helmet-shaped separatrices (blue). The flux below this surface is composed of closed field lines. In addition there is a single coronal null point located about 170 Mm ($r = 1.25 R_{\odot}$) above the active region. The fan surface of this negative null point forms a dome (green lines) overlying all the closed field lines anchored in the negative polarity of AR 10989.

The photospheric image of the large-scale skeleton is indicated in Figure 31 (b) on top of an MDI magnetogram from one week before the flare, when AR 10989 was visible on the disk. The image of the HCS separatrix (cyan) divides positive footpoints of the field lines which close across the equator (CE+) from open field lines. The footprint of the dome (green) encompasses the closed field of the AR which crosses the polarity inversion line (PIL, blue). The north-south orientation of

the PIL almost certainly persists until the time of the flare, suggesting that the CS is not seen edge-on.

Based on the magnetic field topology of the active region, a scenario for this flare’s evolution can be described as follows: An eruption occurred in the field originally under the dome. The field opened by the CME then temporarily joined the flux from the large-scale “Open Field” region which extends to the southeast of the active region. This conclusion is supported by SECCHI observations which show that the filament initially moves southeastward towards the “Open Field” (see Figure 16). Removal of closed flux would result in the dome shrinking downward with the left portion of the green curve in Figure 31 (b) likely moving to the right. The excess open flux resulting from this shift would not be energetically favorable; therefore, reconnection began to occur (likely in the right to left direction) to replenish the field lines in the CD region and to counteract the dome shrinkage. This reconnection is observed as shrinking loops. The SECCHI images strongly suggest that the shrinking of loops begins in the west and progresses southeastward along the PIL. The lifting of the dome to its initial configuration is observed as the rising of the post-eruption arcade. Examples of an arcade brightening from end-to-end, progressively along the length of the PIL, are not new. See, e.g., Hanaoka et al. (1994 [10]) and the more recent analysis by Tripathi et al. (2006b [57]) referring to them as “asymmetric eruptions.”

A schematic diagram for a 3-D interpretation of the “Cartwheel CME” flare is provided in Figure 32. A FOV closely matching that of XRT, rotated so as to focus on the current sheet extending from the arcade, is shown in (a). The outer corona (unrotated) is shown in (b) to describe the LASCO C2 images. A current sheet would form along the PIL and between the erupted flux rope and arcade. The current sheet “boundaries” could extend outward from the ends of the developing arcade. The anchored legs of the flux rope are observed by XRT to slowly rotate southward and are shown in Figure 33. A very similar scenario is depicted by Ciaravella & Raymond (2008 [3]) (see Figure 7 therein).

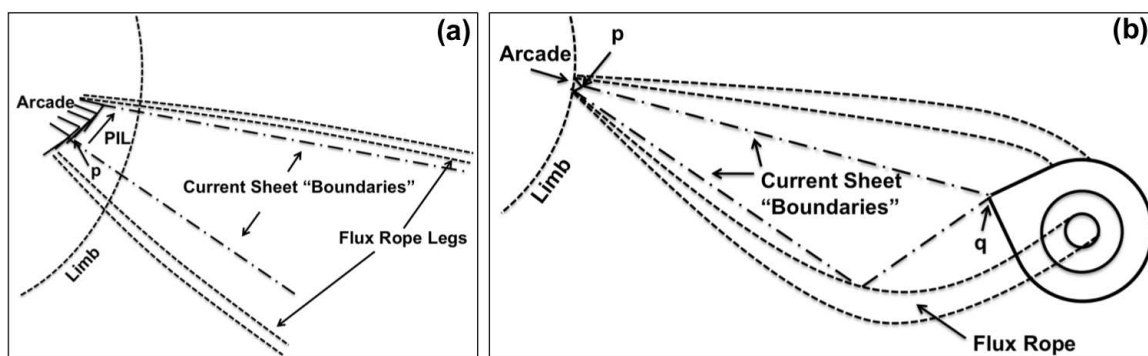


Figure 32: Schematic diagram depicting a 3-D interpretation of the “Cartwheel CME” flare as seen by (a) XRT (rotated view) and (b) LASCO. A current sheet would form along the polarity inversion line (PIL) and between the leading edge of the erupted flux rope and arcade. The boundaries of this current sheet could extend along the length of the arcade.

XRT observes high temperature plasma. The Al/poly filter is sensitive to plasma at several millions of degrees K. It is unlikely that the current sheet shown in Figure 32 would be emitting at such high temperatures except in regions of active reconnection.

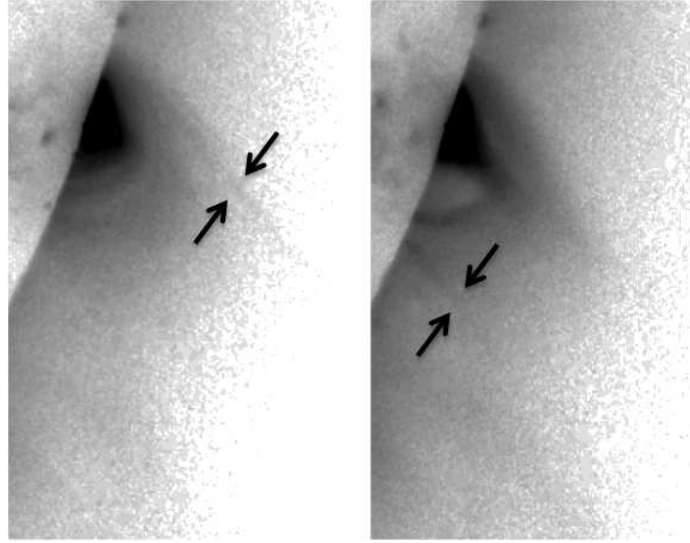


Figure 33: Anchored legs of the flux rope slowly rotate southward (plane-of-sky) through the XRT FOV.

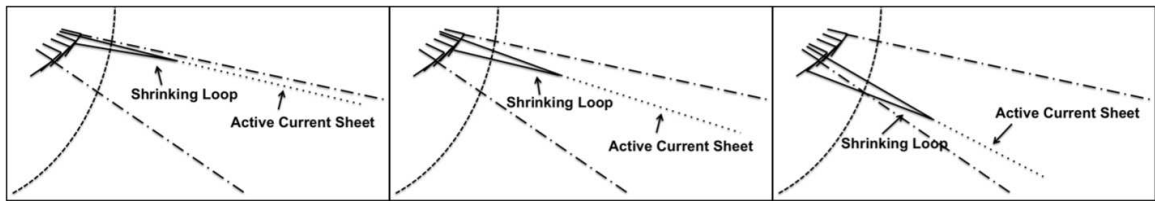


Figure 34: Evolution of the current sheet near the arcade closely matching a rotated XRT FOV. The shrinking loops begin in the west and move southeastward along the polarity inversion line. The active current sheet indicates where reconnection is occurring and would likely appear as a bright, thin linear feature in XRT images.

We noted above that the shrinking loops appear to begin in the western region and move southeastward along the inclined PIL. Figure 34 shows how the current sheet would look at different stages considering this southeast motion. If only the active portion of the current sheet (where reconnection is occurring) were to be emitting at high temperatures (Reeves et al. 2010 [36]), then a bright, thin linear feature would

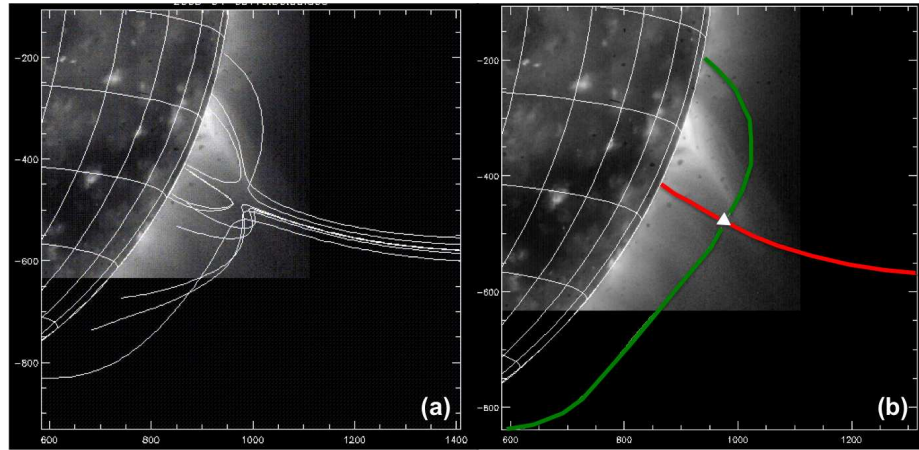


Figure 35: (a) Typical field in the neighborhood of the boundaries indicated by the colored lines in the right panel. (b) 2-D slices of the dome and spline lines (green and red, respectively) from the PFSS model shown in Figure 31 (a). The null point is indicated by a white triangle.

be observed by XRT and appear to move southward. This phenomenon is exactly what is observed; therefore, we propose that the current sheet is not being physically rotated. As noted in Section 3.1, near the middle of the XRT image sequence, the CCS appears fan-like (see Figure 19) which could indicate multiple regions of patchy reconnection. Also, the shrinking loops early in the image sequence appear to be dark while later they appear bright. We speculate that this may be due to an increased density available in the current sheet as the flare progresses through processes such as chromospheric evaporation.

2-D slices of the dome and spline lines are shown in Figure 35 with the null point symbolized by the white triangle in (b). In a 2-D model, a current sheet would be oriented along a bisector between the green and red curves in (b); however, the actual

field is not potential so the location of the current sheet would not exactly match this prediction. This null point is overlaid onto the track composite images in Figure 36.

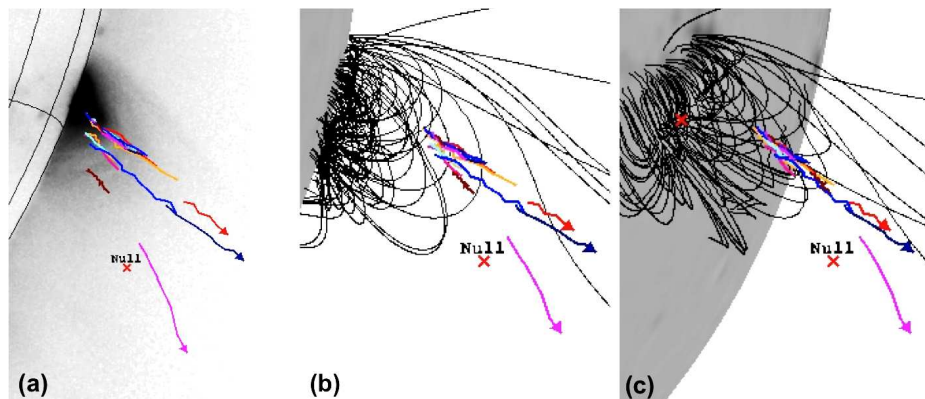


Figure 36: Track composite images from Figure 25 with the null point overlaid.

3.5. Summary & Conclusions

Downflowing oblong voids have been observed with SXT and TRACE above arcades resulting from long-duration flaring events. Similar flows have been observed on much larger scales with LASCO although not always in association with flare arcades (McKenzie & Hudson 1999 [30]; McKenzie 2000 [29]; McKenzie & Savage 2009 [31]; Asai et al. 2004 [1]; Khan et al. 2007 [17]; Sheeley, Warren, & Wang 2004 [46]). These features, known as supra-arcade downflows (SADs), have been interpreted as the cross-sections of individual shrinking magnetic loops as they retract from the reconnection site high above the arcade. The dark loops seen early in the image sequence are consistent with the “shrinking empty loop” discussion pertaining to SADs

in McKenzie (2000 [29]) and the spectral measurements of Innes et al. (2003a [14]). The brightening of the flows in the middle of the sequence (approximately 3 hours after the flux rope release) may have resulted from increased density in the current sheet as the flare progresses through processes such as chromospheric evaporation.

Figure 37, adapted from McKenzie & Savage (2009 [31]), gives quantitative estimates of pertinent parameters that describe this scenario based on a small sample size. The viewing angle for SADs with respect to Figure 37 (a) is from the side (i.e. nearly perpendicular to the arcade). If this scenario is correct, then for the 2008 April 9 event, the viewing angle is face-on to the loops (i.e. along the axis of the arcade) so as to observe supra-arcade downflowing loops (SADLs) as shown in Figure 37 (b). The perpendicular viewing angle is supported by the observation of shrinking loops in XRT and SECCHI as well as the magnetic field configuration derived with the PFSS modeling (see Figure 25 (b)). The available relevant information obtained for this event has been labeled in the figure.

This flare is fairly unusual in that it occurred behind the limb in XRT allowing for better image quality high above the arcade with support from STEREO A observations of the flare on the limb. Under these circumstances, a relatively faint, thin candidate current sheet (CCS) is observed in XRT and the height at which the flows are first detected is increased from that of the previously-analyzed SADs thereby increasing the overall length of the downflow path as well. The striking similarity

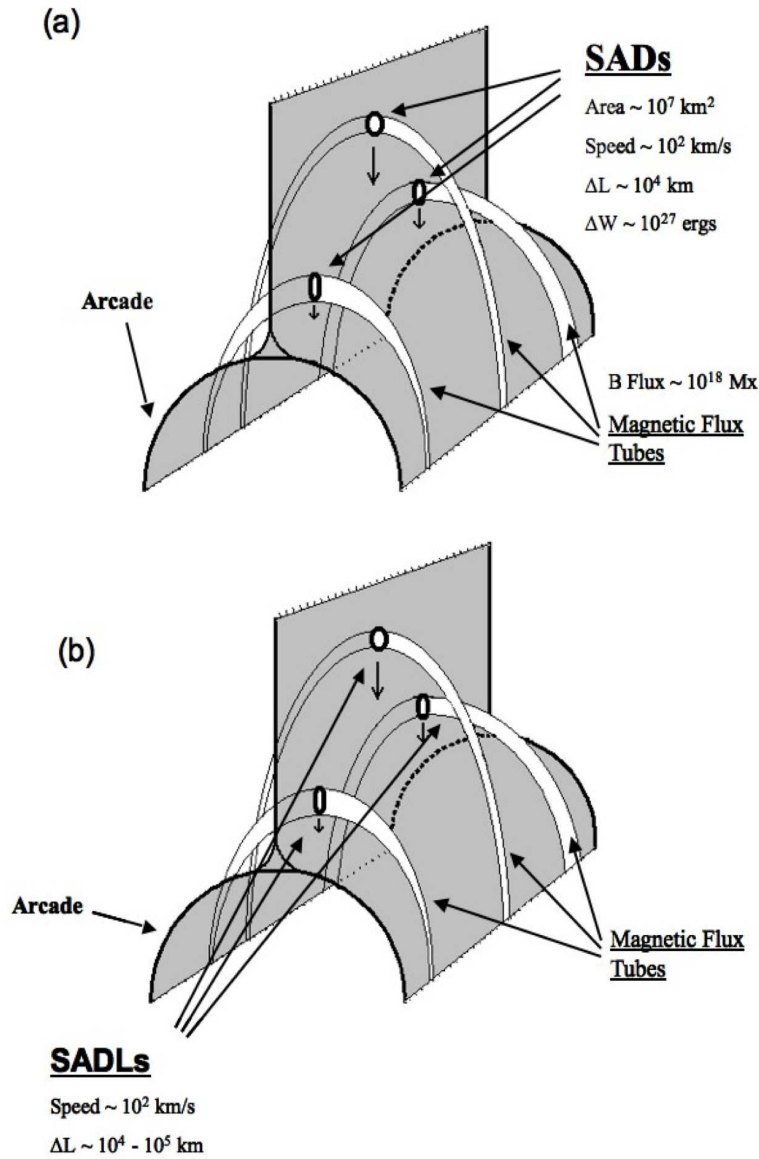


Figure 37: (a) Schematic diagram of supra-arcade downflows (SADs) resulting from 3-D patchy reconnection. Discrete flux tubes are created, which then individually shrink, dipolarizing to form the post-eruption arcade. The measured quantities shown are averages from the following events: 1999 January 20 (M5.2); 2000 July 12 (M1.5); 2002 April 21 (X1.5) (McKenzie & Savage 2009 [31]). (b) Schematic diagram of supra-arcade downflowing loops (SADLs) also resulting from 3-D patchy reconnection. The measured quantities are averages from the flare occurring behind the western limb on 2008 April 9. Note that the viewing angle is perpendicular to that of the SADs observations.

between the speeds and path lengths offers support to the argument that these two observational features are different views of the same phenomenon.

Additionally, we observe a disconnection event which we interpret as a reconnection outflow pair. We believe that this is the first clearly-observed reconnection outflow pair observed so near to the solar surface along a directly observable SXR current sheet. The relatively narrow initial height range (~ 100 Mm) with respect to the CCS extent (see Figure 23) combined with the reconnection outflow pair observations seems to imply patchy reconnection with a relatively localized acceleration region. The possible correspondence of upflows observed to propagate from within the XRT FOV into the LASCO FOV, notably the upflow associated with the LASCO CME “pinch-off point”, also support this statement.

Reports of impulsive-phase RHESSI double coronal sources have been made by other authors (e.g. Liu et al. 2008 [26]; Sui, Holman, & Dennis 2004 [52]; Sui & Holman 2003 [51]) with the lower source corresponding to the top of the rising arcade and the upper source possibly corresponding to an ascending reconnection outflow or an ejected plasmoid. We note that these upper coronal sources have paths, speeds, and placements relative to the arcade similar to the bright plasmoid structure tracked as the eruption front for the “Cartwheel CME” flare (Figure 2). This is consistent with the extrapolated position of one coronal source from the 2002 April 15 flare (Sui, Holman, & Dennis 2004 [52]) which was calculated to roughly track with a coronal loop observed by LASCO (similar to Figure 16 (top)). Sui, Holman,

& Dennis (2004 [52]) conjecture that “the outward-moving coronal source is part of an ejected plasmoid (or a large-scale, helically twisted loop) with two ends anchored on the Sun...”. This inference of “an ejected ... large-scale, helically twisted loop” matches our interpretation of the 2008 April 9 eruption invoking an erupted flux rope (Figure 32).

Liu et al. (2008 [26]) also report that their source closer to the solar surface has a larger emission measure than the higher one. These results are consistent with our “Disconnection Event” observations (see Section 3.2) where the upflow portion is much dimmer and more diffuse than its downflowing counterpart. Indeed, all of the upflows for this flare are dim compared to the bright downflows. This may be due to the difficulty in detecting the upflow signal based on its location high in the corona or possibly due to less compression from lower surrounding coronal densities. It is also worth noting that a non-radial, southward evolution of the loop-top source is reported for the flares in Sui, Holman, & Dennis (2004 [52]) (Figure 10 therein). The source of this divergence may have a similar mechanism as that proposed for the apparent southward drift of the CCS for this flare (Figure 20).

We interpret the basic standard picture of this eruptive flare as being initiated by the release of a flux rope by some means. As the flux rope escapes into the outer corona, a current sheet forms in its wake. Stretched magnetic field lines are swept together into the current sheet where reconnection occurs. This reconnection results in the formation of pairs of cusped, looped field lines, each moving in opposite

directions along the current sheet. The loops retracting toward the solar surface form the post-eruption arcade while their companion loops are swept into the outer corona along with the erupted flux rope. The post-eruption arcade follows the direction of the active region’s polarity inversion line (PIL). The current sheet also follows this direction as it spans the top of the developing arcade.

The “Cartwheel CME” flare offers a unique glimpse into nearly every facet of this flaring process due to long image exposures made possible by the limb occultation of the bright footpoints. The event is observed by several instruments (TRACE, *STEREO A*/SECCHI, *Hinode*/XRT, and LASCO). SECCHI observes the onset of the flux rope eruption near the solar surface. The formation of a candidate current sheet is seen by XRT, and we provide a possible explanation for its apparent southward progression being due to its position along an inclined PIL. (See Landi et al. (2010 [20]) for additional analysis of the CME.) Shrinking loops are very clearly seen in the XRT and SECCHI observations. Although typically very difficult to detect due to the low signal to noise above the flaring region, XRT is able to observe flows moving outward along the current sheet with one even clearly associated with a downflow. These upflows track into the outer corona where they appear to correspond with outflows seen by LASCO. Finally, a post-eruption arcade develops within both the XRT and SECCHI FOV. Any one of these observations provides an argument in favor of 3-D patchy reconnection flare models; however, all of these taken together makes the “Cartwheel CME” flare a very compelling candidate as direct proof of reconnection.

3.6. Acknowledgements

This work was supported by NASA grants NNM07AA02C0 & NNX08AG44G, NSF SHINE grant ATM-0752257, and NSF grant ATM-0837841. The authors wish to thank Drs. L. Sui, G. Holman, J. Raymond, and W. Liu for valuable discussions and suggestions. Hinode is a Japanese mission developed and launched by ISAS/JAXA, with NAOJ as domestic partner and NASA and STFC (UK) as international partners. It is operated by these agencies in co-operation with ESA and the NSC (Norway). Wilcox Solar Observatory data used in this study was obtained via the web site <http://wso.stanford.edu> courtesy of J.T. Hoeksema.

QUANTITATIVE EXAMINATION OF A LARGE SAMPLE OF SUPRA-ARCADE DOWNFLOWS IN ERUPTIVE SOLAR FLARES

4.1. Introduction

Long duration flaring events are often associated with downflowing voids and/or loops in the supra-arcade region (see Figure 38 for example images) whose theoretical origin as newly reconnected flux tubes has been supported by observations (McKenzie & Hudson 1999 [30]; McKenzie 2000 [29]; Innes et al. 2003a [14]; Asai et al. 2004 [1]; Sheeley, Warren, & Wang 2004 [46]; Khan et al. 2007 [17]; Reeves, Seaton, & Forbes 2008 [37]; McKenzie & Savage 2009 [31]; Savage et al. 2010 [40]).

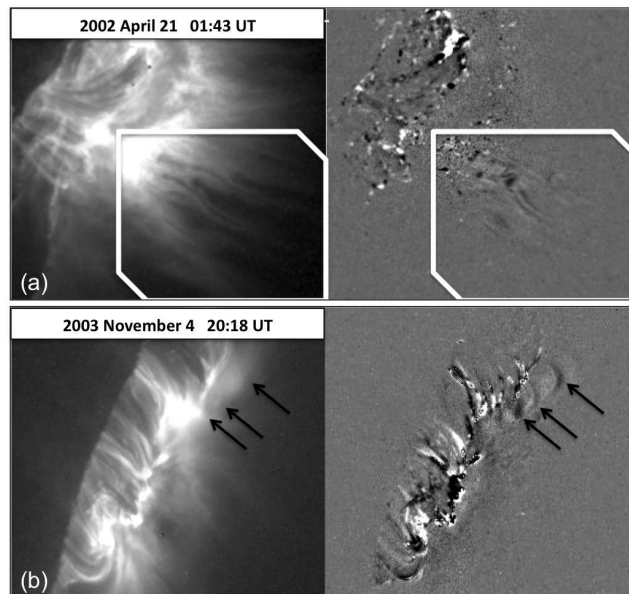


Figure 38: (a) Example image from the 2002 April 21 TRACE flare showing supra-arcade downflows (SADs) enclosed within the white box. (b) Example image from the 2003 November 4 flare with supra-arcade downflowing loops (SADLs) indicated by the arrows. The left panel of each set is the original image. The right panel has been enhanced for motion via run-differencing and scaled for contrast.

The downflowing voids, (a.k.a. supra-arcade downflows (SADs)), differ in appearance from downflowing loops (a.k.a. supra-arcade downflowing loops (SADLs)); however, the explanation for this can be derived simply from observational perspective. If the loops are viewed nearly edge-on as they retract through a bright current sheet, then SADs may represent the cross-sections of the SADLs (see Figure 39). Since neither SADs nor SADLs can be observed 3-dimensionally, proving this hypothetical connection is not possible with a single image sequence. However, their general bulk properties, such as velocity, size, and magnetic flux, can be measured and should be comparable if this scenario is correct. Moreover, measuring these parameters for a large sample of SADs and SADLs yields constraints that are useful for development of numerical models/simulations of 3D magnetic reconnection in the coronae of active stars.

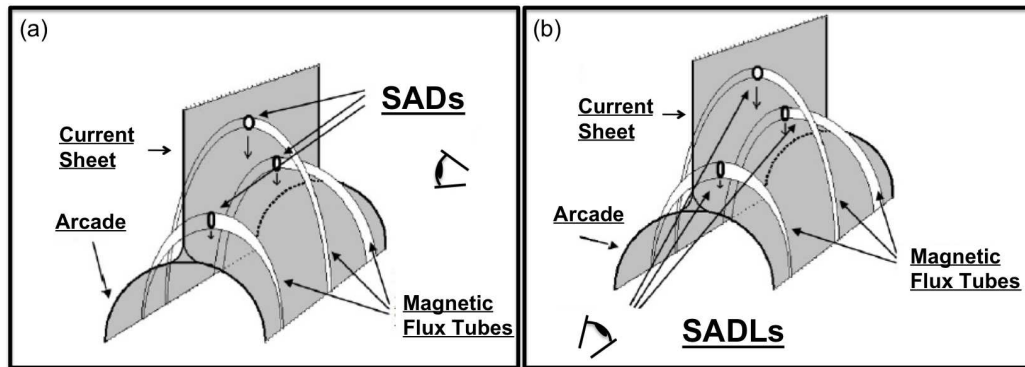


Figure 39: (a) Cartoon depiction of supra-arcade downflows (SADs) resulting from 3-D patchy reconnection. Discrete flux tubes are created, which then individually shrink, dipolarizing to form the post-eruption arcade. (b) Cartoon depiction of supra-arcade downflowing loops (SADLs) also resulting from 3-D patchy reconnection. Note that the viewing angle, indicated by the eye position, is perpendicular to that of SADs observations.

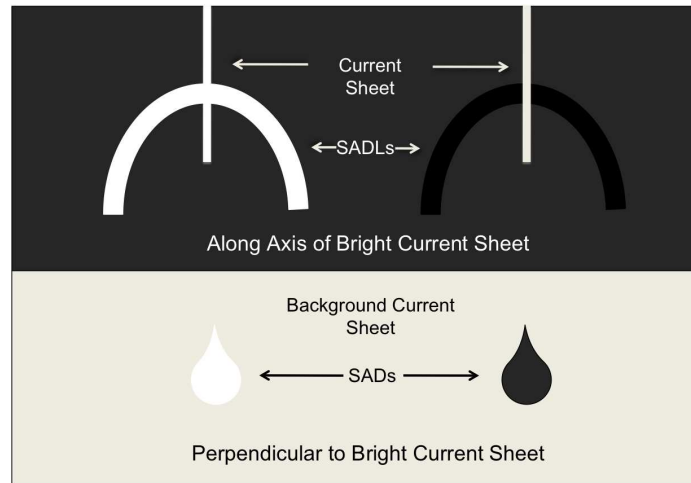


Figure 40: Diagram depiction illustrating the possible reason for the lack of bright SADs despite observations of bright SADLs with a snapshot of a loop shrinking through a bright current sheet with a viewing angle *Top*: along the arcade axis and *Bottom*: perpendicular to the axis. (Different scales) The loop is bright on the left of both panels and dark on the right. Because the current sheet is thin and in a region of low signal, the bright loops are easier to observe along the arcade axis which is opposite for the dark loops.

While bright shrinking loops (SADLs) are often observed as well as dark ones when the background has been sufficiently illuminated, bright SADs are rare. A possibility for the reason behind this lack of bright SADs observations is given in Figure 40. In order to view SADs, the loops are viewed edge-on to their apex cross-sections as they travel through the bright current sheet which provides a bright background. Consequently, if the loops are as bright as the current sheet, then they blend in with the background and are difficult to observe. Conversely, because the current sheet is thin, viewing it edge-on gives the appearance of a bright, thin line surrounded by a dark background against which the bright loops can be seen. The coronal background itself would need to be sufficiently illuminated in order to observe dark loops as they

retract. This is often not the case, however, because during a flare, the footpoints are so bright that the exposure durations applied to the images are not long enough to result in any significant coronal background signal.

In this chapter we provide a list of 62 flares observed by several instruments containing downflow signatures. We analyze flows from 35 of these flares and present comparative results of general bulk properties, including magnetic flux and shrinkage energy estimates, from SADs and SADLs in Section 4.2. These comparisons provide compelling evidence linking SADs to SADLs and constraints on flare magnetic reconnection models. Possible trends in the data are speculated in Section 4.2.2. The effect of simple drag on the loops is investigated in Section 4.2.4 as a possible reason for the slow downflow speeds. Finally, some loop cooling observations are presented in Section 4.2.5 relating the appearance of shrinking loops and the brightening of the arcade.

4.1.1. Observations

Because SADs and SADLs are located in regions of extremely low coronal emission near bright, dynamic sources, measurements for any one flow are naturally associated with a high degree of error. Therefore, in order to identify any trends in the data, analysis of several flows from each of many flares must necessarily be performed. Table 2 contains a list of flares which have been noted to display downflow signatures (i.e. observable SADs, SADLs, or swaying fan above the arcade as suggested by Khan et al. (2007 [17])). Several of these flares were selected from Khan et al. (2007 [17])

(see Table 1 therein) and were supplemented from McKenzie (2000 [29]) as well as by personal flare data investigation. Some flows from the Khan et al. (2007 [17]) list were excluded from this study if the presence of flows was not confirmed by visual inspection.

The majority of the flares are from SXT observations. Under the “Filter” heading in Table 2, the “Q-”, “H-” and the “F-” preceding the filter indicate whether the images examined are quarter-, half-, or full-resolution, respectively (where Q = 9.8, H = 4.9, & F = 2.5 arcsec/pix). The SXT resolution is about 2–10 times poorer than either TRACE (0.5 arcsec/pix) or XRT (1 arcsec/pix) (depending on SXT resolution); however, it was operational during two solar maxima (unlike XRT to date which has been operational primarily during an unusually quiet solar minimum) and observed hotter plasma than TRACE. Having the capacity to observe the hot plasma in the current sheet increases the height of flow observations. A few of the flares lack GOES assignments either because the SXR output was too low or the footpoints were too far beyond the limb to measure any significant signal.

Note that the TRACE flares in Table 2 are extremely energetic (as indicated by their GOES X1.5+ classifications). In addition, the TRACE flares are observed with the 195 Å filter which has temperature response peaks both in the .5 – 2 MK and 11 – 26 MK bandpasses. The high energies result in very high temperature plasma detectable above the underlying post-eruptive arcade. The increased intensity in the

supra-arcade region, presumably within the current sheet (Reeves et al. 2010 [36]), provides a bright background against which to observe the dark downflows.

Not all of the flares listed are suitable for tracking flows due to various factors (e.g. cadence, flow visibility, flare position, image quality, etc.). The last column of Table 2 indicates whether analysis of a flare was performed using the semi-automated routines described in Section 2.2 or a supplementary manual-tracking routine. Flows for 35 out of the 62 flares were evaluated. Table 3 includes a list of the analyzed flares from this study. Whether the flows were determined to be clearly shrinking loops (SADLs) is indicated in the table so that the SADs results can be compared with those of the SADLs. (Both SADs and SADLs are clearly observed in the 2002 April 21 TRACE event.) Also indicated is the position of the flare on the Sun. Flares beyond the limb are given a limb designation for the instrument FOV. Flares occurring on the disk (within $\sim 50^\circ$ from disk center) yield unreliable trajectory information due to the inability to accurately measure heights above the surface; therefore, their results are treated as detections only and removed from the following statistical analysis.

It should be noted that the number of flows being reported are those that were deemed to be the most reliable and complete although additional flows (> 50) have been processed. Inevitably, only a small percentage of the flows could be tracked for most flares due to noise, image quality, cadence, etc. – hence the need to process many flares in order to build up a catalog of flow parameters. The high resolution (0.5 arcsec/pix), high energy (GOES X1.5+) selected TRACE flares yield by far the

highest number of clearly defined, easily-trackable SADs and SADLs, but even in those flares, there is substantial untrackable downflowing motion whose shrinkage energy contribution cannot be included in the final total estimates. This motion is primarily present during the impulsive phase of the flare.

Table 2: List of flares exhibiting downflow signatures.

#	YYYYMMDD	Approx. Time	AR	GOES	FOV Coords	Instrument	Filter	Analyzed
1	19911216	12:30 - 14:30	06972	M3.2	E88 S08	SXT	H-Al12	
2	19920731	00:45 - 05:30	07244		E05 S00	SXT	Q-Al.1	
3	19921102	05:00 - 11:00	07321	X1.9	W90 S27	SXT	H-Al.1	
4	19930514	22:00 - 00:00	07500	M4.4	W50 N17	SXT	H-AlMg	
5	19930624	07:45 - 08:30	07529	M9.7	E74 S14	SXT	H-AlMg	
6	19940227	09:00 - 10:00	07671	M2.8	W88 N09	SXT	H-AlMg	
7	19980420	09:15 - 11:00	08202	M1.4	W92 S23	SXT	H-AlMg	
8	19980423	05:30 - 07:15	08210	X1.2	E91 S18	SXT	H-AlMg	✓
9	19980427	09:30 - 12:00	08210	X1.0	E54 S17	SXT	H-AlMg	✓
10	19980506	07:30 - 10:00	08210	X2.7	W65 S12	SXT	H-AlMg	✓
11	19980509	03:00 - 06:00	08210	M7.7	W91 S19	SXT	H-AlMg	✓
12	19980816	18:30 - 19:30	08306	M3.2	E94 N30	SXT	H-AlMg	✓
13	19980818	22:15 - 00:30	08306	M5.4	E94 N32	SXT	H-AlMg	
14	19980920	02:30 - 03:30	08340	M1.9	E62 N20	SXT	H-AlMg	
15	19980930	13:15 - 14:15	08340	M2.9	W92 N20	SXT	H-AlMg	✓
16	19981123	11:00 - 12:30	08392	M3.2	E60 S24	SXT	H-AlMg	✓
17	19981223	05:45 - 07:45	08421	M2.3	E89 N23	SXT	H-AlMg	✓
18	19990120	19:00 - 23:00	08446	M5.2	E87 N29	SXT	H-AlMg	✓
19	19990216	13:15 - 04:15	08458	M3.3	W17 S27	SXT	H-AlMg	
20	19990503	06:00 - 07:00	08530	M4.4	E47 N20	SXT	H-AlMg	✓
21	19990508	11:15 - 11:30	08541	M1.6	E78 N20	SXT	H-AlMg	
22	19990508	14:30 - 15:00	08526	M4.7	W80 N19	SXT	H-AlMg	
23	19990511	21:45 - 22:15	08542	C1.6	E87 S20	SXT	H-AlMg	
24	19990725	13:00 - 14:00	08639	M2.4	W93 N36	SXT	H-AlMg	✓
25	19991128	18:15 - 22:15	08771	M1.6	W89 S14	SXT	H-AlMg	✓
26	19991207	01:00 - 01:30	08781	C8.7	W89 S10	SXT	H-AlMg	
27	20000101	15:00 - 00:00			E N	LASCO	O+C	✓
28	20000222	20:15 - 21:30	08882	M1.1	E82 S19	SXT	H-AlMg	✓
29	20000712	02:30 - 03:45	09087	C5.3	E89 S11	SXT	H-AlMg	✓
30	20000712	21:00 - 22:00	09066	M1.9	W86 N15	SXT	H-AlMg	✓
31	20000930	17:45 - 18:45	09178	M1.0	E85 S32	SXT	H-AlMg	

Table 2 Continued.

#	YYYYMMDD	Approx. Time	AR	GOES	FOV Coords	Instrument	Filter	Analyzed
32	20001016	06:30 - 07:30	09193	M2.5	N05 W75	SXT	H-AlMg	✓
33	20001025	14:00 - 18:00	09199	C2.1	W69 N10	SXT	F-AlMg	
34	20001108	23:15 - 00:15	09213	M7.5	W90 N10	SXT	H-AlMg	✓
35	20001125	01:00 - 02:30	09240	M8.3	E51 N08	SXT	H-AlMg	
36	20010119	17:15 - 18:15	09313	M1.2	E58 S08	SXT	H-AlMg	
37	20010402	21:15 - 22:00	09393	X20	W70 N16	SXT	H-AlMg	✓
38	20010402	23:45 - 02:30	09393	M1.2	W70 N16	SXT	H-AlMg	✓
39	20010403	03:30 - 07:15	09415	X1.2	E89 S22	SXT	H-AlMg	✓
40	20010404	10:00 - 12:00	09415	M1.6	E59 S22	SXT	H-AlMg	
41	20010405	20:45 - 23:30	09415	M5.1	E47 S21	SXT	H-AlMg	
42	20010626	15:00 - 19:00			E90 S20	SXT	F-AlMg	✓
43	20010825	16:30 - 17:00	09591	X5.4	E28 S18	SXT	H-AlMg	
44	20010927	10:00 - 15:00	09628	M1.0	W39 S18	SXT	F-AlMg	✓
45	20011001	04:30 - 11:30	09632	M9.1	W75 S18	SXT	H-AlMg	
46	20011009	11:00 - 11:30	09653	M1.4	E11 S22	SXT	H-AlMg	✓
47	20011030	19:00 - 21:00	09687	C5.0	E90 S19	SXT	H-AlMg	✓
48	20011101	14:00 - 17:30	09687	M1.8	E90 S19	SXT	H-AlMg	✓
49	20011109	18:30 - 19:15	09687	M1.9	W31 S19	SXT	H-AlMg	✓
50	20011214	09:45 - 10:15	09742	M3.6	E90 N09	SXT	H-AlMg	
51	20020421	01:00 - 03:00	09906	X1.5	W91 S14	TRACE	195	✓
52	20020723	00:15 - 01:30	10039	X4.8	E54 S12	TRACE	195	✓
53	20031104	19:45 - 23:45	10486	X17	W89 S17	TRACE	195	✓
54	20061212	20:00 - 23:00	10930		W21 S05	XRT	Thin-Be	✓
55	20061213	02:30 - 05:00	10930	X3.4	W35 S06	XRT	Thin-Be	✓
56	20070313	01:00 - 11:00	10946		W86 N07	XRT	Ti-Poly	
57	20070509	03:00 - 06:00	10953		W91 S11	XRT	Ti-Poly	✓
58	20070520	19:45 - 20:30	10956		W21 N02	XRT	Ti-Poly	✓
59	20071217	06:00 - 10:00	10978	C2.2	W79 S10	XRT	C-Poly	
60	20071218	06:00 - 10:00	10978		W91 S09	XRT	C-Poly	
61	20080409	08:00 - 18:00	10989		W90 S18	XRT	Al-Poly	✓
62	20100613	02:00 - 05:30	11081		W72 N24	XRT	Ti-Poly	✓

Table 3: List of analyzed flares

#	YYYYMMDD	Instrument	# of Flows	SADs	SADLs	Limb	Disk
1	19980423	SXT	10	✓		E	
2	19980427	SXT	7	✓		E	
3	19980506	SXT	8		✓	W	
4	19980509	SXT	3	✓		W	
5	19980816	SXT	8	✓		E	
6	19980930	SXT	5	✓		W	
7	19981123	SXT	5	✓		E	
8	19981223	SXT	7		✓	E	
9	19990120	SXT	25	✓		E	
10	19990503	SXT	14	✓		E	
11	19990725	SXT	6	✓		W	
12	19991128	SXT	6	✓		W	
13	20000101	LASCO	11	✓		E	
14	20000222	SXT	6	✓		E	
15	20000712	SXT	7		✓	E	
16	20000712	SXT	10	✓		W	
17	20001016	SXT	6		✓	W	
18	20001108	SXT	2	✓		W	
19	20010402	SXT	11		✓	W	
20	20010403	SXT	5	✓		E	
21	20010626	SXT	9	✓		E	
22	20010927	SXT	4		✓	W	
23	20011009	SXT	2	✓			✓
24	20011030	SXT	3	✓		E	
25	20011101	SXT	4	✓		E	
26	20011109	SXT	2	✓		W	
27	20020421	TRACE	48	✓	✓	W	
28	20020723	TRACE	53		✓	E	
29	20031104	TRACE	60		✓	W	
30	20061212	XRT	6	✓			✓
31	20061213	XRT	6	✓			✓
32	20070509	XRT	2	✓		W	
33	20070520	XRT	1	✓			✓
34	20080409	XRT	16		✓	W	
35	20100613	XRT	9	✓		W	

4.1.2. Sources of Uncertainty

Several variables were measured for each flow including height, velocity, acceleration, area, magnetic flux, and shrinkage energy. A description of these measurements can be found in Section 2.2. Flows that were either too difficult for the automatic routine to follow or contained shrinking loops were tracked manually instead. Although conservatively determined by visually judging the cross-sectional diameters and extrapolating a circular area, areas assigned manually are typically smaller than those determined using the automatic threshold technique. All of the manually evaluated flows are assigned a single area per flare whereas the automatically determined areas vary in time. The manual trajectories are thus better determined though the flow sizes are not temporally flexible. This is especially true with SXT data because of the low spatial resolution. As noted in Section 2.3, degrading the resolution of TRACE images to that of SXT's half-resolution leads to flow areas comparable to that of SXT. The result is that several smaller flows become undetectable, some flows that are near one another spatially are combined, and several of the flow "heads" are merged with their trailing "tails" making them appear larger. The square root of the largest area extent is used as the error on the flow positions.

An additional large source of error is the initial height location. This height is biased by instrument-dependent detection capabilities (e.g. dynamic range and FOV) and is limited by the low emission high above the arcade. The initial height detection limits the path length of the measured flow trajectory which is used in the shrinkage

energy calculation. Of larger consequence, the initial height determines the initial magnetic field invoked from the PFSS model (Schatten et al. 1969 [41]; Schrijver & DeRosa 2003 [42]) to calculate the flux and shrinkage energy. The “Cartwheel CME” flare from 2008 April 9 (see Chapter 3) is a nice example of being able to observe near the actual flow initiation region due to long exposure durations enabled by limb-obscured footpoints. This is a rare example, however, because active regions are not often observed for long after crossing the western solar limb and it is difficult to anticipate flares prior to crossing the eastern limb. AIA, an EUV imager aboard the recently-launched Solar Dynamics Observatory (SDO), will improve the number of these necessary limb observations since it observes the full solar disk continuously.

Also noted in Chapter 2, the PFSS model itself is another source of uncertainty considering that the flows are associated with flaring active regions which are expected to be non-potential. It was estimated that the uncertainties from the model do not exceed about 30% (Priest, private communication). The larger contributions to the magnetic field uncertainty are therefore the height input into the model, the footpoints assigned to the flows, and the flare’s position on the Sun. Limb flares provide the optimum viewing angle for flow detections; however, the magnetograms used to extrapolate the magnetic fields into the corona are more reliable on the disk. Additionally, modeling for the east limb is even less reliable because magnetograms prior to the flare are unavailable. This discrepancy is shown in Figure 41 as the footpoint used for an X-class east limb flare (2002 July 23) is circled in panel (a)

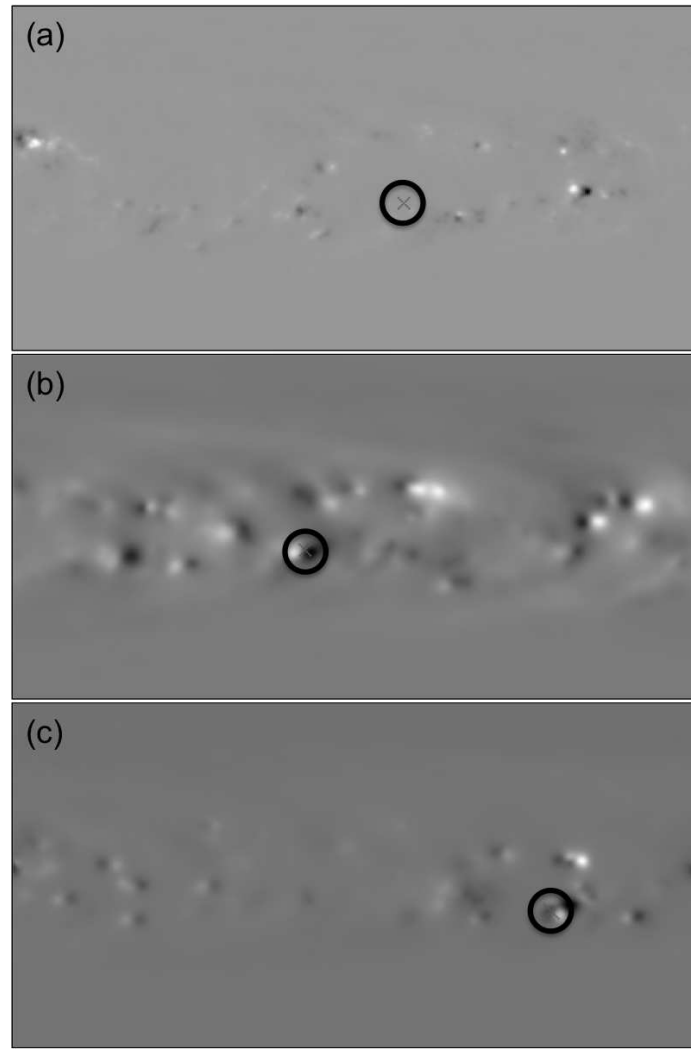


Figure 41: Radial magnetic fields derived from PFSS magnetic field modeling for the active regions producing flares observed by TRACE on a) 2002 July 23, b) 2002 April 21, and c) 2003 November 4. The initial height of the first flow per flare was used to create the figures. The footpoint region is circled. The west limb event in (a) predicts much weaker fields than the other two east limb events.

while the footpoints for X-class west limb flares (2002 April 21 & 2003 November 4) are circled in the bottom two panels. The initial height of the first flow per flare was used as a basis for the magnetic field represented in the panels. There is some variance, however, in the initial magnetic field strength between flows because the field

extrapolation depends on initial height. Note the strong magnetic field indicated by the magnetograms for the west limb flares compared to that of the east. Several of the flares in Table 3 occurred on the east limb (coordinates are shown in Table 2). Magnetic fields are still estimated for these flares. The effect of the underestimated magnetic field becomes apparent in Figure 44 (c).

Velocity results may be biased by the inability to track flows that are so fast they only show up in one frame or so slow that they are unobservable in the difference images. Most flows appear to be moving well within these constraints. Flows with areas near the resolution of the instrument are also difficult to detect which contributes an additional bias to the statistics. The obvious instrumental effect on area measurements is shown in Figure 43 (a).

4.2. Analysis

Considering these substantial uncertainty sources, flow measurements should be taken as imprecise; however, the large number of fairly well-defined flows (total of 387) tracked in the flares listed in Table 3 make it possible to consider ranges and trends in the data. Only the limb flares are considered hereafter which reduces the total number of flows to 372. The upflows tracked and analyzed for XRT 2008 April 9 (see Section 3.3.2) were also excluded bringing the total number of flows to be considered in the following sections to 369.

The Appendix containing the tables of measurements and histograms are divided as follows: 1) Average de-projected velocity; 2) Initial de-projected velocity; 3) Acceleration; 4) Area; 5) Initial height; 6) Change in height; 7) Magnetic flux; 8) Shrinkage energy. These plots are in turn divided by instrument combinations: 1) SXT; 2) TRACE; 3) XRT; 4) LASCO; 5) SXT & XRT; 6) SXT, XRT, & TRACE; 7) SXT, XRT, TRACE, & LASCO. SXT and XRT are plotted together because they have similar wavelength bandpasses providing a visual comparison between SXR and EUV. Not all histograms are provided with LASCO data due to its distinct observational characteristics – namely height and low resolution. The histograms are further subdivided into SADs versus SADLs except that the magnetic information plots are divided by east versus west limb instead. Each section of histograms is preceded by a table providing statistical information.

Note that all positional information is provided based upon the centroid of a trough location. Theoretically, tracking the head of the trough would constitute a more accurate assessment of its position because the centroid position may include portions of the growing wake behind the actual shrinking loop which could cause the velocities to appear slightly smaller. However, the automated routine relies on thresholds to determine the areas, and since each image is at least slightly different – especially when the exposure durations vary – the heads become much less reliable positions than the centroids. Because the areas are all the same for the manual routine, the centroid and head positions are merely shifted from one another.

4.2.1. Synthesis of Frequency Diagrams

The following plots synthesize the results of the tables provided in the Appendix into a more informative composition. Each plot shown in Figures 42, 43, and 44 consists of a quartile plot in the left panel and a histogram in the right. For the quartile plots, the measurement is plotted against the instrument (combination) being considered (S: SXT; X: XRT; T: TRACE; L: LASCO; All: S&X&T&L). For Figures 42 and 43, the left [red or purple] box-and-whisker range per instrument (or instrument combination) represents SADs measurements while the right [blue or purple] one represents SADLs measurements. For Figure 44, the east [pink or green] and west [olive or green] limbs are compared instead of SADs to SADLs. The lines (or whiskers) extending from the boxes indicate the full range of the data. The boxes span the range of the middle 50% of the data. The [white] line through the box indicates the median of the data. Along the top of these plots, the number of flows used to derive the associated measurements is labeled. The combination of the data in the final two [purple or green] box-and-whisker plots is contained within the histogram panel. The median of the histogram is displayed in the legend.

LASCO measurements are not included in Figures 43 or 44 since its resolution (11.4 arcsec/pix) is so much poorer and its observational regime high above the limb ($> 2.5 R_{\odot}$ for C2) is so very different from that of the other instruments, making comparisons more complicated. Deriving magnetic fields at such heights is not applicable with our method either plus determining precise footpoints without coincidental

data from other instruments is nearly impossible. The total number of flows under consideration after removing those observed by LASCO is 358.

Velocity & Acceleration. There is general agreement between SADs and SADLs, the instruments, and the SXR versus EUV bandpasses for the average velocity, initial velocity, and acceleration measurements (Figure 42). Note that the initial velocity and acceleration plots do not incorporate all 369 available flows. Instead, only those flows tracked in at least 5 frames were included because these measurements rely on fitting the trajectories to a 2D polynomial fit. Using fewer than 5 points leads to unreliable results. Also note that a positive downflow acceleration means that the flow is slowing.

Area. A strong correspondence between instrument resolution (SXT: 2.5 - 4.9 arcsec/pix; XRT: 1 arcsec/pix; TRACE: 0.5 arcsec/pix) and measured area is shown in the initial area quartile plot (Figure 43 (a)). The SADLs and XRT SADs area measurements are very strongly peaked due to their manual assignments – hence the lack of distinct quartiles.

Height. The initial height ranges (Figure 43 (b)) show decent agreement between the ranges; however, there is a fair amount of scatter in the medians which requires more detailed understanding of the analyzed flares to explain. The initial heights for both SADs and SADLs observed by SXT offer very good agreement. XRT observations, while agreeing with SXT's range of initial heights, show no agreement between

SADs and SADLs. This discrepancy is due to a combination of factors: 1) XRT has observed very few SADs as yet. 2) XRT observations are rarely sufficiently exposed to illuminate the supra-arcade region; therefore, XRT SADs have only been observed nearer to the solar surface. 3) The SADLs observed by XRT are derived from the “Cartwheel CME” flare (Chapter 3) during which the footpoints were obscured by the limb enabling very long exposure durations. In fact, the disconnection event associated with this flare (Section 3.3.2) was observed at nearly 190 Mm above the solar surface, which is at the max of the combined instrument ranges. TRACE’s temperature coverage targets plasma on order of 1 MK with some overlap in the 11 - 26 MK range with the SXR imagers. The image exposure durations are also optimized to observe the flaring region near the solar surface. Consequently, the observed initial heights of SADs and SADLs measured with TRACE are limited to the region near the top of the growing post-eruption arcade where the hot plasma in the current sheet is most illuminated. This results in initial heights lower than many of those reported for SXT and XRT.

The change in heights shown in Figure 43 (c) are naturally flare and FOV dependent. Even so, there is general agreement between SADs, SADLs, and instrument except for XRT. The explanation for this XRT discrepancy is the same as that for the initial height XRT discrepancy described above (i.e. the flows for the “Cartwheel CME” flare could be tracked further through the FOV).

Magnetic Measurements. The initial magnetic field histograms are not individually provided in the Appendix. Figure 44 (a) is provided as a visual reference only for the initial magnetic fields which are used to calculate the magnetic flux ($\Phi = B \times A$, Figure 44 (b)) and the shrinkage energy ($\Delta W = B^2 A \Delta L / 8\pi$, Figure 44 (c)). The initial magnetic field estimates for the TRACE flares are larger than the majority of those from SXT and XRT because 1) the TRACE flares analyzed are highly energetic according to their GOES classifications and 2) the flows are observed closer to the surface (see Figure 43 (b)) where the magnetic field is stronger according to the PFSS model (Schatten et al. 1969 [41]; Schrijver & DeRosa 2003 [42]). East and west limb measurements are compared in Figure 44 to show the effect of using less reliable east-limb magnetograms. The tendency for west limb flares to have stronger initial magnetic field estimates is noticeable in Figure 44 (a) and carries through into the initial magnetic flux and shrinkage energy plots (b & c, respectively). The dichotomy is most noticeable in the shrinkage energy estimates due to the B^2 component.

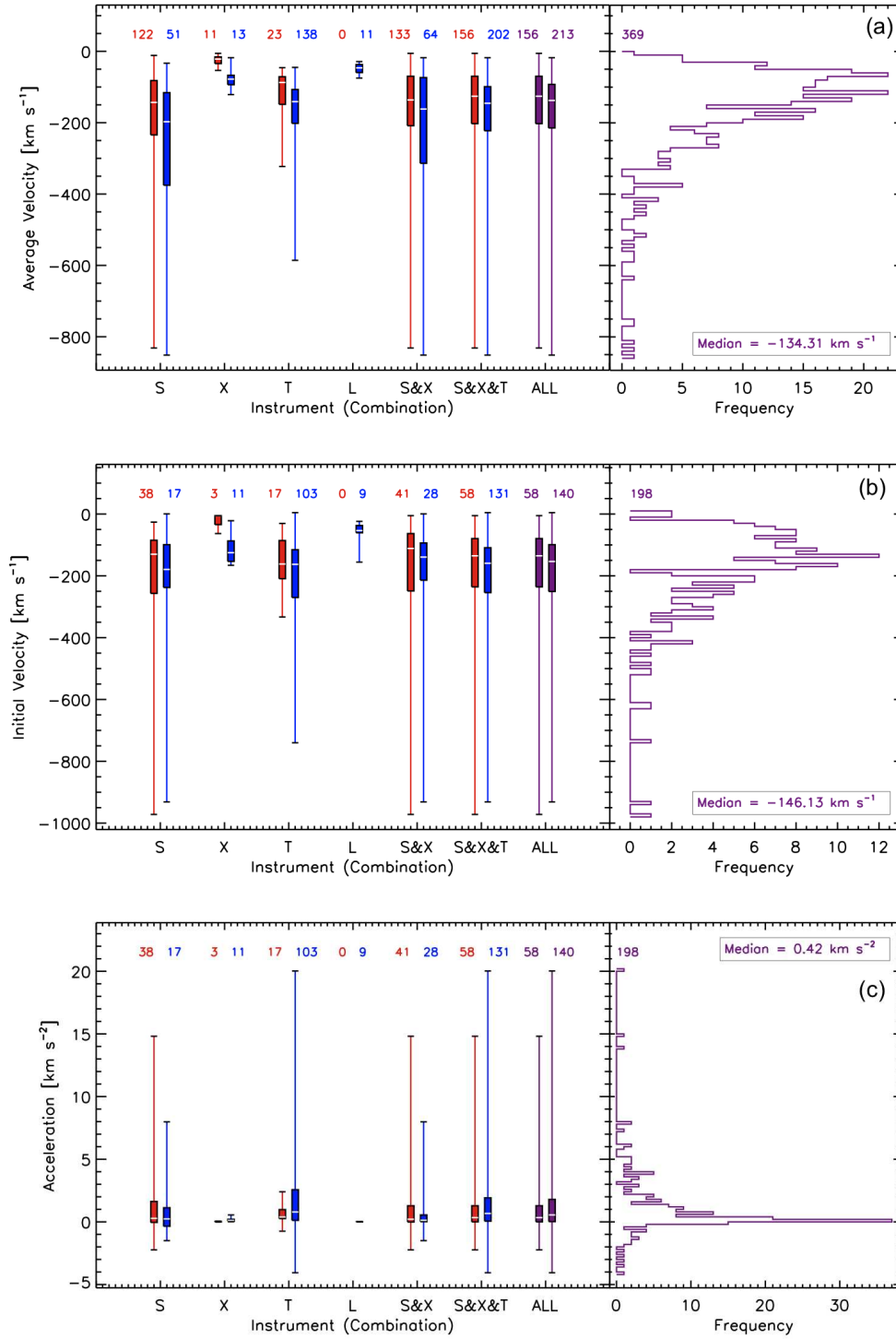


Figure 42: Synthesis of the de-projected trajectory information from Table 4. a) De-projected average velocity. b) De-projected initial velocity. c) De-projected acceleration. (Refer to the text for a detailed description of these figures.)

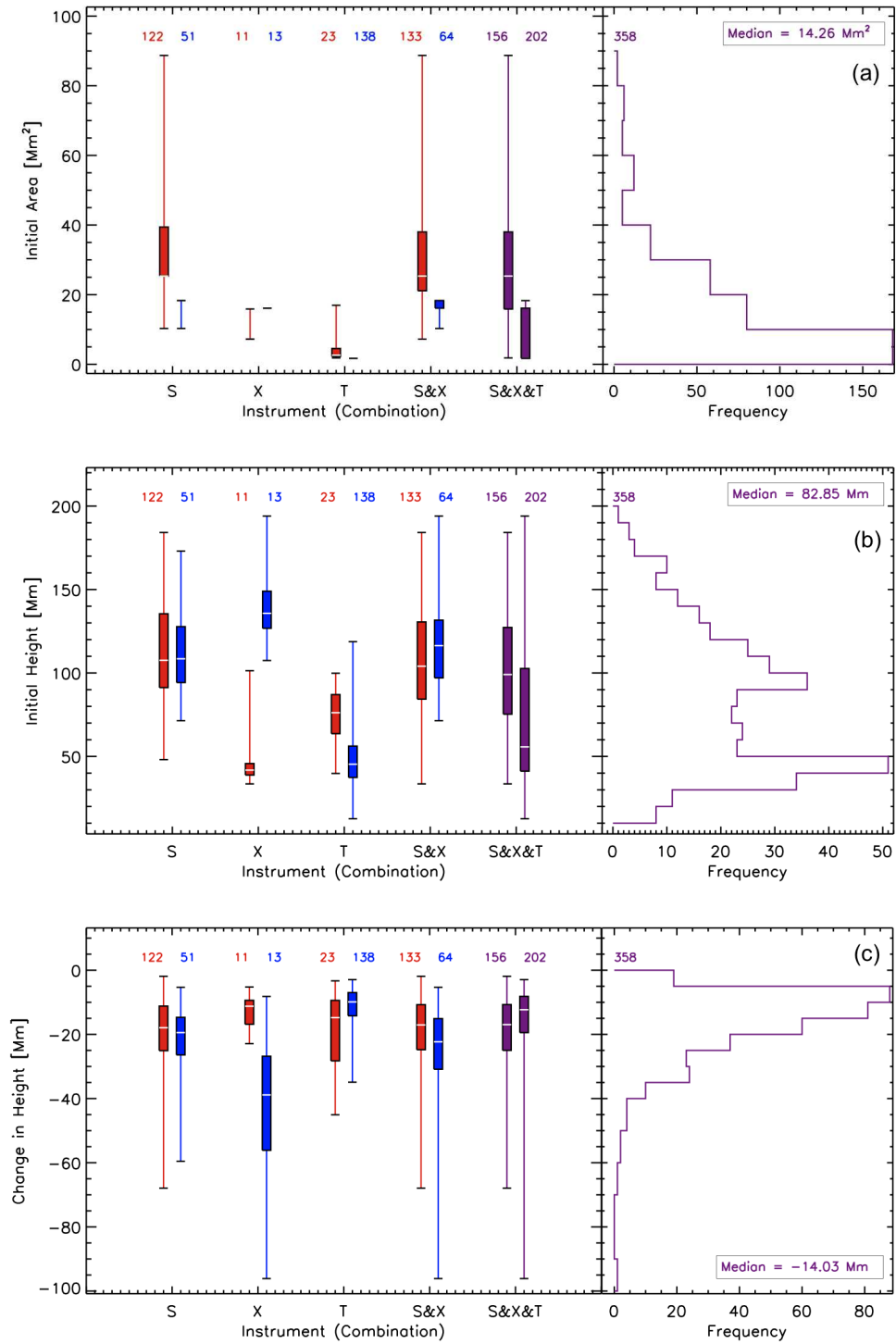


Figure 43: Synthesis of the area and height information from Table 4. a) Initial area. b) De-projected initial height. c) De-projected change in height. (Refer to the text for a detailed description of these figures.)

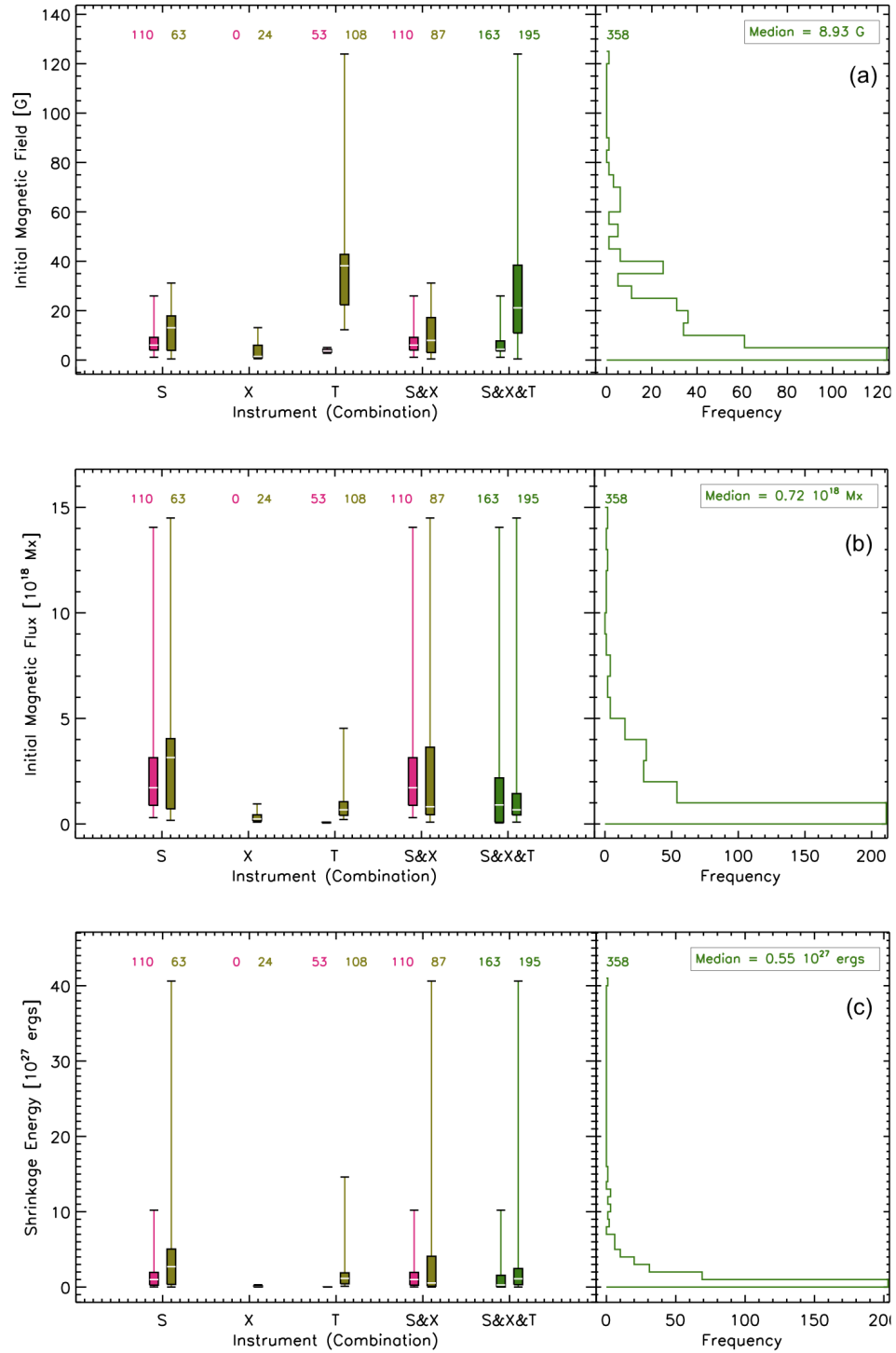


Figure 44: Synthesis of the magnetic information from Table 4. a) Initial magnetic field. b) Initial magnetic flux. c) Shrinkage energy. (Refer to the text for a detailed description of these figures.)

4.2.2. Trends

The following figure presents some of the interesting trends from analysis of the downflow data. Contained within the legends are the number of flows used to create the plot (#), the Spearman rank order correlation coefficient (S), the Spearman chance probability (%), and the Pearson linear correlation coefficient (P) (Hogg & Craig 1995 [12]). The coefficients can range from 0 to 1 with 1 indicating a perfect correlation. The Pearson coefficient applies to linear trends. Negative coefficients indicate anti-correlations between the parameters. The chance probability quantifies the likelihood of the data order occurring randomly. LASCO flows are only included in Figure 45 (d). The number of flows used in panel (a) is based only on those measured with the automatic threshold technique. Panels (b), (c), and (d) only include flows detected in at least 5 frames.

The apparent inverse relationship between field strength and flow area shown in Figure 45 (a) may be an artifact due to the larger detectable areas at higher heights (instrument independent). It is unclear as to whether this is a real effect or a result of poor signal to noise at such heights. The lack of directly measurable magnetic field strengths may also be skewing the data set. If the trend from Figure 45 (a) is real, then it suggests that a lower magnetic field strength results in a longer diffusion time (i.e. the amount of time that flux is able to reconnect) thereby allowing the flux tubes to increase in size.

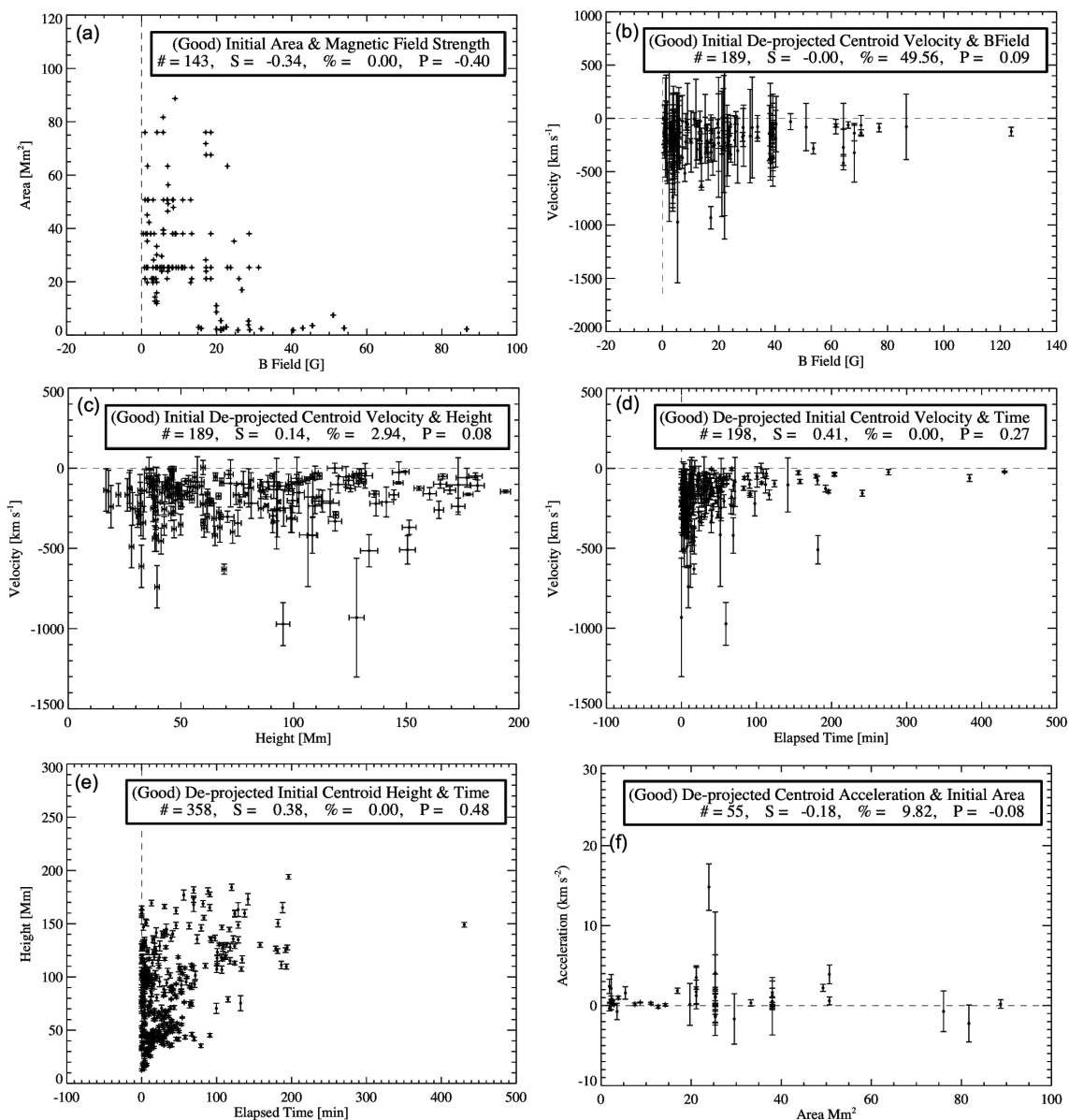


Figure 45: Selected trend plots. (a) Initial area (only for those measured via the threshold technique) versus initial magnetic field strength. (b) Initial de-projected velocity versus initial magnetic field strength. (c) Initial de-projected velocity versus initial de-projected height. (d) Initial de-projected velocity versus elapsed time. (e) Initial de-projected height versus elapsed time. The elapsed time is the time from the initial flow observation per flare. Contained with the legends are the number of flows used to create the plot (#), the Spearman rank order correlation coefficient (S), the Spearman chance probability (%), and the Pearson linear correlation coefficient (P).

Figure 45 (b) shows a very slight visual trend in favor of higher velocities with larger magnetic field strengths although the correlation coefficients do not support a trend. Few velocity measurements are available for very large magnetic fields. The lack of a strong trend is not so surprising, however, considering that the higher field strengths are associated with low heights, and these low initial heights are generally associated with flows near the top of the arcade where they are slowing considerably. More precise initial positions would be required to verify any link between speed and field strength.

Plotting the initial velocity against the initial height (Figure 45 (c)) also reveals a lack of correlation. These parameters, however, are highly sensitive to precise initial positions. There does appear to be a drop in speed at heights above 150 Mm. The disconnection event from the “Cartwheel CME” flare (Chapter 3) occurred near 190 Mm. It is possible that there is a region of flow acceleration as it exits the reconnection site and before it slows as it reaches the arcade. This plot may be indicating such a case; however, there are far too few high velocity points for this idea to be beyond speculative and one would expect for an acceleration region to be flare dependent. Also, in the 2002 April 21 TRACE event, fast-flowing loops are seen to be descending early during the impulsive phase, yet they are not positioned favorably for proper tracking. Knowing their precise speeds and initial heights could have a substantial effect on this plot in particular.

If approximating the flows as thin reconnected flux tubes, their velocity is expected to reflect the Alfvén speed in the corona (Linton & Longcope 2006 [25]) which has often been very roughly estimated to be 1000 km s^{-1} . The flows are traveling nearly an order of magnitude slower than this estimate. This discrepancy may partly be explained by the fact that the flow trajectories are incomplete and are being observed as they are approaching the post-eruption arcade. Interestingly though, the downflow portion of the disconnection event from the “Cartwheel CME” flare is estimated to have a maximum velocity of only about 150 km s^{-1} . (The upflow portion moves at about 120 km s^{-1} .)

Figure 45 (d) indicates that initial flow speeds are strongly correlated with time. The highest speeds are seen at the start of the flare. Indeed, this is generally confirmable by visual inspection. The 2002 April 21 TRACE event is a prime example of this trend. This is not an unexpected trend considering that the Alfvén speed is directly proportional to the magnetic field strength which decreases with height (Schatten et al. 1969 [41]; Schrijver & DeRosa 2003 [42]). (It is also true that the Alfvén speed is inversely proportional to the square root of the density which decreases with height; however, the progression of the flare may lead to an enhanced density in the current sheet through processes such as chromospheric evaporation and conduction (Reeves et al. 2010 [36]). Consequently, the decrease in the field strength should dominate the Alfvén speed response.) So while the flow speeds are not near the expected Alfvén speed, their decrease with height follows the expected Alfvén speed

trend, and it should be restated that precise measurements of the coronal magnetic field are unavailable at this time. Changes in loop geometry as it relaxes, which affects the tension force acting on the retracting loops, has not been taken into account with this simplistic check on the speeds.

Figure 45 (e) displays a strong positive correlation, present for all instruments, for flow observations at higher initial heights as the flare progresses, which can be satisfied by at least two explanations:

1) As the flare progresses, the reconnection site travels upwards as field lines reconnect higher along the current sheet. Using this explanation, however, would imply that the flows are being observed forming at the reconnection site.

2) As the flare progresses, more hot plasma is being conducted into the current sheet thereby brightening it at increasing heights (Reeves et al. 2010 [36]). The hot plasma then provides a bright background at increasing heights against which to observe the faint downflows.

While option 1 would be a nice verification of the standard CSHKP model, it is unrealistic except for the aforementioned “Cartwheel CME” flare wherein reconnection was observed to occur. However, option 2 could provide some insight into the rate of heating within the current sheet.

Finally, Figure 45 (f) shows the lack of a correlation between acceleration and initial area. This result could affect potential drag models which is introduced in

Section 4.2.4. Only flows that were measured using the automatic threshold technique and tracked in at least 5 frames are displayed.

4.2.3. Magnetic Derivations

Figure 46 provides a graphical display of the derivation of the magnetic flux and shrinkage energy with respect to elapsed time. The elapsed time is the time (in minutes) from the initial flow observation per flare. LASCO measurements are not included (see Section 4.2.1 for an explanation). One flow occurring after about 425 minutes of elapsed time has been excluded from the figures in order to better display the bulk of the data. The associated field strength of this flow is ~ 1 G.

While the correlation coefficients for Figure 46 (a) are marginal, the visual trend suggests an anti-correlation between magnetic field strength and time. The field strength is derived using the initial height position and is therefore very sensitive to the initial detection. Because the early flows are often detected closer to the solar surface as the supra-arcade region is brightening, their associated field strengths are strong. Conversely, the later flows can sometimes be detected at higher initial heights (refer to Figure 45 (e)) where the field strengths are lower.

Panel (b) does not support a correlation between the initial areas and elapsed flare time. The clusters of area measurements are a result of manual measurements. The discrete nature of the areas is due to pixelation.

The change in height is shown in panel (c). These values are negative because the final height is lower than the initial, so while the coefficients indicate a negative

correlation, the actual interpretation is that the magnitude of the change in height increases with elapsed flare time. This result is again due to the ability to measure initial positions higher above the arcade as the flare progresses and the supra-arcade region becomes more illuminated. The amount of time that an individual flow is tracked (Panel (d)) shows a positive correlation for this same reason.

Finally, magnetic flux ($\Phi = B \times A$ or (e) = (a) \times (b)) is shown in Figure 46 (e), and magnetic shrinkage energy ($\Delta W = B^2 A \Delta L / 8\pi$ or (f) $\propto ((a)^2 \times (b) \times (c)) / (d)$) is shown in (f). Neither parameter shows a strong correlation with elapsed time although both have slight visual trends similar to that of the magnetic field strength described above for panel (a). If this slight trend (admittedly visual only) is real and not just an artifact of the initial height biases previously discussed, this result indicates that the flux loops retracting earlier impart more energy into the flare compared to the later flows. This conclusion is consistent with the GOES SXR flare lightcurves which show most of the flare energy being released early with a slow decline in emission as the flare progresses. (This only applies to long duration events which are the subject of this study.)

Reconnection rates can be inferred by summing the flow fluxes and dividing by the total time of flow observations per flare. Five flares in this study have enough reliable flow detections to make this derivation meaningful. Reconnection rates are reported in Chapter 2 for the 1999 January 20, 2000 July 12, and 2002 April 21 flares (0.8×10^{16} , 2.3×10^{16} , and 1.2×10^{16} Mx s⁻¹, respectively). For the 2002 July 23

TRACE flare, $\sim 0.3 \times 10^{19}$ Mx was processed in 55 minutes, for a reconnection rate of 0.1×10^{16} Mx s⁻¹. Similarly, for the 2003 November 4 TRACE flare, $\sim 4.1 \times 10^{19}$ Mx was processed in 41 minutes, for a reconnection rate of 1.7×10^{16} Mx s⁻¹. The rates obtained for the 1999 January 20 and 2002 July 23 flares are underestimates because they occurred on the east limb. The east limb magnetic field measurements have been established as being consistently low due to the lack of current magnetograms (see Figures 41 & 44 (a)). Reconnection rates are not being reported for the 2008 April 9 flare despite its significant number of detectable flows because it occurred well beyond the limb making the magnetic field estimates unreliable. These reported reconnection rates may represent a lower bound considering that we can only include the flux and energy from detectable and trackable flows. Additional flows within the same time frame would increase the energy budget and, in turn, the reconnection rate.

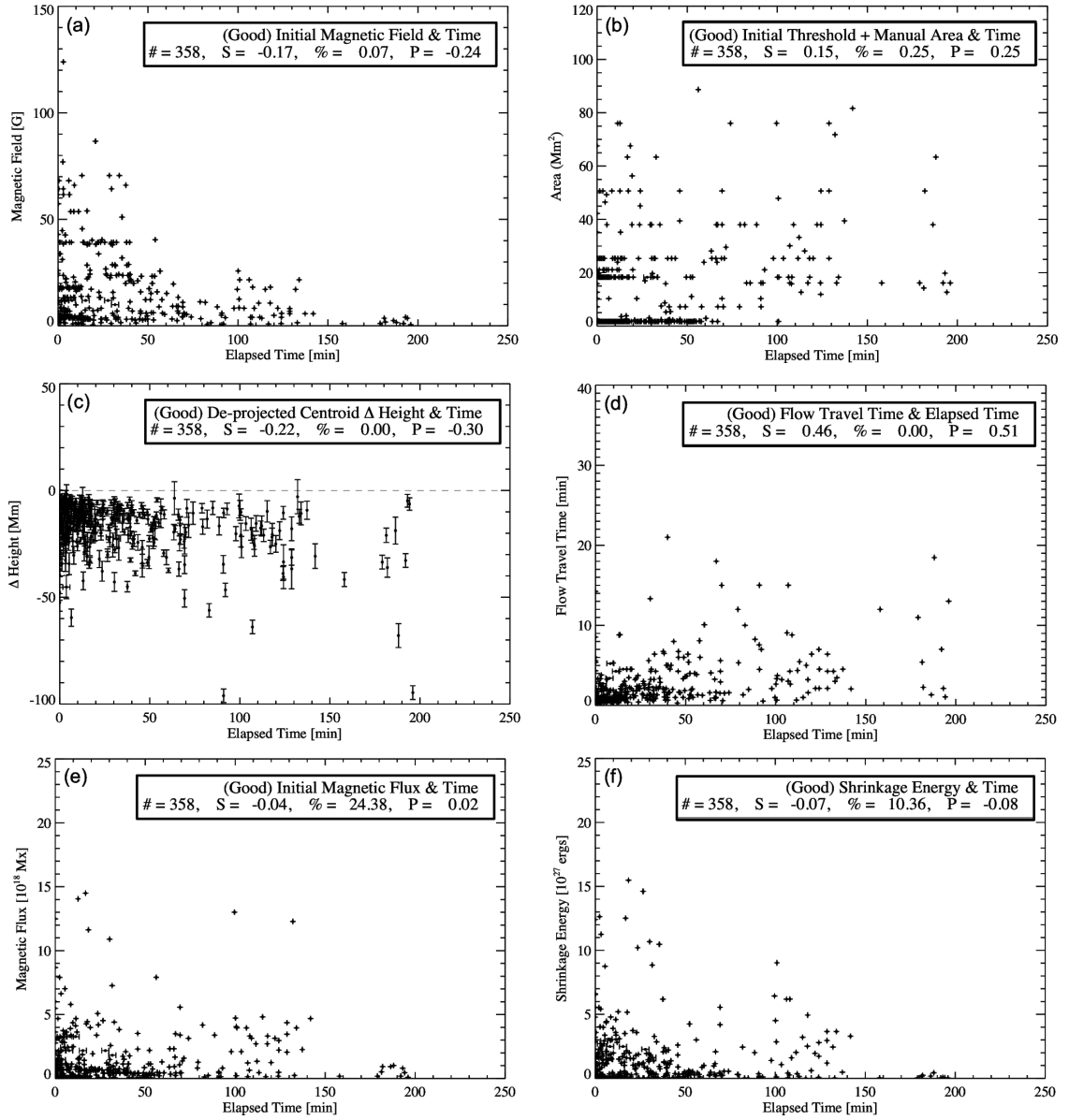


Figure 46: Trends with respect to elapsed time related to the calculation of shrinkage energy. Specifically, $\Delta W \propto ((a)^2 \times (b) \times (c)) / (d)$ and $(e) = (a) \times (b)$. (a) Initial magnetic field strength. (b) Initial area for troughs measured using the threshold technique and those measured manually. (c) Change in de-projected height. (d) Flow travel time. (e) Initial magnetic flux. (f) Shrinkage energy. The elapsed time is the time from the initial flow observation per flare. Contained with the legends are the number of flows used to create the plot ($\#$), the Spearman rank order correlation coefficient (S), the Spearman chance probability ($\%$), and the Pearson linear correlation coefficient (P).

4.2.4. Drag Analysis

Based on often-assumed estimates for coronal Alfvén speeds of about 1000 km s^{-1} , the flows seem to be moving well below predictions. This contradiction may not actually be the case considering that coronal Alfvén speeds cannot be well constrained. The signal is simply too low to measure the magnetic field or density precisely in the supra-arcade region. However, if the Alfvén speed is indeed on order of 1000 km s^{-1} , then the slow flow speeds can be attributed to at least two possibilities: 1) initial height and 2) drag.

The flows are expected to be accelerated from the reconnection site (the duration of acceleration is model-dependent) and slow as they settle near the top of the post-eruption arcade. The fact that the initial height estimates are associated with large uncertainty due to the lack of long exposure duration images of the supra-arcade region has been discussed in previous sections. Therefore, if the flows are initially observed far below the reconnection site, then the measured speed is likely to be slower than the actual initial speed. Note, however, that the measured speeds are still slow for the “Cartwheel CME” event near the reconnection region (Section 3.3.2). This bias has been well established, so in this section we will explore the second option – drag.

One way to test the effects of drag on the flows is to compare the trajectories to theoretical gravitational profiles. While the flows are not expected to be affected by gravity if they are plasma-deficient flux tubes, damped gravitational profiles provide

a method of comparing a known trajectory affected by drag with the shape of the flow profiles. This test was done for the flows from the “Cartwheel CME” event. Figure 47 provides a few example flow profiles with overlaid gravitational profiles as a thick dashed line.

The gravitational profiles were calculated using the flow initial height (h_0) and speed (v_0) (explicitly, $h = h_0 + v_0 t + 0.5 g_{\odot} t^2$, where t = time and g_{\odot} = acceleration due to gravity calculated as $g_{\odot} = -(6.67 \times 10^{-11} M_{\odot}) / ((R_{\odot} + h_0)^2)$). The thin dashed line is the gravitational profile with some constant damping in the form of Stokes’ drag ($F_d = -bv$) where the speed is thus calculated as $v = g_{\odot} / k + ((kv_0 - g_{\odot}) / k) \exp(-kt)$, where k = damping coefficient. This form of drag is being implemented based on its simplicity for this exercise. The drag coefficient is noted in the legend and was chosen as the value resulting in a profile closest to that of the original flow trajectory. A few of the flow profiles from this event match well with the gravitational profiles (e.g. Figure 47 (c)), but most begin to veer away towards the end of the track. Those tracks that do not appear to decelerate may be too incomplete to derive a proper acceleration. Additionally, the entire arcade is obscured by the limb for this event which makes following the flows until they reach their final configuration impossible.

The initial height from free-fall (drag-free) is noted in the legend along with a predicted final height for decelerating flows. No convergence among these values was found which is most likely due to the inability to observe and measure complete flow

tracks thus resulting in imprecise profiles. Also, the applied 2-D polynomial fit does not take into account changes in the acceleration which has a noticeable effect.

Considering how well the damped profiles match with the flow profiles, drag is a possible explanation to the slow-speed problem. As noted above, constant drag is being used to calculate the thin dashed profiles, but realistically the drag should be a function of height if it is due to the flows entering regions of higher density. Figure 48 supports the anti-correlation between height and drag with a Spearman rank order correlation coefficient of -0.44 and a linear correlation coefficient of -0.26. (Interestingly though, Figure 45 (f) does not indicate any correlation between acceleration and area. If the drag is a result of mass build-up in front of the flow, the expectation would be for the flows with larger areas to slow faster.) Some interpretations of these results are that either the Alfvén speed is lower than expected in the reconnection region, the drag may be overwhelming the magnetic tension force pulling down the loops causing them to retract slower, entanglement of field lines or plasma compressibility during the reconnection process reduces the initial speed, or even continual field entanglement during the retraction phase through the current sheet slows the flows. There is also the possibility that the flows are not retracting reconnected loops; however, several of the flare observations clearly show shrinking loop features, and the slowing of the flows as they approach the arcade would become difficult to explain otherwise.

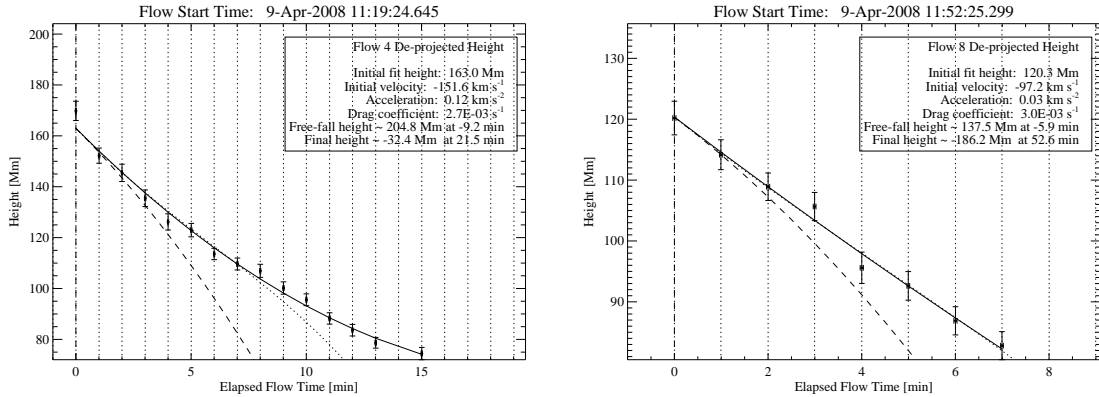


Figure 47: Example flow profiles from the 2008 April 9 “Cartwheel CME” event observed by XRT. The thick line represents the 2-D polynomial fit to the trajectory. The thick dashed line represents the gravitational profile calculated using the initial height and initial speed of the flow. The thin dashed line represents the gravitational profile with some constant damping coefficient applied. The thin dashed vertical lines indicate the times of the available images.

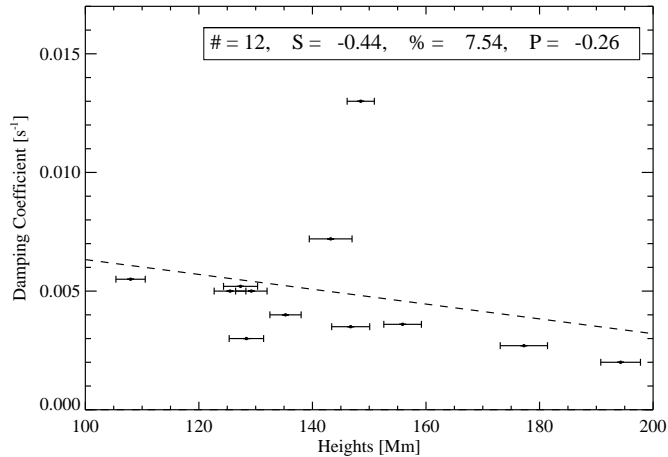


Figure 48: A plot of the applied drag constants, chosen to most closely match the flow profiles, versus initial height. The dashed line represents a linear fit to the data. Contained with the legend is the number of flows used to create the plot (#), the Spearman rank order correlation coefficient (S), the Spearman chance probability (%), and the Pearson linear correlation coefficient (P).

4.2.5. Loop Cooling

An interesting observation can be seen to occur during the 2002 April 21 and 2003 November 4 TRACE events wherein faint, hazy loops retract early during the impulsive phase along the length of the arcade. Between approximately 15–40 minutes later, bright, distinguishable post-eruption arcade loops appear without retracting in the same region. Figure 49 provides a visual reference of these loops and the delay. Deriving a more precise figure for this delay is complicated by the fact that a one-to-one correspondence cannot be established between a shrinking loop and an arcade loop. This delay is not observable in XRT images. Its appearance using TRACE is probably due to the use of the 195 Å filter which selects for temperatures of 0.5–2 MK and 11–26 MK. Therefore, while the hot loops have already settled, it appears to take the plasma within them, which is supplied through chromospheric evaporation, approximately 15–40 minutes to cool into the lower temperature passband. This has interesting implications: namely, that the early shrinking loops are either very hot to begin with, or that they quickly fill with hot plasma once they reach their potential configuration above the arcade. This delay cannot be measured in the SXT data because the arcade region is saturated.

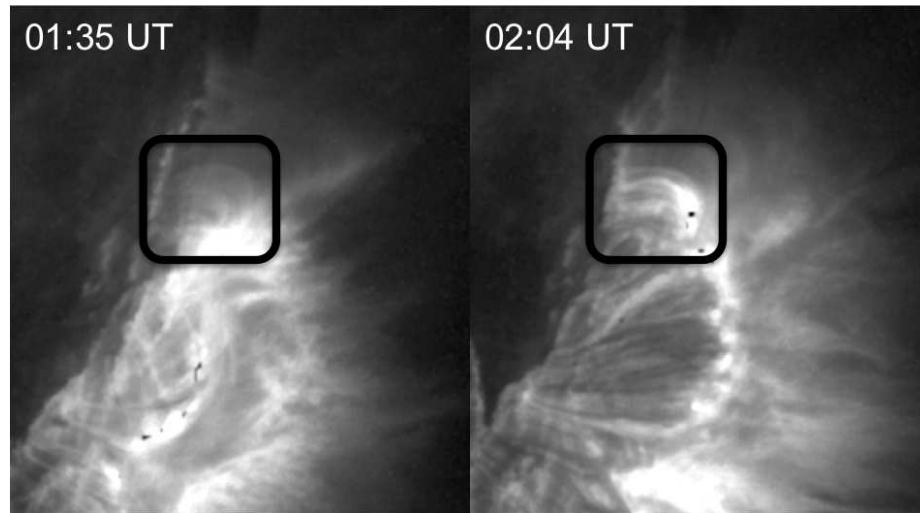


Figure 49: Images taken from the 2002 April 21 TRACE flare showing some of the post-eruption arcade loops cooling between the 195 Å temperature passbands.

4.2.6. Discussion & Conclusions

This chapter of analysis has presented many downflow observations from several instruments. Measurements of any one flow have too many possible sources of uncertainty to contribute to our understanding of the reconnection process occurring during long duration solar flares. SXT observed the most flares during its lifetime because it was operational throughout two solar maxima and was the first instrument to observe SADs; however, the poor spatial resolution leaves much to be desired with respect to being able to observe many flows per flare and make reliable measurements. LASCO has observed a number of flows in the outer corona; however, they are not always associated with flaring events, and because of the imager's much higher observational regime above the solar surface and considerably lower resolution, comparisons with

other SADs and SADLs observations are difficult to interpret. LASCO speeds and accelerations are the only parameters comparable to the other instruments. TRACE has the best resolution of all the instruments used for this study and has observed many hundreds of flares during its lifetime; however, flows are difficult to observe with TRACE unless the 195 Å filter is being utilized for broader temperature coverage and the flare is atypically large (all three TRACE flares in this study were GOES X-class flares). These requirements are due to the need for the hot plasma above the flare arcade to be illuminated. Finally, XRT has high enough spatial resolution to observe the flows as well as the optimal temperature coverage; however, solar activity has been unusually low throughout most of its lifetime to date making the amount of available flare data small. For all of these reasons, combining flow observations from all instruments improves our understanding of the flows themselves and ultimately our understanding of the reconnection process. Also, comparing the measurements between the instruments allows us to determine if the appearance of flows is temperature or density dependent.

Interpreting SADs as the cross-sections of retracting reconnected flux tubes also means that if they are viewed from an angle that is not near perpendicular to the arcade axis (i.e. the polarity inversion line), the downflows will instead appear as shrinking loops. These shrinking loops (SADLs) have indeed been clearly observed with all of the instruments under investigation. Therefore, comparing observations of SADs to those of SADLs can help to support the hypothesis for SADs or deny it.

Figures 42 through 44 present a nice summary of the instrument and SAD/SADL comparisons. These figures show that the flow velocities and accelerations agree between the instruments quite well. Height measurements agree except for those measured with XRT due to the exceptional heights observed for the “Cartwheel CME” flare. Figure 43 (a) shows that the area measurements are understandably resolution dependent, which indicates that we may not be able to observe the smallest loop sizes. The flux and energy measurements are area dependent and therefore instrument dependent. There is also a limb dependence with the magnetic measurements due to the use of modeling based on magnetograms. Even so, there is decent agreement between all of the instruments. (LASCO is only included with the velocity and acceleration comparisons as explained above).

Beyond the agreement between the SADs and SADLs measurements, the high-resolution TRACE observations clearly show both SADs and SADLs occurring during the same flare depending on the arcade viewing angle which curves within the active region. The SADs versus SADLs diagram shown in Figure 50 (previously Chapter 3 – Figure 37) still remains applicable after this analysis and has been updated to include magnetic estimates for SADLs.

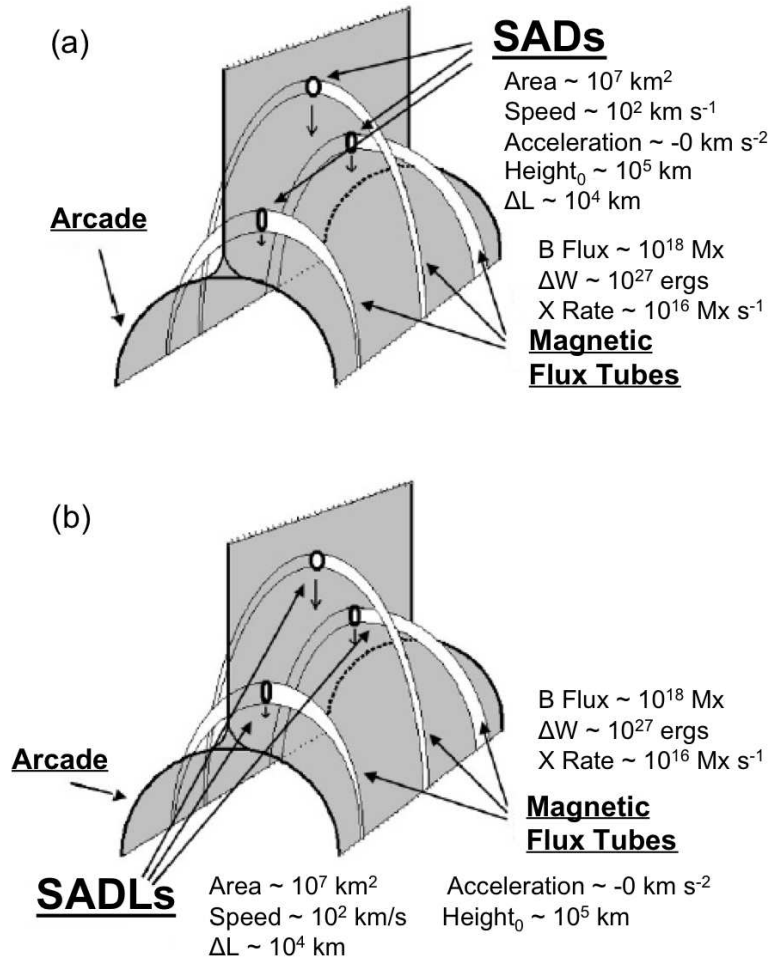


Figure 50: (a) Schematic diagram of supra-arcade downflows (SADs) resulting from 3-D patchy reconnection. Discrete flux tubes are created, which then individually shrink, dipolarizing to form the post-eruption arcade. The measured quantities shown are averages from the limb events listed in Table 3 containing SADs. (b) Schematic diagram of supra-arcade downflowing loops (SADLs) also resulting from 3-D patchy reconnection. The measured quantities shown are averages from the limb events listed in Table 3 containing SADLs.

These observations and measurements support the conclusion that SADs are indeed post-reconnection loops relaxing to form the post-eruption arcade. Also, the lack of instrument dependency of the dark flow observations suggests that either the loops are filled with cold material or are depleted. The temperature coverage of the instruments used in this study goes up to about 100 MK; therefore, it is unlikely that the loops are filled with hotter material. Combining this with the SUMER analysis of the 2002 April 21 TRACE flare from Innes et al. 2003a [14] which showed the lack of continuum absorption or emission in the C II, Fe XII, and Fe XXI lines at the flow sites supports the hypothesis that the tubes are depleted. This is at least true for loops reconnecting following the flare impulsive phase, which may be due to the fact that, according to the standard model, subsequent loops reconnect higher in the corona where less plasma is available to fill the loops. Loops shrinking very early during the 2002 April 21 TRACE flare appear to be bright in the hot 195 Å bandpass as noted in Section 4.2.5. Few bright flows are analyzed in this study because they are more difficult to observe as SADs due to the low contrast although bright SADLs have easily been observed (see Figure 40). Density analysis has not been performed due to the small sample of bright, tracked flows and especially lack of spectral coverage.

Assuming that SADs and SADLs are thin, post-reconnection loops based on the body of evidence presented in this chapter, the measurements obtained through this analysis and summarized in Figure 50 provide useful constraints for reconnection

models (e.g. area estimates can constrain the diffusion time per episode and reconnection rates can be derived to distinguish between fast and slow reconnection). The lack of acceleration of the downflow speeds and their discrete nature tends to favor 3D patchy Petschek reconnection. Speeds almost an order of magnitude slower than traditionally assumed Alfvén speeds are an unexpected consequence of the flow measurements; therefore, analyzing the effect of some source of drag on the downflow trajectories using models (an effort begun by Linton & Longcope (2006) [25]) could provide valuable insight into this discrepancy.

REFERENCES CITED

- [1] ASAI, A., YOKOYAMA, T., SHIMOJO, M., AND K., S. *ApJL* 605 (2004), L77.
- [2] CARMICHAEL, H. *AAS-NASA Symposium on the Physics of Solar Flares*, ed. W. N. Hess (1964), 451.
- [3] CIARAVELLA, A., AND RAYMOND, J. C. *ApJ* 686 (2008), 1372.
- [4] CIARAVELLA, A., RAYMOND, J. C., LI, J., REISER, P., GARDNER, L. D., KO, Y.-K., AND FINESCHI, S. *ApJ* 575 (2002), 1116.
- [5] FLETCHER, L., AND HUDSON, H. S. *Sol. Phys.* 204 (2001), 69.
- [6] FLETCHER, L., AND HUDSON, H. S. *ApJ* 675 (2008), 1645.
- [7] FORBES, T. G., AND ACTON, L. W. *ApJ* 459 (1996), 330.
- [8] FREELAND, S. L., AND HANDY, B. N. *Sol. Phys.* 182 (1998), 497.
- [9] GOLUB, L. E. A. *Sol. Phys.* 243 (2007), 63.
- [10] HANAOKA, Y. E. A. *PASJ* 46 (1994), 205.
- [11] HIRAYAMA, T. *Sol. Phys.* 34 (1974), 323.
- [12] HOGG, R. V., AND CRAIG, A. T. Introduction to mathematical statistics, 5th ed. (New York: Macmillan) (1995).
- [13] HUDSON, H. S. *ApJL* 531 (2000), L75.
- [14] INNES, D. E., MCKENZIE, D. E., AND WANG, T. *Sol. Phys.* 217 (2003a), 247.
- [15] INNES, D. E., MCKENZIE, D. E., AND WANG, T. *Sol. Phys.* 217 (2003b), 267.
- [16] JAGGI, R. K. *AAS-NASA Symposium on the Physics of Solar Flares*, ed. W. N. Hess (1964), 419.
- [17] KHAN, J. I., BAIN, H. M., AND FLETCHER, L. *A&A* 475 (2007), 333.
- [18] KO, Y. K., RAYMOND, J. C., LIN, J., LAWRENCE, G., LI, J., AND FLUDRA, A. *ApJ* 594 (2003), 1068.

- [19] KOPP, R. A., AND PNEUMAN, G. W. *Sol. Phys.* 50 (1976), 85.
- [20] LANDI, E., RAYMOND, J. C., MIRALLES, M. P., AND HARA, H. *ApJ* 711 (2010), 75.
- [21] LIN, J. *Sol. Phys.* 222 (2004), 115.
- [22] LIN, J., AND FORBES, T. G. *JGR* 105, A2 (2000), 2375.
- [23] LIN, J., KO, Y.-K., SUI, L., RAYMOND, J. C., STENBORG, G. A., JIANG, Y., ZHAO, S., AND MANCUSO, S. *ApJ* 622 (2005), 1251.
- [24] LIN, J., LI, J., FORBES, T. G., KO, Y.-K., RAYMOND, J. C., AND VOURLIDAS, A. *ApJL* 658 (2007), L123.
- [25] LINTON, M., AND LONGCOPE, D. W. *ApJ* 642 (2006), 1177.
- [26] LIU, W., PETROSIAN, V., DENNIS, B. R., AND JIANG, Y. W. *ApJ* 676 (2007), 704.
- [27] LONGCOPE, D. W., GUIDONI, S. E., AND LINTON, M. G. *ApJL* 690 (2009), L18.
- [28] LONGCOPE, D. W., MCKENZIE, D. E., CIRTAİN, J., AND SCOTT, J. *ApJ* 630 (2005), 596.
- [29] MCKENZIE, D. E. *Sol. Phys.* 195 (2000), 381.
- [30] MCKENZIE, D. E., AND HUDSON, H. S. *ApJL* 519 (1999), L93.
- [31] MCKENZIE, D. E., AND SAVAGE, S. L. *ApJ* 697 (2009), 1569.
- [32] NARUKAGE, N., AND SHIBATA, K. *ApJ* 637 (2006), 1122.
- [33] PARKER, E. N. *ApJS* 8 (1963), 177.
- [34] PETSCHKE, H. E. *AAS-NASA Symposium on the Physics of Solar Flares*, ed. W. N. Hess (1964), 425.
- [35] PRIEST, E., AND FORBES, T. *Magnetic Reconnection: MHD Theory and Applications*. (Cambridge, UK: Cambridge University Press) (2000).
- [36] REEVES, K., LINKER, J. A., MIKIĆ, Z., AND FORBES, T. G. *ApJ* 721 (2010), 1547.

- [37] REEVES, K., SEATON, D., AND FORBES, T. *ApJ* 675 (2008), 868.
- [38] REGNIER, S., AND PRIEST, E. *ApJL* 669 (2007), L53.
- [39] SABA, J. L. R., GAENG, T., AND TARBELL, T. D. *Multi-Wavelength Observations of Coronal Structure and Dynamics—Proceedings of the Yohkoh 10th Anniversary Meeting*, eds. P.C.H. Martens and D. Cauffman (2001), 175.
- [40] SAVAGE, S. L., MCKENZIE, D. E., REEVES, K. K., FORBES, T. G., AND LONGCOPE, D. W. *ApJ* 722 (2010), 329.
- [41] SCHATTEN, K. H., WILCOX, J. M., AND NESS, N. F. *Sol. Phys.* 6 (1969), 442.
- [42] SCHRIJVER, C. J., AND DEROSA, M. L. *Sol. Phys.* 212 (2003), 165.
- [43] SEATON, D. B., AND FORBES, T. G. *ApJ* 701 (2009), 348.
- [44] SHEELEY, N. R., AND WANG, Y.-M. *ApJ* 579 (2002), 874.
- [45] SHEELEY, N. R., AND WANG, Y.-M. *ApJ* 655 (2007), 1142.
- [46] SHEELEY, N. R., WARREN, H. P., AND WANG, Y.-M. *ApJ* 616 (2004), 1224.
- [47] SHIBATA, K. *Ap&SS* 264 (1999), 129.
- [48] SHIBATA, K., MASUDA, S., SHIMOJO, M., HARA, H., YOKOYAMA, T., TSUNETA, S., KOSUGI, T., AND OGAWARA, Y. *ApJL* 451 (1995), 83.
- [49] SOMOV, B. V. *Physical Processes in Solar Flares*. (Dordrecht: Kluwer) (1992), 192.
- [50] STURROCK, P. A. *IAU Symp. 35: Structure and Development of Solar Active Regions* (1968), 471.
- [51] SUI, L., AND HOLMAN, G. *ApJL* 596 (2003), 251.
- [52] SUI, L., HOLMAN, G., AND DENNIS, G. *ApJ* 612 (2004), 546.
- [53] ŠVESTKA, Z., FRANIK, F., HUDSON, H., AND HICK, P. *Sol. Phys.* 182 (1998), 179.
- [54] SWEET, P. A. *Electromagnetic Phenomena in Cosmical Physics* 6 (1958), 123.

- [55] TRIPATHI, D., ISOBE, H., AND MASON, H. E. *A&A* 453 (2006a), 1111.
- [56] TRIPATHI, D., SOLANKI, S. K., MASON, H. E., AND WEBB, D. F. *A&A* 472 (2007), 633.
- [57] TRIPATHI, D., SOLANKI, S. K., SCHWENN, R., BOTHMER, V., MIERLA, M., AND STENBORG, G. *A&A* 449 (2006b), 369.
- [58] VERWICHTE, E., NAKARIAKOV, V. M., AND COOPER, F. C. *A&A* 430 (2005), L65.
- [59] WANG, T. J., SOLANKI, S. K., INNES, D. E., AND CURDT, W. *ESA SP-505: SOLMAG 2002. Proceedings of the Magnetic Coupling of the Solar Atmosphere Euroconference*, ed. H. Sawaya-Lacoste (2002), L69.
- [60] WEBB, D. F., BURKEPILE, J., FORBES, T. G., AND RILEY, P. *JGR* 108, A12 (2003), 1440.
- [61] YOKOYAMA, T., AKITA, K., MORIMOTO, T., INOUE, K., AND NEWARK, J. *ApJL* 546 (2001), L69.
- [62] YOKOYAMA, T., AND SHIBATA, K. *ApJL* 494 (1998), L113.

APPENDICES

APPENDIX A

FLOW TABLES & HISTOGRAMS

4.2.7. Histograms

Average De-projected Velocity.

	SXT	XRT	TRACE	LASCO	Figure	# of Flows	Median [km s ⁻¹]	Range [km s ⁻¹]
All Limb	✓				51 (a)	173	-161	-9 – -839
		✓			51 (b)	24	-51	-6 – -121
			✓		51 (c)	161	-134	-45 – -586
				✓	51 (d)	11	-46	-29 – -75
	✓	✓			51 (e)	197	-140	-5 – -851
	✓	✓	✓		51 (f)	358	-138	-6 – -851
	✓	✓	✓	✓	51 (g)	369	-134	-6 – -851
SADs	✓				52 (a)	122	-143	-11 – -832
		✓			52 (b)	11	-22	-6 – -53
			✓		52 (c)	23	-87	-46 – -323
	✓	✓		✓	52 (d)	133	-136	-6 – -832
	✓	✓	✓		52 (e)	156	-123	-6 – -832
SADLs	✓				53 (a)	51	-197	-33 – -851
		✓			53 (b)	13	-78	-18 – -121
			✓		53 (c)	138	-139	-45 – -586
				✓	53 (d)	11	-46	-29 – -75
	✓	✓			53 (e)	64	-162	-18 – -851
	✓	✓	✓		53 (f)	202	-145	-18 – -851
	✓	✓	✓	✓	53 (g)	213	-138	-18 – -851

Table 4: Average de-projected velocities statistics.

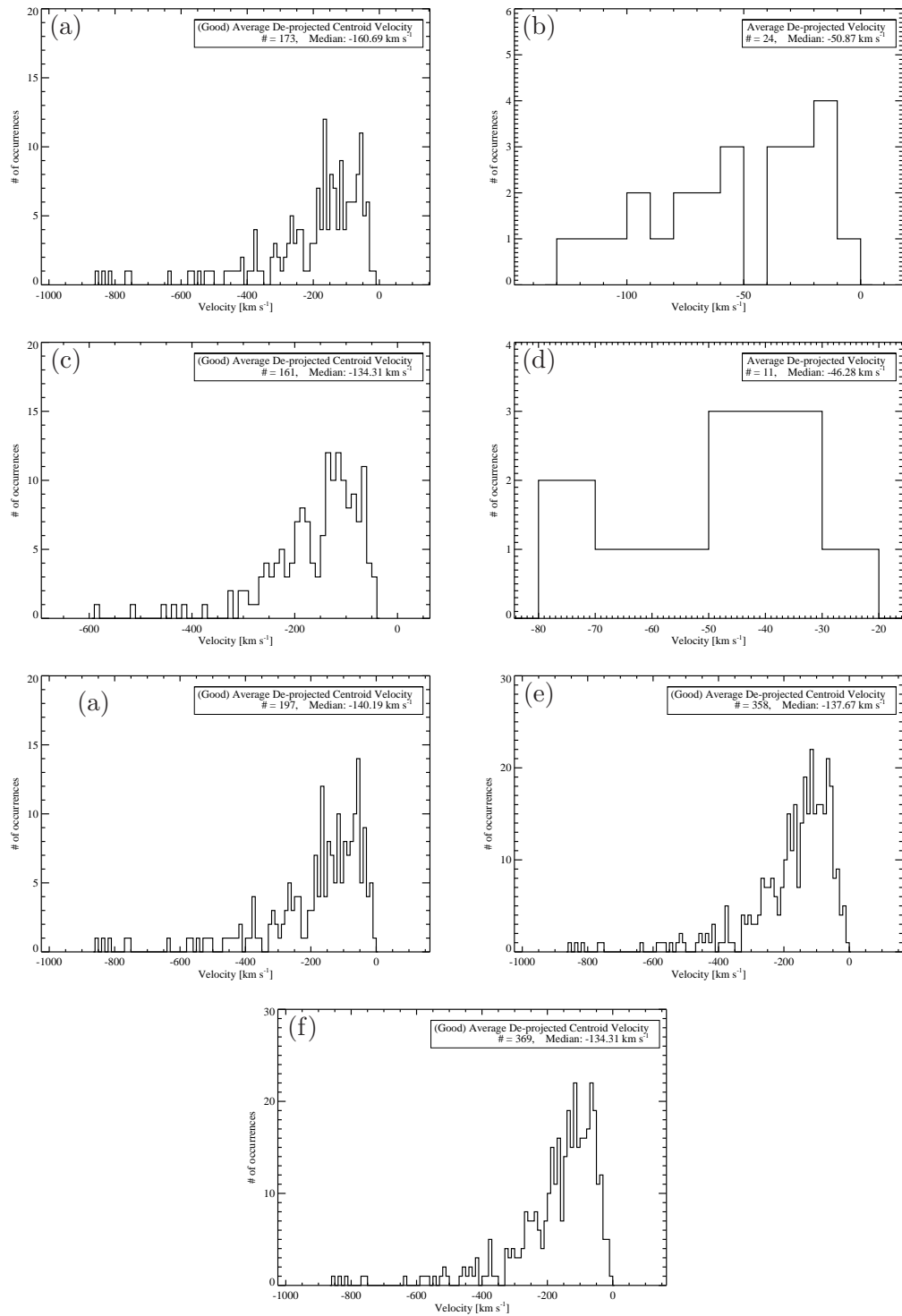


Figure 51: Histograms displaying average velocity frequency for the limb flares from this study as observed by a) SXT, b) XRT, c) TRACE, d) LASCO, e) SXT & XRT, f) SXT, XRT, & TRACE, and g) SXT, XRT, TRACE, & LASCO.

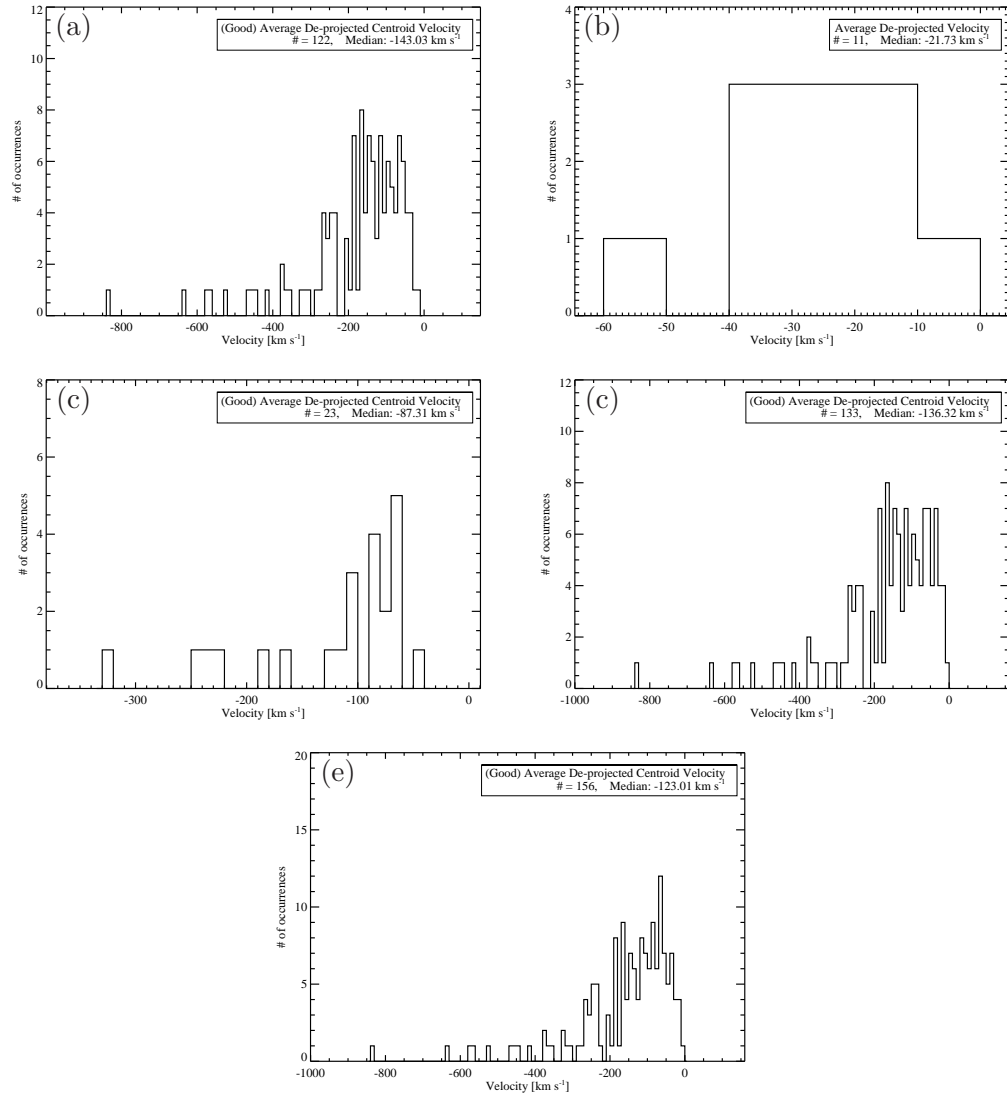


Figure 52: Histograms displaying average velocity frequency for the limb flares from this study which contained SADs as observed by a) SXT, b) XRT, c) TRACE, d) SXT & XRT, and e) SXT, XRT, & TRACE.

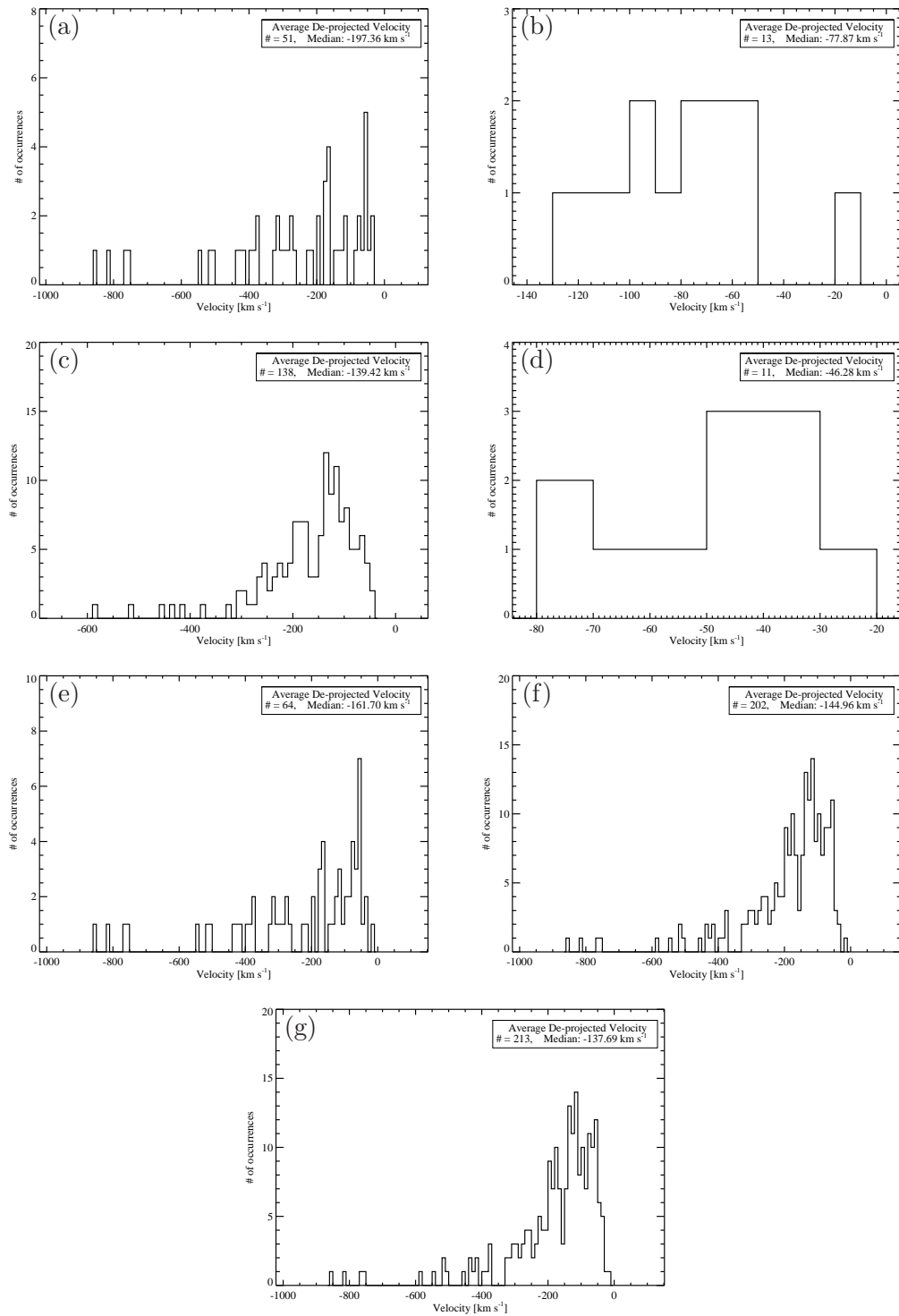


Figure 53: Histograms displaying average velocity frequency for the limb flares from this study which contained SADLs as observed by a) SXT, b) XRT, c) TRACE, d) LASCO, e) SXT & XRT, f) SXT, XRT, & TRACE, and g) SXT, XRT, TRACE, & LASCO.

Initial De-projected Velocity.

The initial velocities below are only shown for flows tracked in at least 5 frames since they are calculated using 2-D polynomial fitting.

	SXT	XRT	TRACE	LASCO	Figure	# of Flows	Median [km s ⁻¹]	Range [km s ⁻¹]
All Limb	✓				54 (a)	55	-152	-0.5 – -972
		✓			54 (b)	14	-91	-5 – -166
			✓		54 (c)	120	-162	-4.4 – -740
				✓	54 (d)	9	-53	-24 – -156
	✓	✓			54 (e)	69	-126	-0.5 – -972
	✓	✓	✓		54 (f)	189	-155	-0.5 – -972
	✓	✓	✓	✓	54 (g)	198	-146	-0.5 – -972
SADs	✓				55 (a)	38	-123	-26 – -972
		✓			55 (b)	3	-5	-5 – -63
			✓		55 (c)	17	-162	-30 – -333
	✓	✓		✓	55 (d)	41	-111	-4 – -972
	✓	✓	✓		55 (e)	58	-133	-5 – -972
SADLs	✓				56 (a)	17	-179	-0.5 – -931
		✓			56 (b)	11	-125	-22 – -166
			✓		56 (c)	103	-163	-4.4 – -740
				✓	56 (d)	9	-53	-24 – -156
	✓	✓			56 (e)	28	-133	-0.5 – -931
	✓	✓	✓		56 (f)	131	-159	-0.5 – -931
	✓	✓	✓	✓	56 (g)	140	-152	-0.5 – -931

Table 5: Initial de-projected velocity statistics.

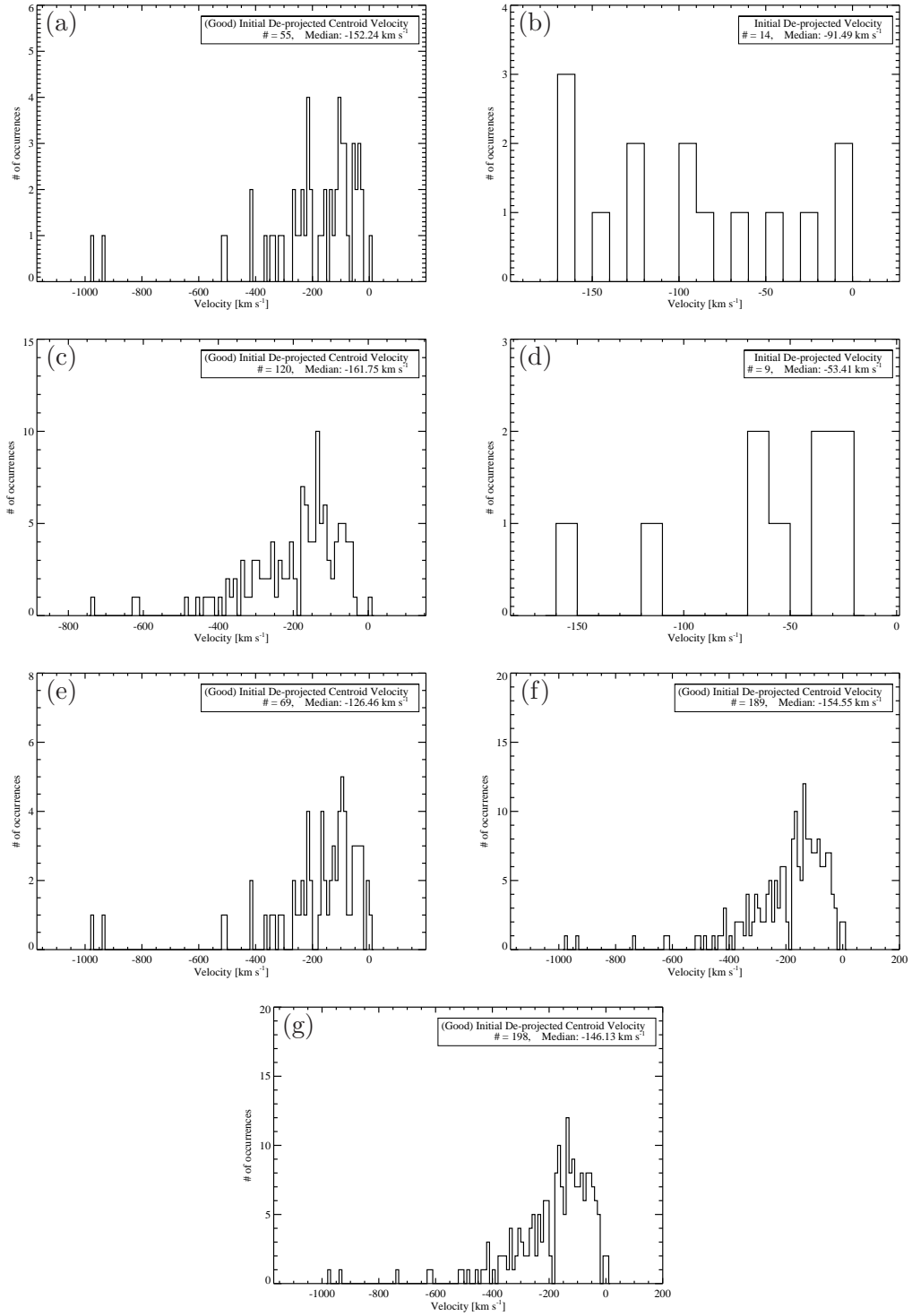


Figure 54: Histograms displaying initial velocity frequency for the limb flares from this study as observed by a) SXT, b) XRT, c) TRACE, d) LASCO, e) SXT & XRT, f) SXT, XRT, & TRACE, and g) SXT, XRT, TRACE, & LASCO.

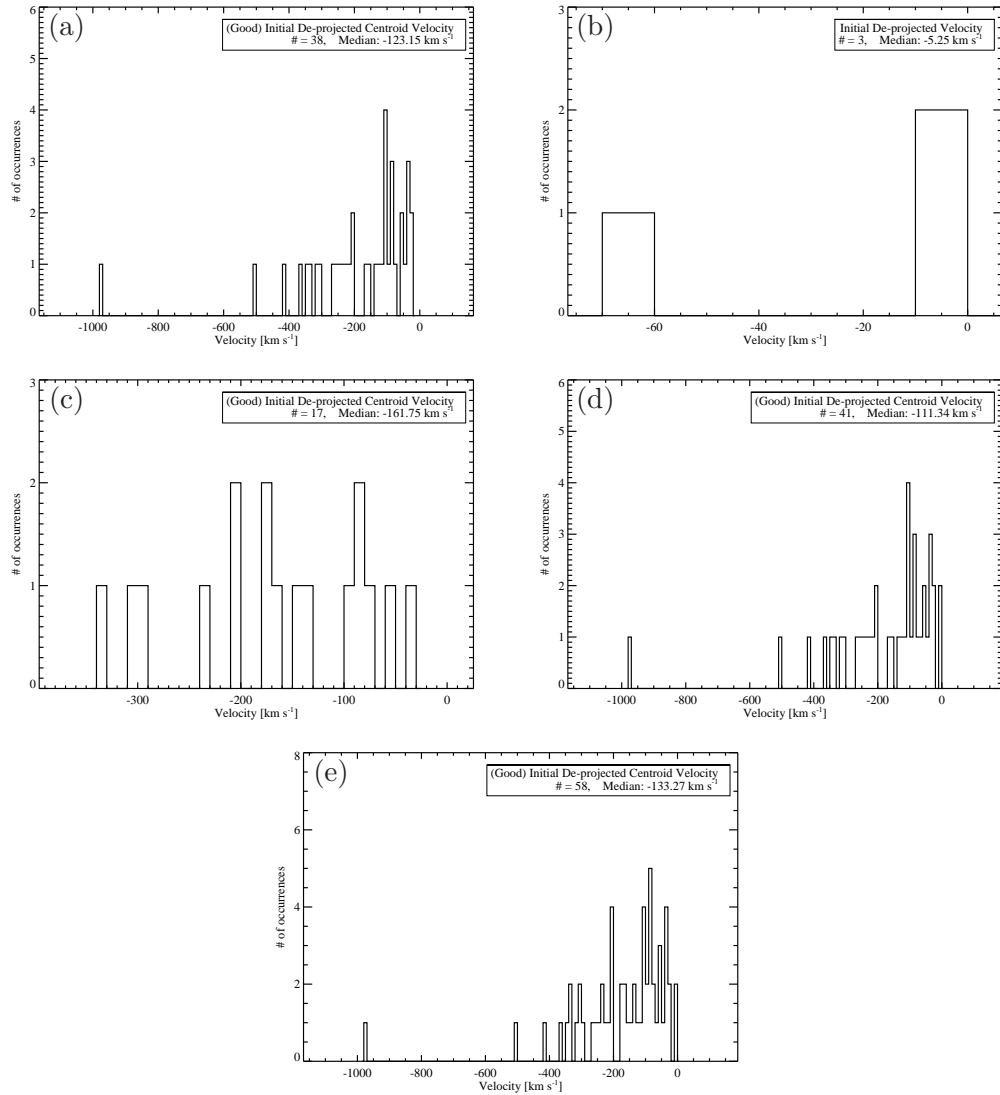


Figure 55: Histograms displaying initial velocity frequency for the limb flares from this study which contained SADs as observed by a) SXT, b) XRT, c) TRACE, d) SXT & XRT, and e) SXT, XRT, & TRACE.

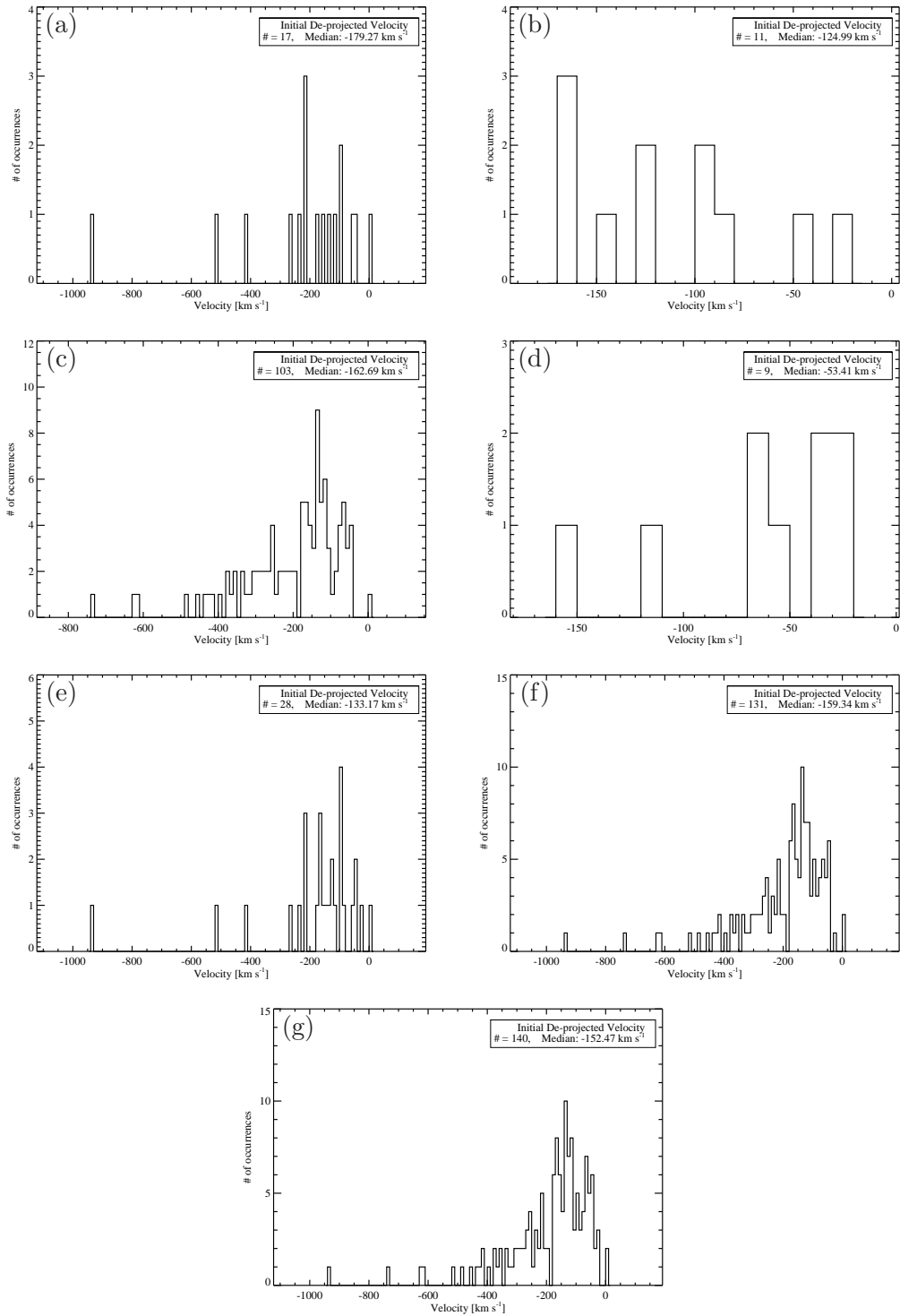


Figure 56: Histograms displaying initial velocity frequency for the limb flares from this study which contained SADLs as observed by a) SXT, b) XRT, c) TRACE, d) LASCO, e) SXT & XRT, f) SXT, XRT, & TRACE, and g) SXT, XRT, TRACE, & LASCO.

De-projected Acceleration.

The initial velocities below are only shown for flows tracked in at least 5 frames since they are calculated using 2-D polynomial fitting.

	SXT	XRT	TRACE	LASCO	Figure	# of Flows	Median [km s ⁻²]	Range [km s ⁻²]
All Limb	✓				57 (a)	55	.2	-2.2 – 15.
		✓			57 (b)	14	0.06	-0.01 – 0.55
			✓		57 (c)	120	0.8	-4.1 – 20.
				✓	57 (d)	9	0	0 – 0.03
	✓	✓			57 (e)	69	0.2	-2.2 – 15.
	✓	✓	✓		57 (f)	189	0.6	-4.1 – 20.
	✓	✓	✓	✓	57 (g)	198	0.4	-4.1 – 20.
SADs	✓				58 (a)	38	0.3	-2.2 – 15.
		✓			58 (b)	3	0	-0.01 – 0.06
			✓		58 (c)	17	0.4	-0.74 – 2.4
	✓	✓		✓	58 (d)	41	0.2	-2.2 – 15
	✓	✓	✓		58 (e)	58	0.4	-2.2 – 15
SADLs	✓				59 (a)	17	0.2	-1.5 – 8.0
		✓			59 (b)	11	0.1	0.01 – 0.6
			✓		59 (c)	103	0.8	-4.1 – 20.
				✓	59 (d)	9	0	0 – 0.03
	✓	✓			59 (e)	28	0.1	-1.5 – 7.9
	✓	✓	✓		59 (f)	131	0.7	-4.1 – 20
	✓	✓	✓	✓	59 (g)	140	0.5	-4.1 – 20

Table 6: De-projected acceleration statistics. Positive accelerations indicate deceleration of the downflows.

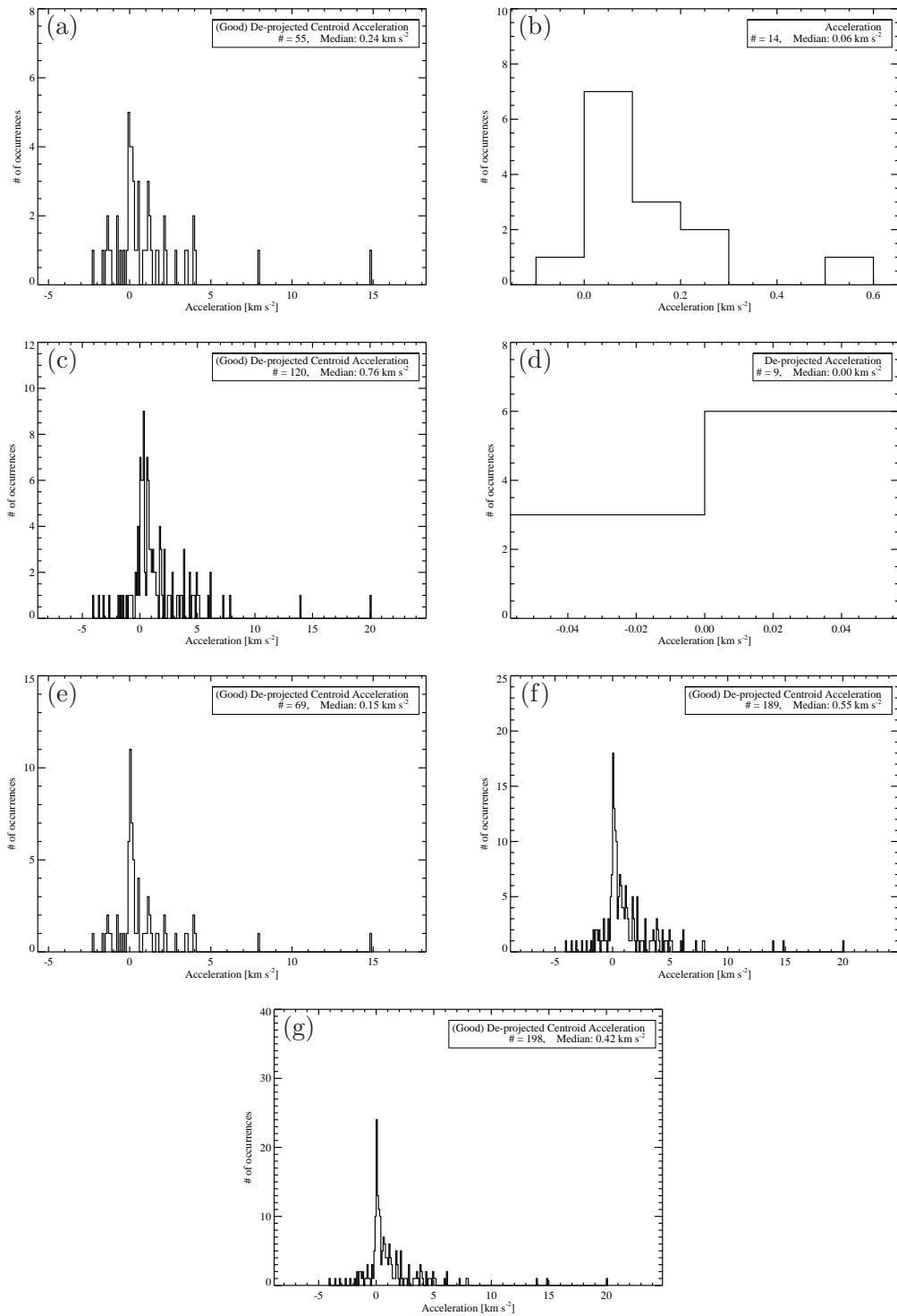


Figure 57: Histograms displaying acceleration frequency for the limb flares from this study as observed by a) SXT, b) XRT, c) TRACE, d) LASCO, e) SXT & XRT, f) SXT, XRT, & TRACE, and g) SXT, XRT, TRACE, & LASCO.

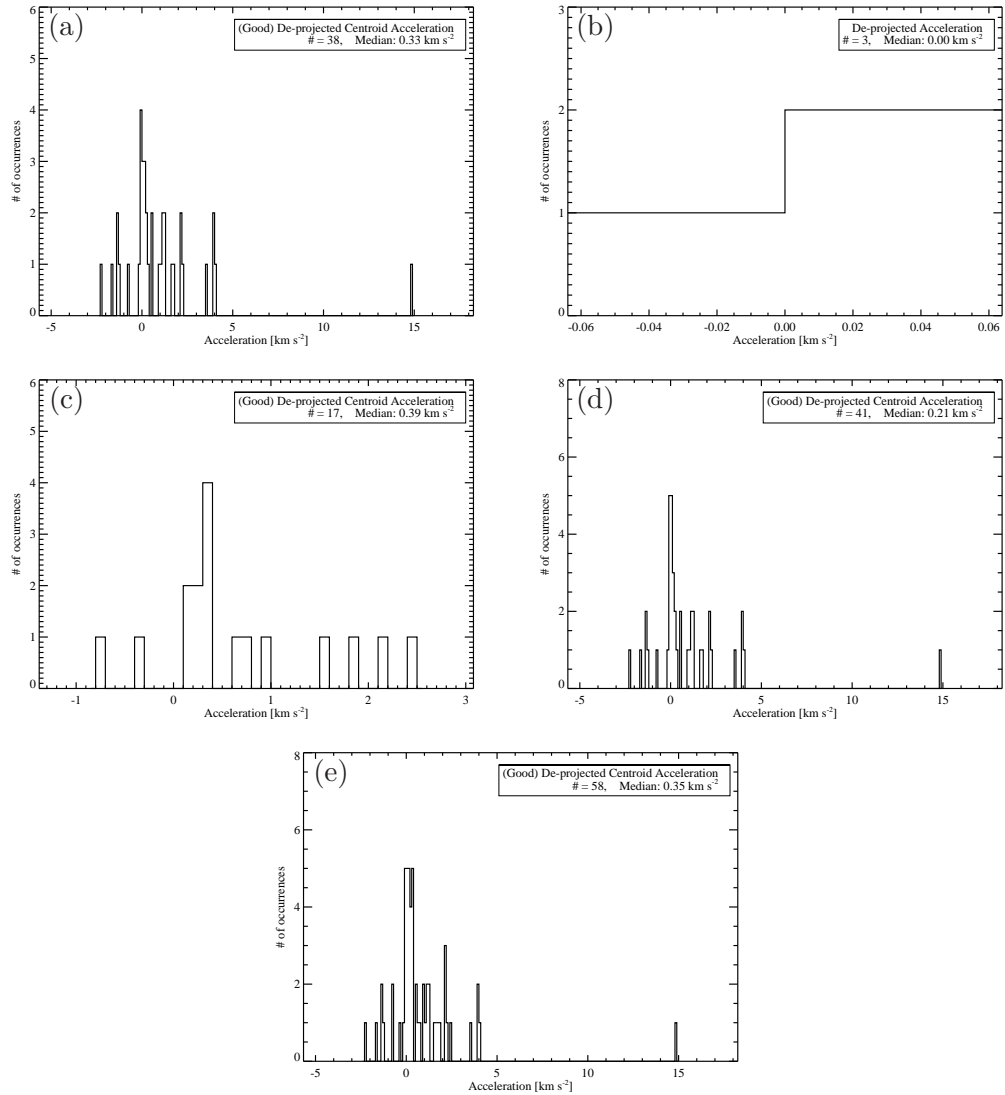


Figure 58: Histograms displaying acceleration frequency for the limb flares from this study which contained SADs as observed by a) SXT, b) XRT, c) TRACE, d) SXT & XRT, and e) SXT, XRT, & TRACE.

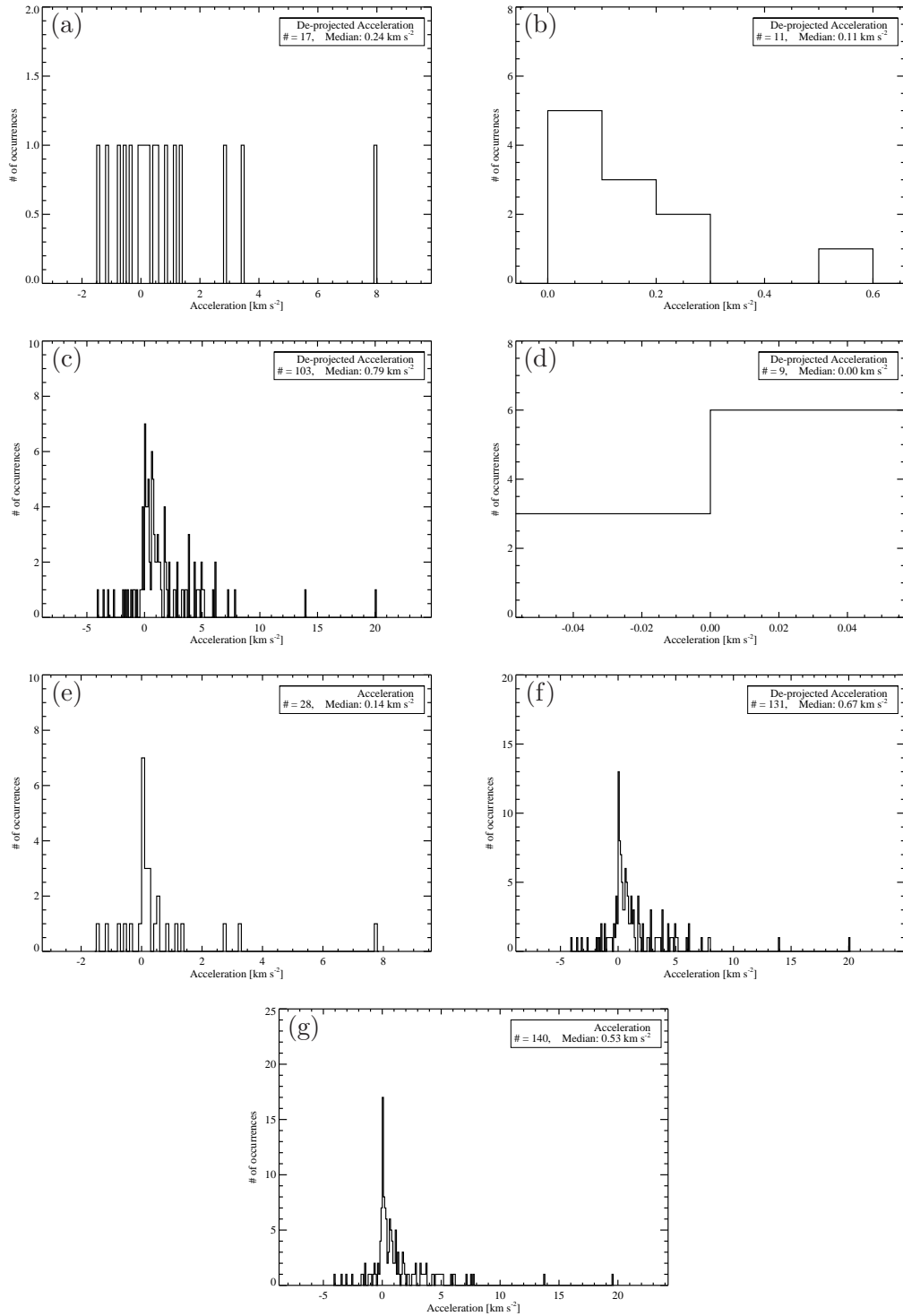


Figure 59: Histograms displaying acceleration frequency for the limb flares from this study which contained SADLs as observed by a) SXT, b) XRT, c) TRACE, d) LASCO, e) SXT & XRT, f) SXT, XRT, & TRACE, and g) SXT, XRT, TRACE, & LASCO.

Initial Area.

	SXT	XRT	TRACE	LASCO	Figure	# of Flows	Median [Mm ²]	Range [Mm ²]
All Limb	✓				60 (a-l)	120	25	11 – 89
(w/manual)	✓				60 (a-r)	173	25	10 – 89
(w/manual)		✓				24	16	7 – 16
(w/manual)		✓			60 (b-l)	23	3	2 – 17
(w/manual)			✓		60 (b-r)	161	2	2 – 17
(w/manual)				✓		11	968	968*
(w/manual)	✓	✓			61 (c-l)	120	25	12 – 89
(w/manual)	✓	✓			61 (c-r)	197	21	7 – 89
(w/manual)	✓	✓	✓		61 (d-l)	143	25	2 – 89
(w/manual)	✓	✓	✓		61 (d-r)	358	14	2 – 89
(w/manual)	✓	✓	✓	✓	61 (e-r)	369	16	2 – 967
SADs	✓				62 (a-l)	120	25	11 – 89
(w/manual)	✓				62 (a-r)	122	25	10 – 89
(w/manual)		✓				11	7	7 – 16
(w/manual)		✓			62 (b-l)	23	3	2 – 17
(w/manual)			✓					
(w/manual)				✓				
(w/manual)	✓	✓			62 (c-l)	120	25	12 – 89
(w/manual)	✓	✓			62 (c-r)	133	25	7 – 89
(w/manual)	✓	✓	✓		62 (d-l)	143	25	2 – 89
(w/manual)	✓	✓	✓		62 (d-r)	156	25	2 – 89
SADLs	✓							
(w/manual)	✓					51	18	10 – 18
(w/manual)		✓				13	16	16*
(w/manual)			✓			138	2	2*
(w/manual)				✓		11	968	968*
(w/manual)	✓	✓				64	18	10 – 18
(w/manual)	✓	✓	✓			202	2	2 – 18
(w/manual)	✓	✓	✓	✓		213	2	2 – 967

Table 7: Initial area statistics. “Manual area only” measurements are not plotted as histograms since there is no spread in the data. *No range in data.

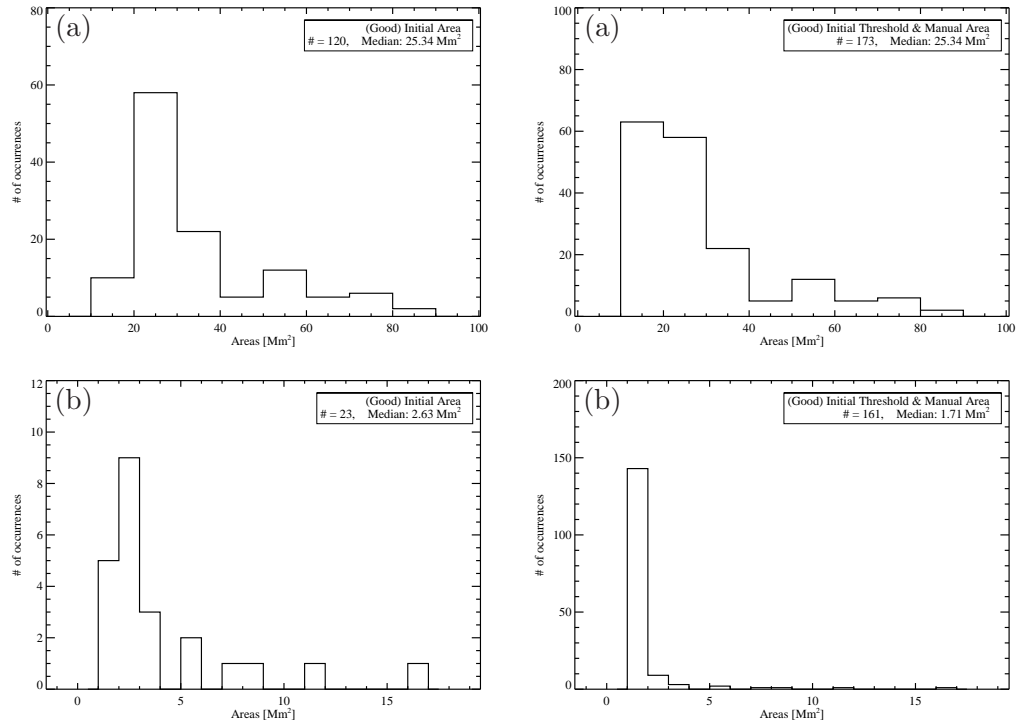


Figure 60: Histograms displaying initial area frequency for the limb flares from this study as observed by a) SXT and b) TRACE. *Left:* Troughs chosen using thresholds. *Right:* Threshold plus manual trough areas.

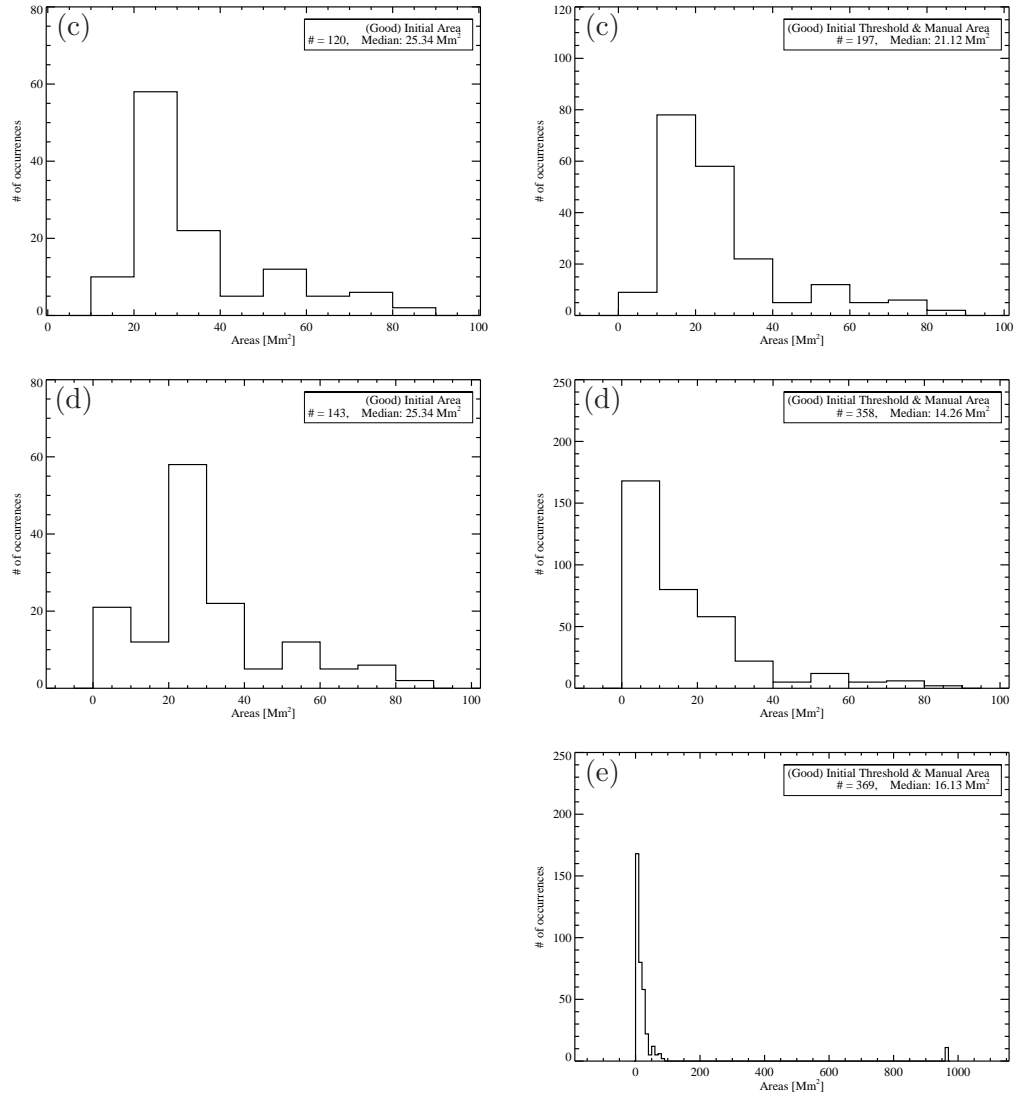


Figure 61: Histograms displaying initial area frequency for the limb flares from this study as observed by c) SXT & XRT, d) SXT, XRT, & TRACE, and e) SXT, XRT, TRACE, & LASCO. *Left:* Troughs chosen using thresholds. *Right:* Threshold plus manual trough areas.

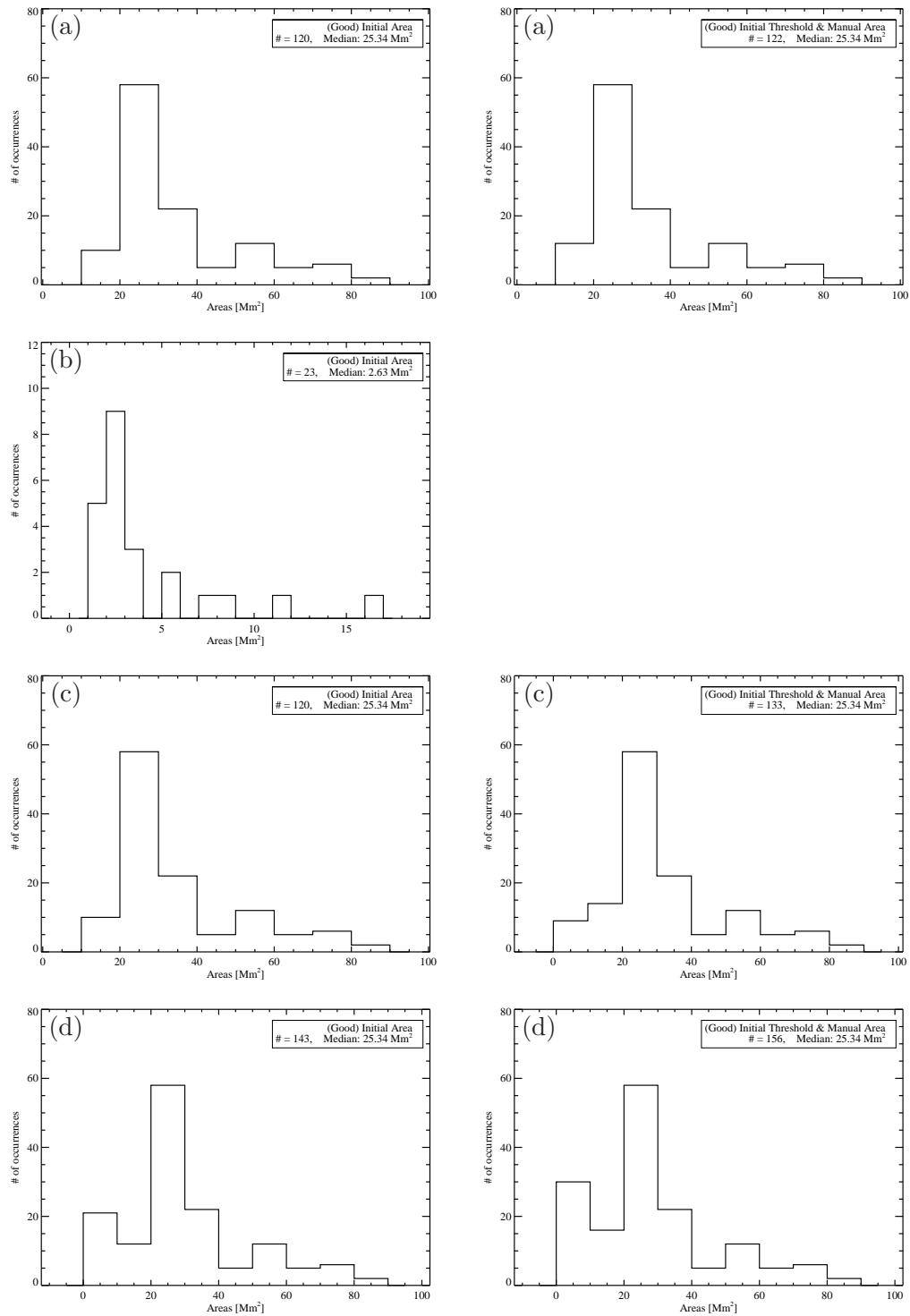


Figure 62: Histograms displaying initial area frequency for the limb flares from this study which contained SADs as observed by a) SXT, b) TRACE, c) SXT & XRT, and d) SXT, XRT, & TRACE. *Left:* Troughs chosen using thresholds. *Right:* Threshold plus manual trough areas.

Initial Height.

	SXT	XRT	TRACE	LASCO	Figure	# of Flows	Median [Mm]	Range [Mm]
All Limb	✓				63 (a)	173	108	48 – 184
		✓			63 (b)	24	110	34 – 194
			✓		63 (c)	161	48	13 – 119
				✓	63 (d)	11	1365	1084 – 2220
	✓	✓			63 (e)	197	108	34 – 194
	✓	✓	✓		63 (f)	358	83	13 – 194
	✓	✓	✓	✓	63 (g)	369	85	13 – 2220
SADs	✓				64 (a)	122	108	48 – 184
		✓			64 (b)	11	42	34 – 101
			✓		64 (c)	23	76	40 – 100
	✓	✓		✓	64 (d)	133	104	34 – 184
	✓	✓	✓		64 (e)	156	99	34 – 187
SADLs	✓				65 (a)	51	109	171 – 172
		✓			65 (b)	13	136	107 – 194
			✓		65 (c)	138	46	13 – 119
				✓	65 (d)	11	1365	1084 – 2220
	✓	✓			65 (e)	64	116	71 – 194
	✓	✓	✓		65 (f)	202	56	13 – 194
	✓	✓	✓	✓	65 (g)	213	59	13 – 2220

Table 8: Initial de-projected height statistics.

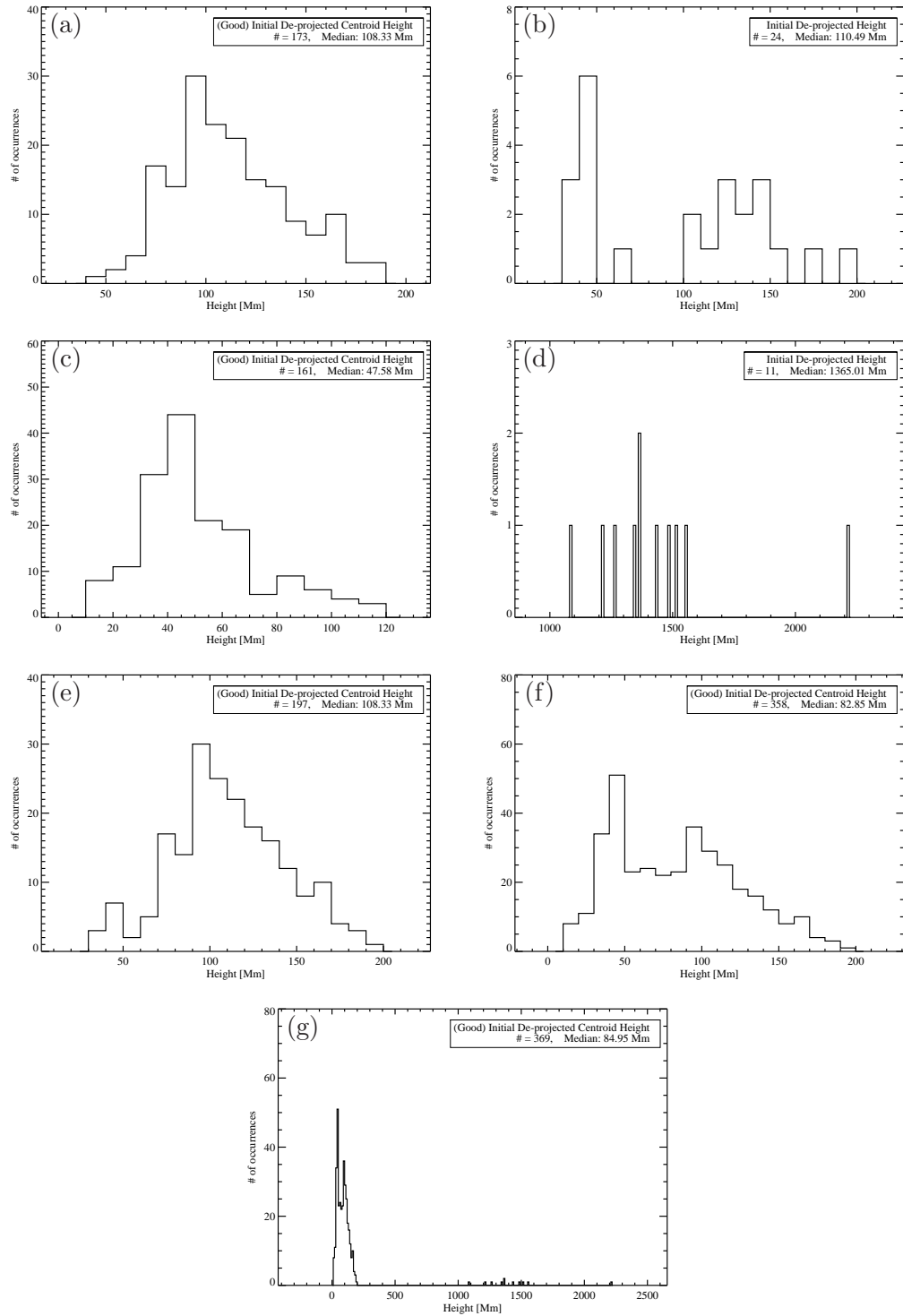


Figure 63: Histograms displaying initial height frequency for the limb flares from this study as observed by a) SXT, b) XRT, c) TRACE, d) LASCO, e) SXT & XRT, f) SXT, XRT, & TRACE, and g) SXT, XRT, TRACE, & LASCO.

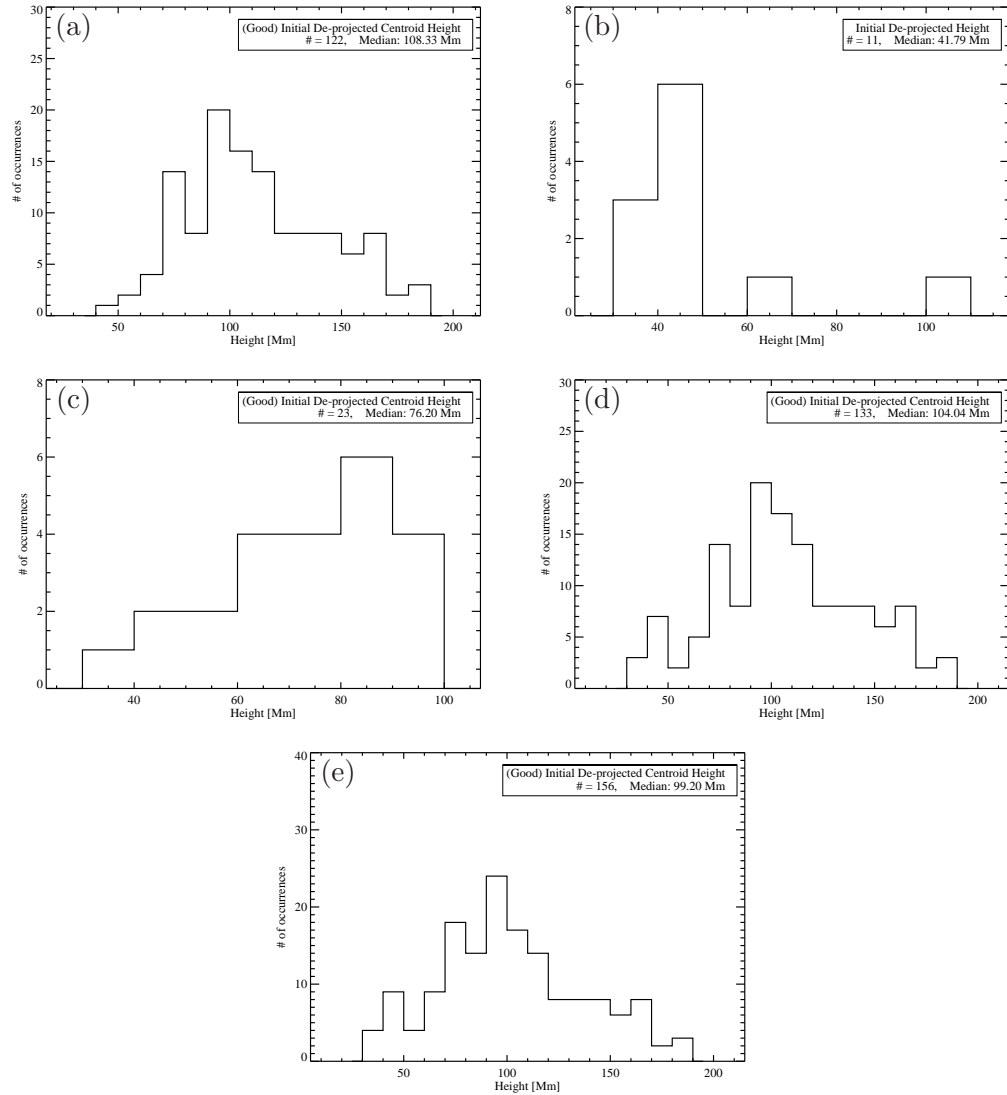


Figure 64: Histograms displaying initial height frequency for the limb flares from this study which contained SADs as observed by a) SXT, b) XRT, c) TRACE, d) SXT & XRT, and e) SXT, XRT, & TRACE.

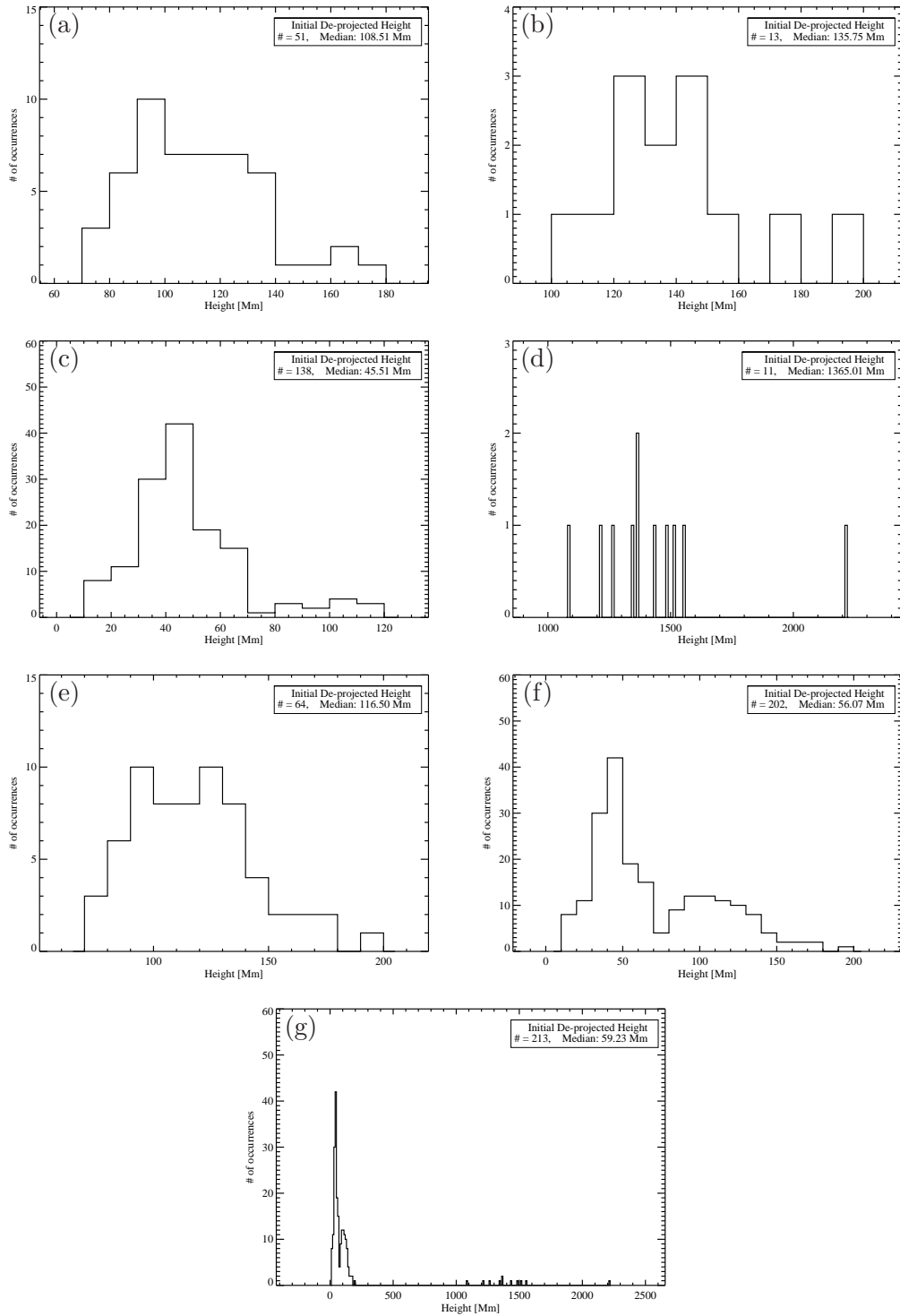


Figure 65: Histograms displaying initial height frequency for the limb flares from this study which contained SADLs as observed by a) SXT, b) XRT, c) TRACE, d) LASCO, e) SXT & XRT, f) SXT, XRT, & TRACE, and g) SXT, XRT, TRACE, & LASCO.

Change in Height.

	SXT	XRT	TRACE	LASCO	Figure	# of Flows	Median [Mm]	Range [Mm]
All Limb	✓				66 (a)	173	-19	-2 – -68
		✓			66 (b)	24	-21	-5 – -96
			✓		66 (c)	161	-10	-3 – -45
				✓	66 (d)	11	-319	-115 – -437
	✓	✓			66 (e)	197	-19	-2 – -96
	✓	✓	✓		66 (f)	358	-14	-2 – -96
	✓	✓	✓	✓	66 (g)	369	-14	-2 – -437
SADs	✓				67 (a)	122	-18	-2 – -68
		✓			67 (b)	11	-11	-5 – -23
			✓		67 (c)	23	-15	-3 – -45
				✓	67 (d)	133	-17	-2 – -68
	✓	✓	✓		67 (e)	156	-17	-2 – -68
SADLs	✓				68 (a)	51	20	5 – 60
		✓			68 (b)	13	39	48 – 91
			✓		68 (c)	138	10	3 – 35
				✓	68 (d)	11	319	115 – 437
	✓	✓			68 (e)	64	22	5 – 96
	✓	✓	✓		68 (f)	202	12	3 – 96
	✓	✓	✓	✓	68 (g)	213	13	3 – 437

Table 9: De-projected change in height statistics.

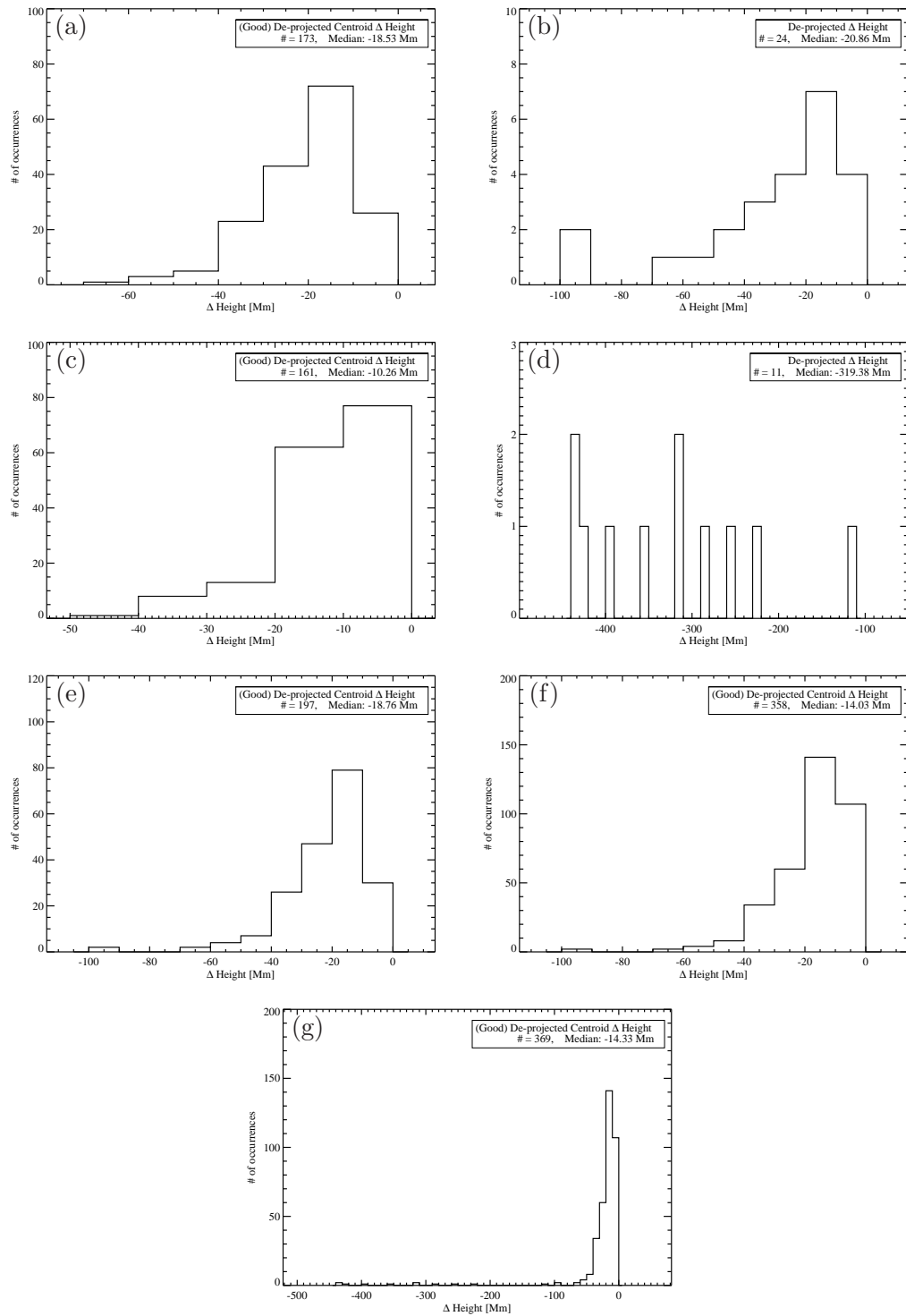


Figure 66: Histograms displaying change in height frequency for the limb flares from this study as observed by a) SXT, b) XRT, c) TRACE, d) LASCO, e) SXT & XRT, f) SXT, XRT, & TRACE, and g) SXT, XRT, TRACE, & LASCO.

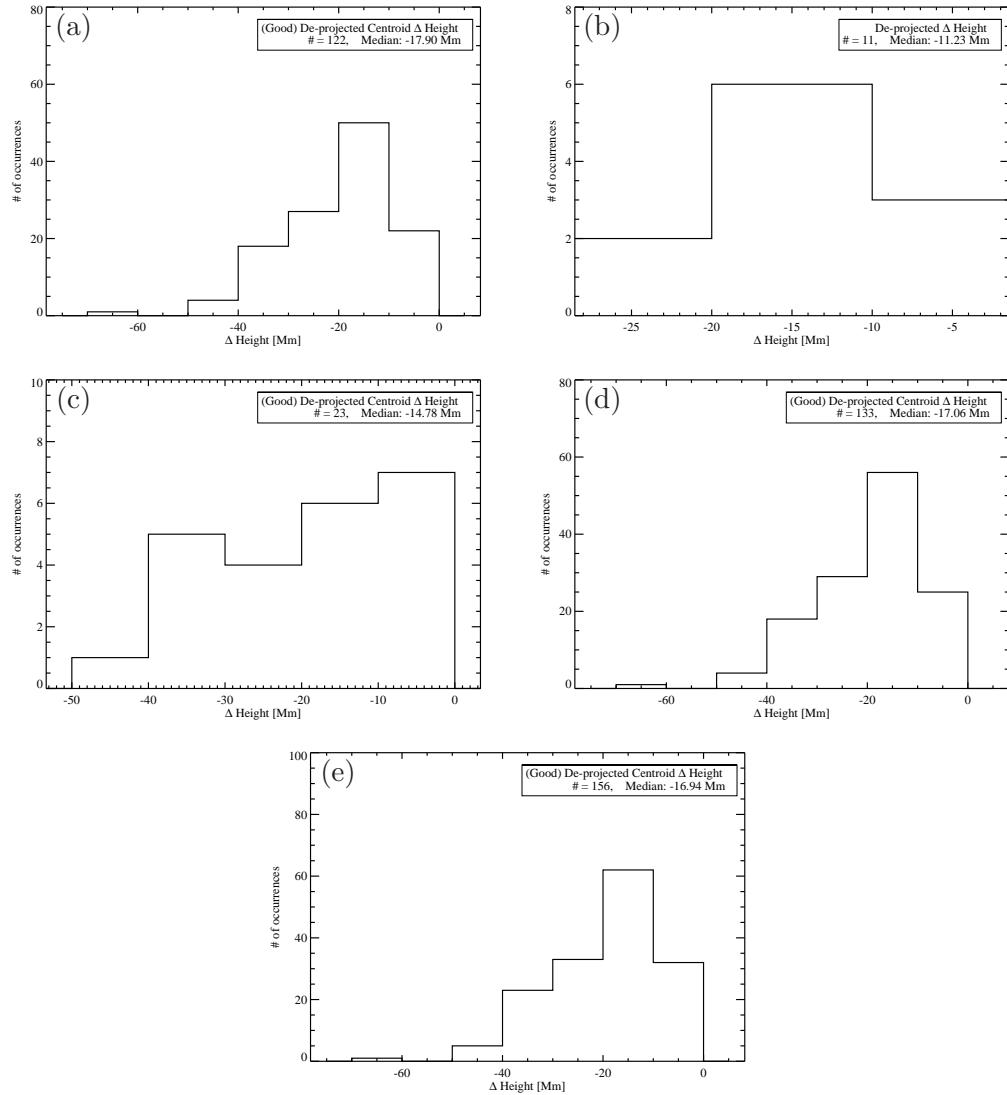


Figure 67: Histograms displaying change in height frequency for the limb flares from this study which contained SADs as observed by a) SXT, b) XRT, c) TRACE, d) SXT & XRT, and e) SXT, XRT, & TRACE.

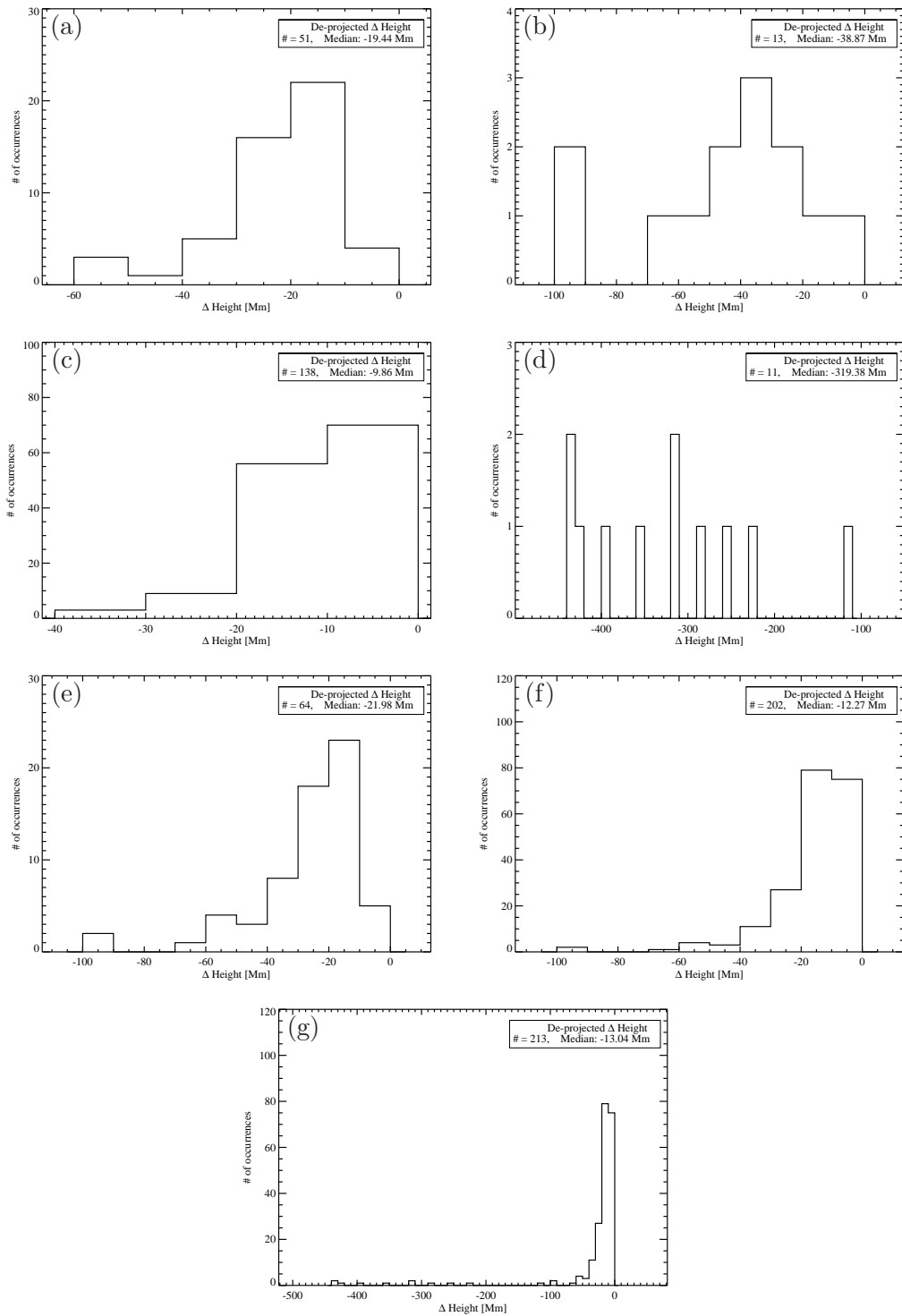


Figure 68: Histograms displaying change in height frequency for the limb flares from this study which contained SADLs as observed by a) SXT, b) XRT, c) TRACE, d) LASCO, e) SXT & XRT, f) SXT, XRT, & TRACE, and g) SXT, XRT, TRACE, & LASCO.

Initial Magnetic Flux.

	SXT	XRT	TRACE	LASCO	Figure	# of Flows	Median [$\times 10^{18}$ Mx]	Range [$\times 10^{18}$ Mx]
All Limb	✓				69 (a- <i>l</i>)	120	2.3	0.17 – 15.
(w/manual)	✓				69 (a- <i>r</i>)	173	2.1	0.17 – 15.
(w/manual)		✓				24	.24	0.09 – 0.9
(w/manual)		✓			69 (b- <i>l</i>)	23	0.75	0.4 – 4.5
(w/manual)			✓		69 (b- <i>r</i>)	161	0.4	0.05 – 4.5
(w/manual)				✓		11	1.0	1.0 – 1.0
(w/manual)	✓	✓		✓	70 (c- <i>l</i>)	120	2.3	0.2 – 15.
(w/manual)	✓	✓			70 (c- <i>r</i>)	197	1.6	0.09 – 15.
(w/manual)	✓	✓	✓		70 (d- <i>l</i>)	143	1.8	0.2 – 15.
(w/manual)	✓	✓	✓		70 (d- <i>r</i>)	358	0.72	0.05 – 15.
(w/manual)	✓	✓	✓	✓	70 (e- <i>l</i>)	143	1.8	0.2 – 15.
(w/manual)	✓	✓	✓	✓	70 (e- <i>r</i>)	369	0.7	0.05 – 15.
East	✓				71 (a)	110	1.8	0.3 – 14.
		✓				53	0.06	0.05 – 0.09
			✓			11	1.0	1.0 – 1.0
	✓		✓	✓	71 (b)	163	0.9	0.05 – 14.
	✓		✓	✓	71 (c)	174	1.0	0.05 – 14.
West	✓				72 (a)	63	3.2	0.2 – 15.
		✓				24	.24	0.09 – 0.9
			✓		72 (b)	108	0.67	0.2 – 4.5
	✓	✓		✓	72 (c)	87	0.81	0.08 – 15.
	✓	✓	✓		72 (d)	195	0.67	0.08 – 15.

Table 10: Initial magnetic flux statistics. “Manual area only” measurements are not plotted as histograms since there is no spread in the data.

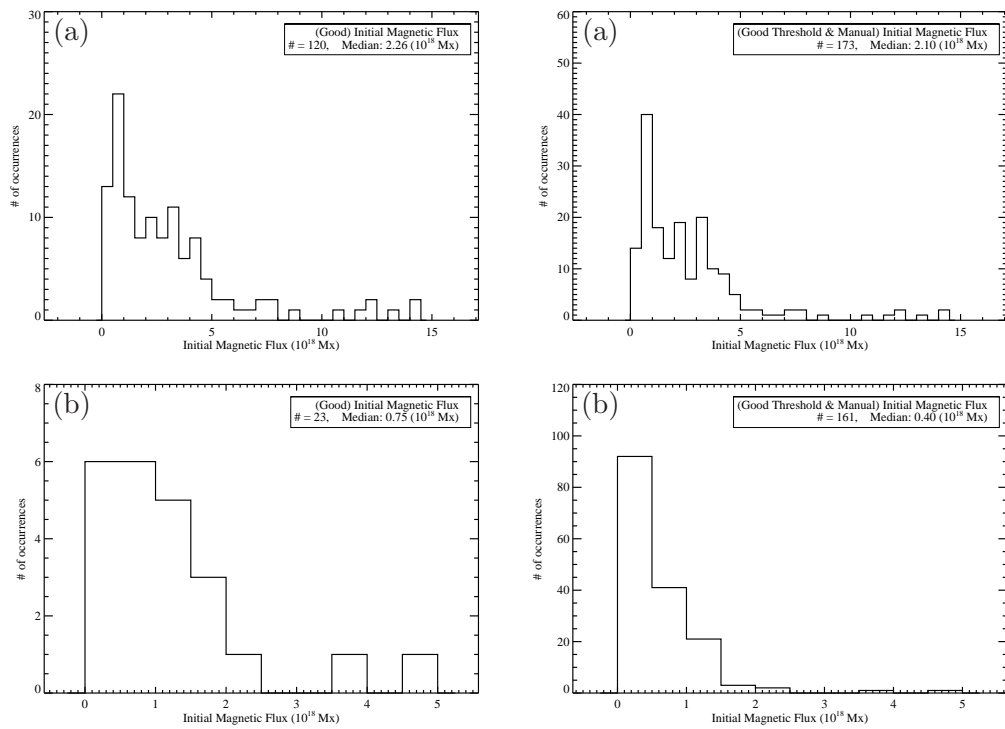


Figure 69: Histograms displaying magnetic flux frequency for the limb flares from this study as observed by a) SXT and b) TRACE. *Left:* Troughs chosen using thresholds. *Right:* Threshold plus manual trough areas.

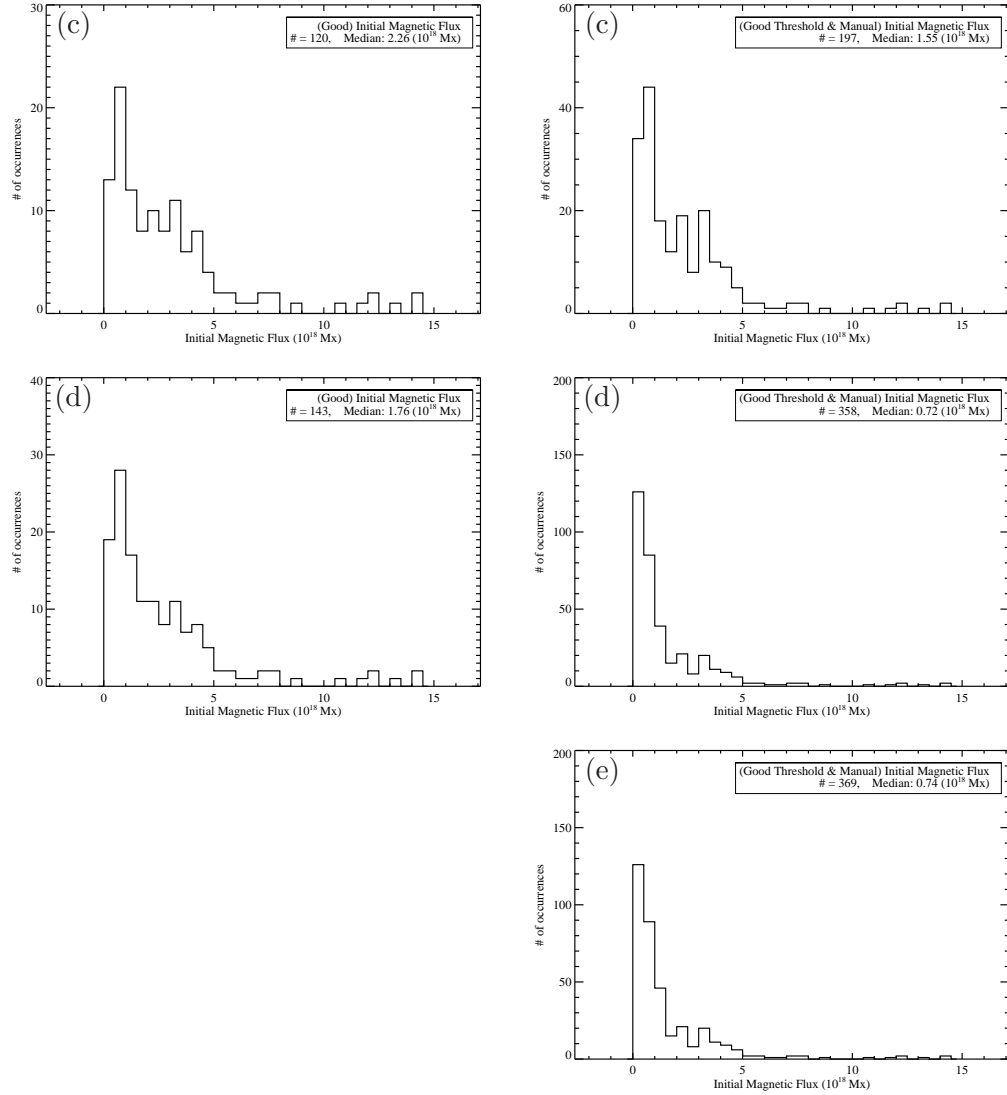


Figure 70: Histograms displaying magnetic flux frequency for the limb flares from this study as observed by c) SXT & XRT, d) SXT, XRT, & TRACE, and e) SXT, XRT, TRACE, & LASCO. *Left:* Troughs chosen using thresholds. *Right:* Threshold plus manual trough areas.

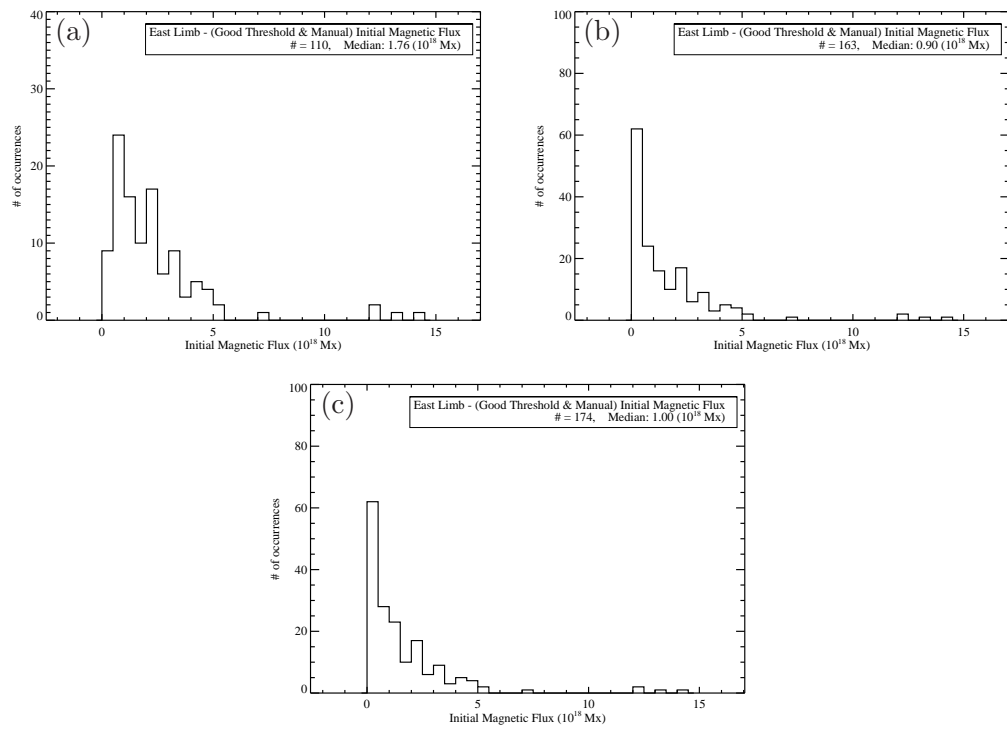


Figure 71: Histograms displaying magnetic flux frequency for east limb flares from this study as observed by a) SXT, b) SXT & TRACE, and c) SXT, TRACE, & LASCO.

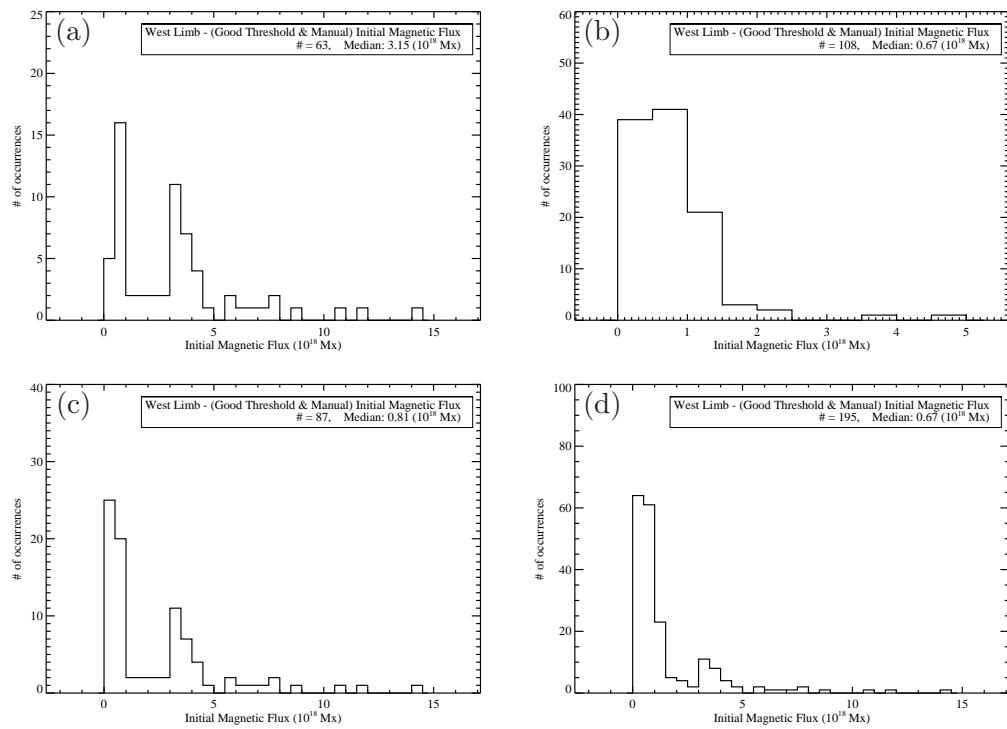


Figure 72: Histograms displaying magnetic flux frequency for the west limb flares from this study as observed by a) SXT, b) TRACE, c) SXT & XRT, and d) SXT, XRT, & TRACE.

Shrinkage Energy.

	SXT	XRT	TRACE	LASCO	Figure	# of Flows	Median [x10 ²⁷ erg]	Range [x10 ²⁷ erg]
All Limb	✓				73 (a-l)	120	1.3	0.004 – 41.
(w/manual)	✓				73 (a-r)	173	1.3	0.004 – 41.
(w/manual)		✓				24	0.03	0.01 – 0.3
(w/manual)		✓			73 (b-l)	23	1.4	0.4 – 15
(w/manual)			✓		73 (b-r)	161	0.44	0.4 – 15
(w/manual)				✓		11	0.13	0.05 – 0.2
(w/manual)	✓	✓		✓	74 (c-l)	120	1.3	0.004 – 41.
(w/manual)	✓	✓			74 (c-r)	197	0.86	0.004 – 41.
(w/manual)	✓	✓	✓		74 (d-l)	143	1.3	0.004 – 41.
(w/manual)	✓	✓	✓		74 (d-r)	358	0.55	0.004 – 41.
(w/manual)	✓	✓	✓	✓	74 (e-r)	369	0.49	0.004 – 41.
East	✓				75 (a)	110	1.0	0.03 – 10.
		✓				53	0.008	0.004 – 0.02
			✓			11	0.13	0.05 – 0.2
	✓		✓	✓	75 (b)	163	0.28	0.03 – 10.
	✓		✓	✓	75 (c)	174	0.24	0.004 – 10.
West	✓				76 (a)	63	2.7	0.004 – 41.
		✓				24	0.03	0.01 – 0.3
			✓		76 (b)	108	1.2	0.1 – 15.
				✓		87	0.54	0.004 – 41.
	✓	✓	✓		76 (c)	195	1.1	0.004 – 41.
	✓	✓	✓		76 (d)	195	1.1	0.004 – 41.

Table 11: Shrinkage energy statistics. “Manual area only” measurements are not plotted as histograms since there is no spread in the data.

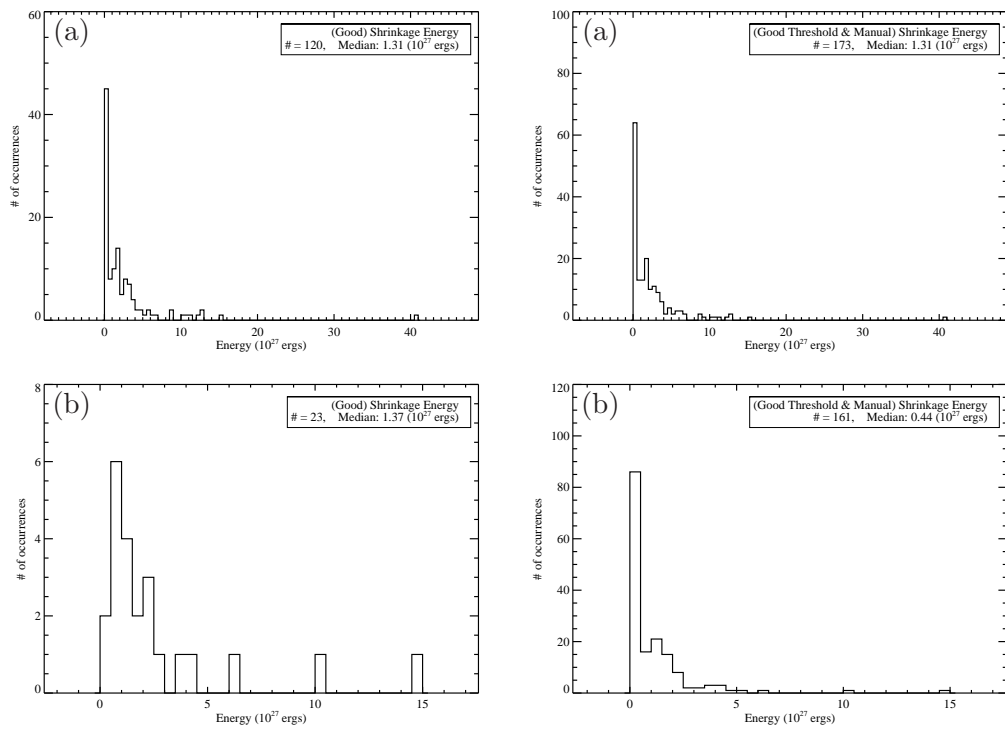


Figure 73: Histograms displaying magnetic work frequency for the limb flares from this study as observed by a) SXT and b) TRACE. *Left:* Troughs chosen using thresholds. *Right:* Threshold plus manual trough areas.

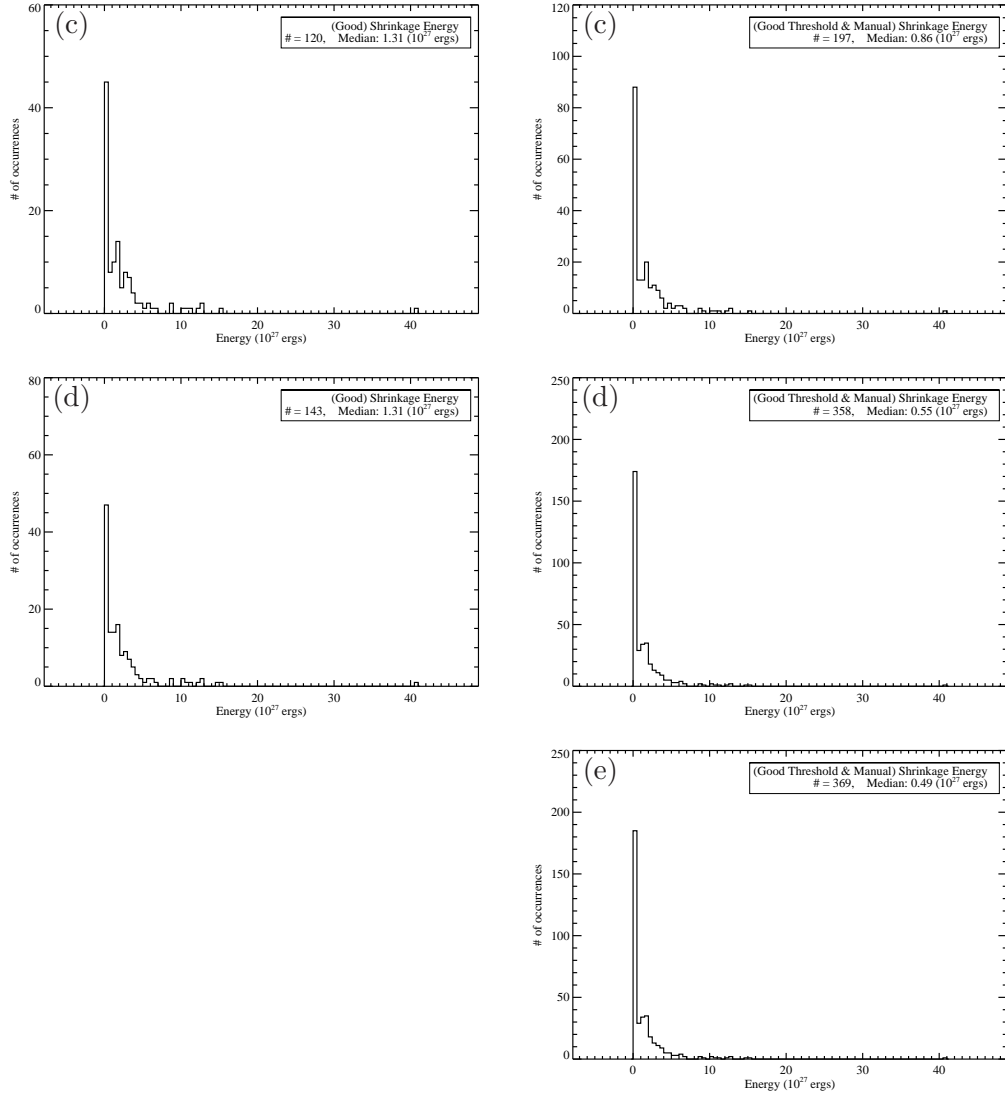


Figure 74: Histograms displaying magnetic work frequency for the limb flares from this study as observed by c) SXT & XRT, d) SXT, XRT, & TRACE, and e) SXT, XRT, TRACE, & LASCO. *Left:* Troughs chosen using thresholds. *Right:* Threshold plus manual trough areas.

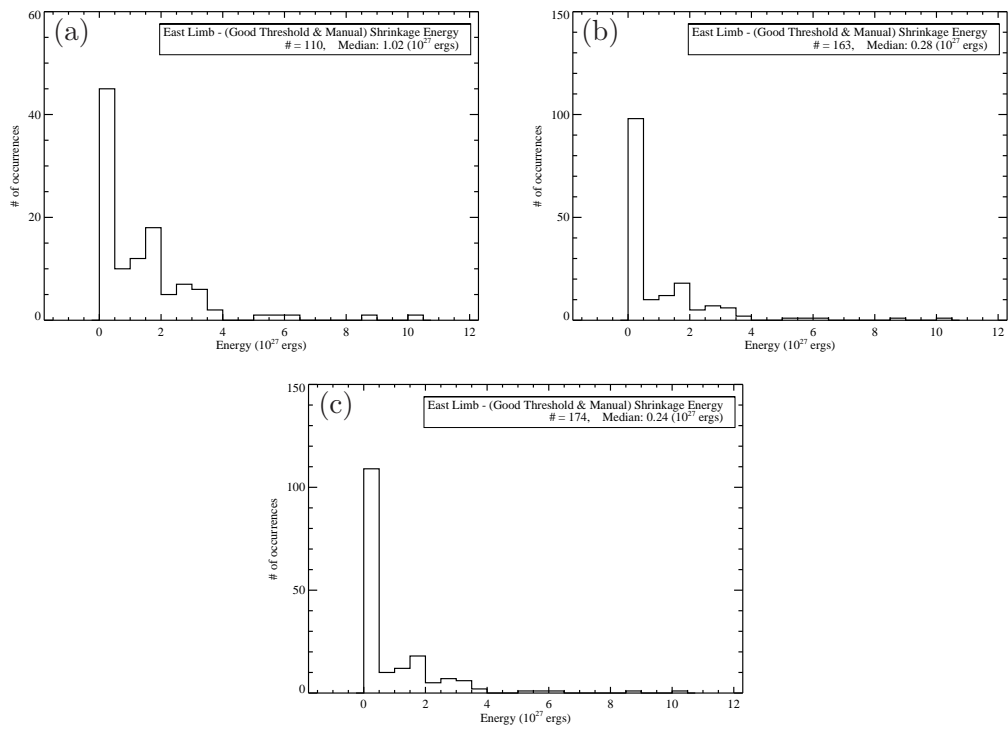


Figure 75: Histograms displaying magnetic work frequency for the east limb flares from this study as observed by a) SXT, b) SXT & TRACE, and c) SXT, TRACE, & LASCO.

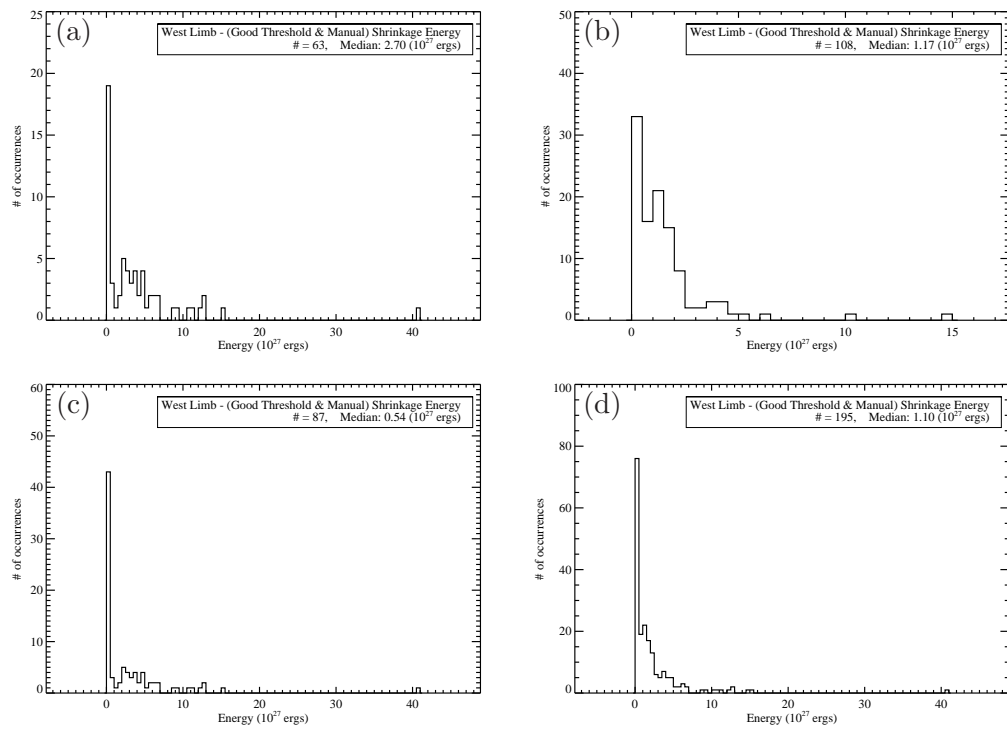


Figure 76: Histograms displaying magnetic work frequency for the limb flares from this study which contained SADs as observed by a) SXT, b) TRACE, c) SXT & XRT, and d) SXT, XRT, & TRACE.

APPENDIX B

ODE TO DR. SEUSS

One flare, two flare,
red flare, blue flare.

This flare has a flow.

This flow's in a flare.

Some flows have no flares,
But as to those, who cares?

Error bars and medians,
Quartiles, means and histograms.

This flow is a SAD.

That flow is a SADL.

The SAD's a SADL at right angles.

More flows in a swaying fan;

Analyze them all you can.

Copious flows in the FOV,

outside maybe two or three;

LASCO sees them eventually.

– Dr. Charles Kankelborg